

UNCLASSIFIED

AD NUMBER

ADB029489

LIMITATION CHANGES

TO:

Approved for public release; distribution is unlimited.

FROM:

Distribution authorized to U.S. Gov't. agencies only; Test and Evaluation; AUG 1978. Other requests shall be referred to Air Force Space and Missile Systems Organization, RSSE, PO Box 92960, Worldway Postal Center, Los Angeles, CA 90009.

AUTHORITY

USAF/SAMSO ltr, 23 Feb 1979

THIS PAGE IS UNCLASSIFIED

DOC_NUM SER CN
UNC32016-PDC A 1



**DYNAMIC FORCE MEASUREMENTS
AND BOUNDARY-LAYER TRANSITION MAPPING
ON A SPINNING 9-DEG CONE WITH AND WITHOUT
MASS ADDITION AT MACH NUMBERS 5 AND 8**

**T. D. Buchanan, L. M. Jenke, and M. J. Chaney
ARO, Inc., a Sverdrup Corporation Company**

**VON KÁRMÁN GAS DYNAMICS FACILITY
ARNOLD ENGINEERING DEVELOPMENT CENTER
AIR FORCE SYSTEMS COMMAND
ARNOLD AIR FORCE STATION, TENNESSEE 37389**

August 1978

Final Report for Period November 1977 - January 1978

Distribution limited to U.S. Government agencies only, this report contains information on test and evaluation of military hardware; August 1978; other requests for this document must be referred to Space and Missile Systems Organization/RSSE, P. O. Box 92960, Worldway Postal Center, Los Angeles, California 90009.

Prepared for

**SPACE AND MISSILE SYSTEMS ORGANIZATION/RSSE
P.O. BOX 92960, WORLDWAY POSTAL CENTER
LOS ANGELES, CALIFORNIA 90009**

NOTICES

When U. S. Government drawings, specifications, or other data are used for any purpose other than a definitely related Government procurement operation, the Government thereby incurs no responsibility nor any obligation whatsoever, and the fact that the Government may have formulated, furnished, or in any way supplied the said drawings, specifications, or other data, is not to be regarded by implication or otherwise, or in any manner licensing the holder or any other person or corporation, or conveying any rights or permission to manufacture, use, or sell any patented invention that may in any way be related thereto.

Qualified users may obtain copies of this report from the Defense Documentation Center.

References to named commercial products in this report are not to be considered in any sense as an indorsement of the product by the United States Air Force or the Government.

APPROVAL STATEMENT

This report has been reviewed and approved.



ERVIN P. JASKOLSKI, Captain, USAF
Test Director, VKF Division
Directorate of Test Operations

Approved for publication:

FOR THE COMMANDER



ALAN L. DEVEREAUX, Colonel, USAF
Director of Test Operations
Deputy for Operations

UNCLASSIFIED

REPORT DOCUMENTATION PAGE		READ INSTRUCTIONS BEFORE COMPLETING FORM
1 REPORT NUMBER AEDC-TR-78-40	2 GOVT ACCESSION NO.	3 RECIPIENT'S CATALOG NUMBER
4 TITLE (and Subtitle) DYNAMIC FORCE MEASUREMENTS AND BOUNDARY-LAYER TRANSITION MAPPING ON A SPINNING 9-DEG CONE WITH AND WITHOUT MASS ADDITION AT MACH NUMBERS 5 AND 8		5 TYPE OF REPORT & PERIOD COVERED Final Report, Nov 1977 - Jan 1978
		6 PERFORMING ORG REPORT NUMBER
7 AUTHOR(s) T. D. Buchanan, L. M. Jenke, and M. J. Chaney, ARO, Inc.		8 CONTRACT OR GRANT NUMBER(s)
9 PERFORMING ORGANIZATION NAME AND ADDRESS Arnold Engineering Development Center/DO Air Force Systems Command Arnold Air Force Station, Tennessee 37389		10 PROGRAM ELEMENT, PROJECT, TASK AREA & WORK UNIT NUMBERS Program Element 63311F
11 CONTROLLING OFFICE NAME AND ADDRESS Space and Missile Systems Organization/RSSE P. O. Box 92960, Worldway Postal Center, Los Angeles, California 90009		12 REPORT DATE August 1978
		13 NUMBER OF PAGES 104
14 MONITORING AGENCY NAME & ADDRESS (if different from Controlling Office)		15 SECURITY CLASS (of this report) UNCLASSIFIED
		15a DECLASSIFICATION/DOWNGRADING SCHEDULE N/A
16 DISTRIBUTION STATEMENT (of this Report) Distribution limited to U.S. Government agencies only; this report contains information on test and evaluation of military hardware; August 1978; other requests for this document must be referred to Space and Missile Systems Organization/RSSE, P. O. Box 92960, Worldway Postal Center, Los Angeles, California 90009.		
17 DISTRIBUTION STATEMENT (of the abstract entered in Block 20, if different from Report)		
18 SUPPLEMENTARY NOTES Available in DDC		
19 KEY WORDS (Continue on reverse side if necessary and identify by block number) boundary-layer transition spin (motion) heat transfer measurements Reynolds number dynamic performance supersonic flow conical bodies		
20 ABSTRACT (Continue on reverse side if necessary and identify by block number) A wind tunnel test program was conducted to determine the effect of spin on the aerodynamic forces and moments and the shape and movement of the boundary-layer transition zone on 9-deg (half-angle) cone configurations. The effects of nose geometry, mass addition, angle of attack, Mach number, and Reynolds number were investigated at various spin rates. Results were obtained using a spin mechanism (1-DOF) developed for this test and a three		

UNCLASSIFIED

UNCLASSIFIED

20. ABSTRACT (Continued)

degree-of-freedom (3-DOF) mechanism. The test was conducted at Mach numbers 5 and 8 at free-stream Reynolds numbers, based on model length, ranging from 1.6×10^6 to 24×10^6 and angles of attack ranging from -6 to 6 deg. The dynamic heat-transfer rate results were corrected for gage response characteristics with the use of the digital Fourier Analysis technique. The dynamic results were generally in good agreement with the steady-state results. The data obtained from the spin tests indicated there were no effects of spin on the transition zone nor were there any induced lateral forces or moments produced at the test conditions of this test.

PREFACE

The work reported herein was conducted by the Arnold Engineering Development Center (AEDC), Air Force Systems Command (AFSC), at the joint request of the Space and Missiles System Organization (SAMSO) and Defense Nuclear Agency (DNA) for the Prototype Development Associates, (PDA) Inc., under Program Element 63311F. The PDA project monitor was Mr. J. E. Dunn; the DNA monitor was Lt. Commander R. J. Nibe, and the SAMSO monitor was Capt. Robert Chambers. The results presented herein were obtained by ARO, Inc., AEDC Division (a Sverdrup Corporation Company), operating contractor for the AEDC, AFSC, Arnold Air Force Station, Tennessee, under ARO Project Number V41A/B-N7. The final data package was completed on March 30, 1978, and the manuscript was submitted for publication on June 8, 1978.

The authors acknowledge the splendid support by the personnel of AEDC/VKF. Individuals who merit mentioning were J. L. Roberson and M. B. Krauth for their programming and data reduction efforts; D. C. Carpenter and T. L. Bradford for their instrumentation support, and A. L. Bouldin and C. E. Waldrup for their support during the test preparation.

CONTENTS

	<u>Page</u>
1.0 INTRODUCTION	7
2.0 APPARATUS	
2.1 Wind Tunnels	8
2.2 Models	8
2.3 Test Mechanisms	10
2.4 Instrumentation and Measurements	11
3.0 TEST DESCRIPTION	
3.1 Dynamic Gage Calibration	17
3.2 3-DOF Telemetry Calibration	18
3.3 Test Conditions	18
3.4 Test Procedures	18
4.0 ACCURACY OF MEASUREMENTS	
4.1 Test Conditions	23
4.2 Spin Test Data	24
4.3 3-DOF Test Data	26
5.0 RESULTS AND DISCUSSION	26
6.0 SUMMARY	29
REFERENCES	30

ILLUSTRATIONS

Figure

1. Test Facilities	31
2. Photographs of Model Installations	33
3. Photograph of Model Cooling Manifold in Tunnel A Test Section Tank	35
4. Model Details	36
5. Frustum Details	38
6. Nose Tip Details	44
7. Boundary-Layer Trips	48
8. Groove-Type Trip Configurations	49
9. Details of the Spin Test Mechanism	50
10. Photographs of Spin Test Mechanism	51
11. 3-DOF Test Mechanism (VKF-3.A)	53
12. Instrumentation Locations on Spin Model	54

<u>Figure</u>	<u>Page</u>
13. Instrumentation Locations on 3-DOF Model	55
14. Details of Heat Gages	56
15. Thermal Pulse Generator Photograph	59
16. Four-Component Magnus Balance 4.00-Y-34-076	60
17. Mass (N ₂) Injection System	61
18. Instrumentation Block Diagram	64
19. Dynamic Data Acquisition Block Diagram	65
20. Dynamic Data Reduction Diagram	66
21. Typical Thermopile Gardon Gage Dynamic Calibration	67
22. Typical Temp-Sensor with Analog Circuit Dynamic Calibration	69
23. Typical Hy-Therm Gage Dynamic Calibration	71
24. Representative Dynamic Heat-Transfer Rate Data	73
25. Heat-Transfer Distributions at $M_\infty \approx 8$	77
26. Heat-Transfer Distributions at $M_\infty \approx 5.06$, $Re_\infty/ft = 6 \times 10^6$	78
27. Circumferential Heat-Transfer Rate Comparison between Static and Dynamic Data	79
28. Typical Heat-Transfer Distributions with Model Spinning, $p = 402$ deg/sec	80
29. Typical Heat-Transfer Distributions with Angle of Attack with and without Ablation	81
30. End of Transition Distribution, $r_n/r_b = 0.042$ Spherical, $M_\infty = 5.06$, $Re_\infty/ft = 6 \times 10^6$	82
31. End of Transition Distribution, $r_n/r_b = 0.12$ Spherical, $M_\infty = 5.06$, $Re_\infty/ft = 6 \times 10^6$	83
32. End of Transition Distribution, $r_n/r_b = 0.20$ Spherical, $M_\infty = 5.06$, $Re_\infty/ft = 6 \times 10^6$	84
33. End of Transition Mapping, $r_n/r_b = 0.042$ Spherical, $M_\infty \approx 5$	85
34. End of Transition Mapping, $r_n/r_b = 0.042$ Spherical, $M_\infty \approx 8$	86
35. End of Transition Mapping, $r_n/r_b = 0.042$ Biconic, $Re_\infty/ft = 3.6 \times 10^6$, $M_\infty \approx 5$ and 8	87
36. End of Transition Mapping, $r_n/r_b = 0.12$ Spherical, $M_\infty \approx 5$	88
37. End of Transition Mapping, $r_n/r_b = 0.20$ Spherical, $M_\infty \approx 5$	89
38. Unfiltered Aerodynamic Coefficients without Tare Correction	90
39. Representative Dynamic Aerodynamic Coefficient Data	91
40. Aerodynamic Coefficients for Sharp Cone at Angle of Attack	93
41. Posttest Photograph of Ablated Camphor Nose Tip, $r_n/r_b = 0.042$	94

<u>Figure</u>	<u>Page</u>
42. Aerodynamic Coefficients on Spinning Model with Camphor Nose Tip with Imbedded Metal Shaving	95
43. 3-DOF Model Motion - Laminar Boundary Layer	96
44. 3-DOF Model Motion - Turbulent Boundary Layer	97

TABLE

1. Test Summary	98
NOMENCLATURE	102

1.0 INTRODUCTION

During reentry, some vehicles experience disturbances which result in a rolling motion being imparted to the vehicle. It is thought that the rolling motion might skew the transition front distribution in the altitude régime where the boundary layer on the vehicle is transitional. Such an effect could contribute to the dispersion and be detrimental to the overall system performance. To investigate this effect, a test program was conducted at the Arnold Engineering Development Center (AEDC), von Kármán Gas Dynamics Facility (VKF), by the Space and Missiles System Organization (SAMSO) and the Defense Nuclear Agency (DNA). The overall objectives of the test program were to define the shape and movement of the boundary-layer transition zone and measure the lateral forces and moments on a spinning model undergoing boundary-layer transition. The primary test phase was a one-degree-of-freedom spin test which was conducted to measure extensive heat-transfer rate data for mapping the boundary-layer transition front. Measurements were also made simultaneously with a Magnus balance to obtain the resulting forces and moments. The secondary test phase was a 3-degree-of-freedom test in which model motions due to preset initial conditions were measured along with limited heat-transfer rate measurements. Variables which were investigated were model geometry, mass injection at the nose, simulated ablation, angle of attack, Mach number, Reynolds number, and spin rate.

One of the standard procedures for identifying a boundary-layer transition front is to record the heat-transfer or local temperature distribution along the model surface. For the stationary model, established test procedures using steady-state heat gages existed, but for a spinning model, new techniques using transient heat gage measurements were needed. The fast Fourier Transform technique was adapted to this purpose using three types of heat sensors. The primary type of sensor was a thermopile Gardon gage which is a heat flux sensor with a nominal output of 1.0 mv/Btu/(ft²sec) and a response time of 120 milliseconds (msec). The second type of sensor was a fast-responding (the order of microseconds) temperature sensor (temp-sensor) which when used in conjunction with a properly designed analog circuit produced an output which was proportional to the heat flux imposed on the sensor. The third type of sensor was a Schmidt-Boelter transducer (Hy-Therm®) which has a response very similar to the Gardon gage with a nominal output of 2.7 mv/Btu/(ft²-sec).

The test program reported herein was conducted in the AEDC-VKF Supersonic Wind Tunnel A and Hypersonic Wind Tunnel B at Mach numbers 5 and 8, respectively. Results were obtained at free-stream Reynolds number per foot ranging from 0.5×10^6 to 6×10^6 . Model spin rate ranged from 0 to slightly over 6,000 deg/sec at angles of attack

from -6 to +6 deg. Two 9-deg half-angle cone models were tested. A 15-in. base diameter model was tested on the spin mechanism, and a 10-in. base diameter model was tested using the AEDC-VKF 3 degree-of-freedom (3-DOF) system.

Selected results are presented to show the usefulness of the techniques which were developed to analyze dynamic heat-transfer measurements and to illustrate the effects of various parameters on the location of the boundary-layer transition front.

2.0 APPARATUS

2.1 WIND TUNNELS

The VKF Tunnels A and B are closed-circuit, continuous-flow, variable-density wind tunnels. Each tunnel is equipped with a model injection system which allows removal of the model from the test section while the tunnel remains in operation. The tunnels are depicted in Fig. 1.

Tunnel A has a 40- by 40-in. test section and an automatically driven flexible-plate-type nozzle which provides Mach numbers from 1.5 to 6. The tunnel operates at maximum stagnation pressures ranging from 29 psia at $M_{\infty} = 1.5$ to 200 psia at $M_{\infty} = 6$. Minimum operating pressures range from about one-tenth to one-twentieth of the maximum at each Mach number. The stagnation temperature can be varied from an average minimum of about 540°R to a maximum of 750°R, depending on Mach number and pressure level.

Tunnel B has an axisymmetric contoured nozzle and a 50-in.-diam test section. Tunnel B has two interchangeable nozzles to provide Mach numbers of 6 and 8 and operates over a range of stagnation pressure levels from 20 to 200 psia at $M_{\infty} = 6$, and 50 to 900 psia at $M_{\infty} = 8$. Each tunnel (throat, nozzle, test section, and diffuser) is cooled by integral, external water jackets.

A complete description of these tunnels is given in Ref. 1.

2.2 MODELS

The two models were supplied by PDA, Inc., and each consisted of a 9-deg half-angle cone. Each model was fabricated with an inner structure (liner) attached to the test mechanism (either a cylindrical or a 3-DOF gas bearing). Shells were supplied to fit over the liner to make up the particular model aerodynamic configuration. In addition, the nose tips could be changed to provide various nose geometries. Installation photographs of the spin model in Tunnel A and the 3-DOF model in Tunnel B are shown in Fig. 2. The cooling manifold arrangement for the Tunnel A installation is shown in Fig. 3. The models were cooled in the tunnel test section tanks using air following each injection into the tunnel flow.

The shells of both models were composed of sections which comprised four general types as shown in Fig. 4. The basic configuration for each model was a segmented, smooth aluminum type that was instrumented. Sections of each basic shell could be replaced with camphor (in the case of the larger spin model only, Fig. 5a), asymmetric aluminum (Fig. 5b), or carbon phenolic frustums (Figs. 5c-e) which were uninstrumented. The asymmetries on the aluminum frustums were roughness strips asymmetrically distributed around the frustum. Three types of the carbon phenolic frustums were tested.

The nose tip geometry was varied using a selection of tips and adapters. Nose bluntnesses from sharp to 1.50-in. radius, and geometries from hemispherical to biconic or flat could be selected (see Fig. 6a and b). In addition, camphor nose tips (Fig. 6c) could be used on the spin model with either camphor or aluminum frustums and on the 3-DOF model with the aluminum frustum. The mass injection nose tips (Fig. 6d) were only used on the spin model. Three types of mass injection tips were available: a gaseous jet (e.g. injection occurring through a pitot-pressure-type port), a porous wall blunt configuration, and a static orifice configuration (called "active trips") on a blunt nose. Porosities of the porous wall configurations were 10, 20, or 40 μ .

The nose tip adapters could be either smooth or grooved. The smooth adapter had a ring section which could be removed for installation of grit or sphere-type trips (see Fig. 7). There were two grooved adapters (Fig. 8). One type (called "Rectangular Grooved") featured grooves running along cone rays spaced every 12 deg and circumferential grooves every 0.075 in. The second type (called "Tollmein-Schlichtfin" or T/S) had grooves running 30 deg to the local cone ray also spaced every 12 deg around the adapter. This arrangement created a diamond crosshatching pattern. All grooves on both adapters were typically 0.020 in. wide and 0.015 in. deep.

2.2.1 Spin Model

The spin model (Fig. 4a) had a base diameter of 15 in. The aluminum shell contained 30 heat-transfer gages (20 Gardon, 7 temp-sensor, and 3 Hy-Therm gages). The shell was composed of three sections allowing all the different types of frustums to be tested. Adapter rings were used to fit the different frustums to the remaining sections of the aluminum shell (see Fig. 4). The full set of nose tips and grooved nose tip adapters were used in combination with the different types of frustums. The mass addition system was used only with the instrumented aluminum shell. The mass addition system will be discussed in Section 2.4.6.

2.2.2 3-DOF Model

The 3-DOF model (Fig. 4b) had a base diameter of 10 in. There were two basic aluminum shells which contained six heat gages (either Gardon or Hy-Therm) each and a carbon phenolic shell without antenna windows (Fig. 5c). One of the aluminum shells featured the antenna windows as detailed in Fig. 5e. The boundary-layer trip section was located just aft of the nose tips. Either a grooved section (Fig. 7) or a removable collar with 3 spherical 0.078-in.-diam balls or grit roughness elements was used as a trip. The grit was applied to either 1 or 2 segments (180 deg apart) that were 20 deg wide. A smooth collar for testing without boundary-layer trips, and a smooth mismatch collar which caused model misalignment asymmetry were also provided. The model also contained on board instrumentation supplied by PDA to measure three angular velocities (rate gyroes) and six heat rates and transmit these data by telemetry to a receiving antenna on the sting.

2.3 TEST MECHANISMS

2.3.1 Spin-Test Mechanism

The spin-test mechanism (Figs. 9 and 10) consisted of six subsystems: four component balance, cylindrical gas bearing, turbine, disk brake, slip-ring assembly, and nose mass addition system (not shown). The test mechanism was furnished by PDA with the exception of the brake system. The balance will be discussed in Section 2.4.4.

The cylindrical gas bearing provided a nearly frictionless support. The bearing surfaces consisted of a cylindrical section and two end pads. The cylindrical section (journal) could support 500 lb of lift or side force. The end pads could support axial-force loads from -40 to +80 lb with gaseous nitrogen supplied at a pressure of 600 psi to the gas bearing in an atmospheric environment. Nominal air bearing gap was 0.002 in. in an unloaded state.

The turbine comprised an impeller assembly of two rows of 60 blades each and four air jets set to impinge on the impeller blades (Fig. 10b). Air pressure was set to sustain 600 psi (total pressure) to the jets. The turbine spun the model in the positive roll direction according to normal sign conventions. The outer edge of the turbine drum was scribed with 72 black nonreflective lines in a radial pattern (see Fig. 10b), and the surface between each line was polished. This pattern was used in conjunction with light reflective transducers, to determine roll rate and position as will be discussed in Section 2.4.5.

The disk brake featured a single caliper brake with Micarta® pads and stainless steel disk. The disk was attached to the base plate of the model, and the caliper brake was attached to the support sting. The brake was operated by air at 30 to 40 psig. A foul circuit was imbedded in each pad to verify clearance during the data acquisition periods.

The slip-ring assembly had forty-six channels through which excitation power and instrumentation outputs were transferred from the spinning model to the conventional sting wiring (passed through the balance, see Fig. 10a). The slip ring was a commercially available unit and was supplied by PDA.

A Lexan® bumper (Fig. 10a) was mounted at the base of the model to limit the balance deflections and provide overload protection for the balance.

2.3.2 3-DOF Test Mechanism

Details of the 3-DOF test mechanism (VKF-3.A) are shown in Fig. 11. The balance consists of a spherical gas bearing pivot, a two-axes variable reluctance angular transducer, three light reflective phototransistors, a model release mechanism, and a model locking device.

The spherical gas bearing (Fig. 11) provided a nearly frictionless pivot which is desirable for dynamic stability testing at hypersonic speeds where it is necessary to minimize tare damping. The bearing can permit model oscillations up to ± 10 deg and unlimited motion in roll. The gas bearing of this mechanism had a load capacity to 300 lb of lift and 200 lb of drag.

The 3-DOF test mechanism provides several methods of initiating model motions. Models can be released from an initially pitched position with an initial yaw rate using the displacement arm and lock. Both of these initial conditions can be varied. The three rotating arms are usually used to lock the model before it reaches its angular limit on the bearing. Air jets are used to increase or decrease model roll rate when the model is in the locked position. These same air jets may be used to induce angular motion when the rotating arms are retracted.

2.4 INSTRUMENTATION AND MEASUREMENTS

2.4.1 Tunnel Instrumentation

Tunnel A stilling chamber pressure is measured with a 15-, 60-, 150-, or a 300-psid transducer referenced to a near vacuum. Based on periodic comparisons with secondary standards, the accuracy (a bandwidth which includes 95 percent of the residuals, i.e.

2-sigma deviation) of these transducers is estimated to be within ± 0.2 percent of reading or ± 0.015 psi, whichever is greater. Stilling chamber temperature is measured with a copper-constantan thermocouple with an accuracy of $\pm 3^\circ\text{F}$ based on repeat calibrations (2-sigma deviation).

Tunnel B stilling chamber pressure is measured with a 100- or 1,000-psid transducer referenced to a near vacuum. Based on periodic comparisons with secondary standards, the accuracy of the transducers is estimated to be within ± 0.1 percent of reading or ± 0.06 psi, whichever is greater for the 100-psid range and ± 0.1 percent of reading or ± 0.5 psi, whichever is greater for the 1,000-psid range. Stilling chamber temperature measurements are made with Chromel®-Alumel® thermocouples which have an accuracy of $\pm (1.5^\circ\text{F} + 0.375 \text{ percent of reading})$ based on repeat calibrations.

2.4.2 Heat-Transfer Gages

Heat-transfer rate gages were used in this program to determine the location of the boundary-layer transition fronts. Three types of gages were used; thermopile Gardon (primary), temp-sensor with analog circuits, and Schmidt-Boelter (called Hy-Therm). The Gardon and temp-sensor gages were designed and fabricated by VKF, and the Hy-Therm gages were purchased from Hy-Cal Engineering. The locations of the various gages are shown in Figs. 12 and 13.

2.4.2.1 Thermopile Gardon Gage

Steady-state heat-transfer-rate measurements were made with thermopile Gardon gages (Refs. 1 and 2) which are shown in Fig. 14a. These gages were designed, fabricated, and calibrated by the AEDC-VKF. The Gardon gages are 0.125 in. in diameter and have a constantan sensing foil nominally 2 mils in thickness mounted on a cylindrical copper heat sink. The thermopile rosette on the sensing foil was formed by a vacuum-depositing technique and consisted of alternating legs of antimony and bismuth, which provide an excellent thermocouple sensor. In this study, the output of the thermopile Gardon gage was nominally 1.0 mv/(Btu/ft²-sec) with a nominal operating temperature range of 60 to 300°F (above this temperature the gage elements begin to separate or fail). The thermocouple rosette is used to sense the temperature difference across the gage sensing foil, and this temperature difference is essentially proportional to the heat flux imposed on the constantan foil.

The sensing surface (constantan foil) of the gage was thinly coated with a black paint having a high thermal absorptivity so that the gages could be statically calibrated with a radiant heat source, in this case a set of quartz-iodide lamps. The accuracy of the

scale factors based on repeated calibrations against a secondary standard (2-sigma deviation) was estimated to be ± 5 percent (Ref. 2). A set of conventional or standard 0.25-in.-diam Gardon gages acts as a facility secondary standard for the purpose of statically calibrating all other thermopile Gardon gages. At various times, the calibration of these secondary standards is checked against slug calorimeters or working standards of other independent calibration facilities (such as Hy-Cal Engineering or the Heat Technology Laboratory). Dynamic heat-transfer-rate measurements were also made with these gages which had a slow response (nominally 120 msec); therefore, the gage output had to be corrected. A calibration procedure was developed to experimentally define the gage's dynamic response. The dynamic calibration equipment and procedure used will be described in Section 3.1.

The Gardon gage wall temperature measurements (i.e., the temperature of the outer edge of the constantan film) are normally made with iron-constantan thermocouples. However, the wall temperatures were not measured in this test because of the limited number of slip-ring channels and the error incurred by the slip-ring junction in the thermocouple circuit.

2.4.2.2 Temp-Sensor with Analog Circuit

The temp-sensor shown in Fig. 14b is basically a surface temperature measuring device which employs a low thermal conductivity (1.845×10^{-5} Btu/(ft²-sec-°F)) epoxy material (Stycast[®] 1090) as a substrate and a thin semiconductor silicon wafer (0.090 x 0.040 x 0.0005 in.) imbedded in the substrate with only one surface exposed. The substrate is considered to be a homogeneous, one-dimensional, semi-infinite solid. The silicon wafer has a high positive temperature coefficient of resistance of 5.0×10^{-3} ohms/(ohms-°F). The nominal output of the sensor was 4 mv/°F for a 5-v d-c excitation. The output of the temp-sensor is fed through a specially designed analog circuit (described below) so that the output from this circuit is proportional to the heat flux impinging on the temp-sensor. The useful operating or run time of this temp-sensor analog circuit unit is nominally 17 sec.

When utilizing temp-sensors in wind tunnel testing, it is generally desirable to compute the incident heat flux on the gage from the temperature history of the gage. This process requires a numerical integration over the total temperature history in question, which for large numbers of gages and high data sample rates can produce time-consuming computer analysis requirements. In order to reduce the required analysis time, an analog circuit was developed which would, in essence, perform the numerical integration of the temperature history and produce a voltage proportional to the incident heat flux on the gage. Analysis of the temperature history and the algorithm required to obtain heat flux showed that an analog circuit was needed whose gain increased at a

10-db/frequency decade slope and whose phase shift was 45 deg. This function cannot be exactly implemented electronically. However, the desired response can be approximated by staggering 20-db slopes (zero) and 20-db slopes (pole) at equal logarithmic spacings resulting in an average 10-db slope. The closeness of the approximation to the exact desired response is then a function of the closeness of the spacing of the circuit poles and zeros. The circuit which was utilized is an eight-pole, eight-zero circuit with the pole/zero spacing set every octave. This spacing can be shown to produce the desired 10-db/decade response to within ± 1 percent. The circuit covers the frequency range from 0.07 to 2,600 Hz.

2.4.2.3 Hy-Therm Gages

The Hy-Therm gages were purchased from Hy-Cal Engineering, Santa Fe Springs, CA. The gage is basically a Schmidt-Boelter transducer. Pertinent details of construction are shown in Fig. 14c. The output of the Hy-Therm is proportional to the heat-transfer rate and had a sensitivity generally of 2.7 mv/(Btu/ft²-sec).

2.4.3 Thermal Pulse Generator

A basic problem encountered in this study was the necessity of a technique to obtain a dynamic calibration of the heat gages. The primary problem was to apply a known short-duration (order of milliseconds) heat flux pulse to a heat gage to determine the gage transfer function. Several calibration systems were tested, and the system which was selected consisted of a projection lamp with a 3,150°K filament temperature, a high-speed shutter, and a lens to focus the radiant heat source on the gage surface, as shown in Fig. 15. The position of the lamp and the lens relative to the gage could be varied so that the level of the heat flux imposed on the gage surface could be varied from 1 to 20 Btu/(ft²-sec). The shutter (1-in.-diam) and the associated actuating systems could cycle (from closed to fully open to closed) in about 9 msec, and the calibrations were obtained for this shutter speed. About 3 msec were needed for the shutter to completely open or close. The 0.125-in.-diam heat gage was fully exposed to the heat source in less than half a millisecond. A photocell was used to detect the actual opening and closing of the shutter. The response time of the photocell is on the order of 50 microseconds (μ sec). The input to the heat gages was defined as a pure step function beginning and ending where the photocell output reached 20 percent of its full-scale value. The magnitude of the heat flux step imposed on the gage was established by holding the shutter open and measuring the heat flux with a secondary standard.

2.4.4 Four-Component Magnus Balance

Model forces and moments for the spin test were measured with a four-component, moment-type, strain-gage balance designed by VKF and fabricated by PDA (Fig. 16).

Three holes passed through the balance. One of these supplied the nitrogen to the gas bearing, and the other two provided passages for the instrumentation wiring to the slip-ring assembly. Small outrigger side beams of the balance with semiconductor strain gages were used to obtain the sensitivity required to measure small side loads while maintaining adequate balance stiffness for the larger pitch loads. When a yawing moment is imposed on the balance, secondary bending moments are induced in the side beams. Thus, the outrigger beams act as mechanical amplifiers, and a normal-force to side-force capability ratio of 10 was achieved for a 500-lb normal-force loading. Before testing, static loads in each plane and combined static loads are applied to the balance, simulating the range of model loads anticipated for the test. The following accuracies represent the bands for 95 percent (2-sigma deviation) of the measured residuals, based on differences between the applied loads and the corresponding values calculated from the balance calibration equations included in the final data reduction. The range of static loads applied and the measurement accuracies follow.

4.00-Y-34-076 Balance

<u>Component</u>	<u>Design Load</u>	<u>Range of Static Loads</u>	<u>Measurement Static Load Accuracy</u>
Normal Force, lb	± 500	± 250	±0.25
Pitching Moment*, in.-lb	±2,500	±1,900	±1.8
Side Force, lb	± 50	± 10	±0.02
Yawing moment*, in.-lb	± 250	± 70	±0.05

*About the balance forward moment bridge.

The transfer distance from the balance forward pitching moment bridge to the model moment reference location was 27.742 in. along the longitudinal axis and was measured with an estimated precision of ±0.005 in.

2.4.5 Tachometer and Roll Position

The rotational speed and roll position of the spin model were computed from the electrical pulses produced by a surface with alternating reflective and nonreflective surfaces passing two internally mounted infrared-emitting diodes and phototransistors (see Fig. 16). One transducer which was used to determine the rotational speed worked in conjunction with 72 alternating reflective and nonreflective surfaces fixed to the outer edge of the gas bearing (see Fig. 10b). The output of the transducer was fed to a

frequency-to-voltage converter whose output is an analog signal proportional to the spin rate of the model. The second transducer sensed a non-reflective surface only at the $\phi = 0$ position and allowed the model roll position to be defined with respect to time, i.e., $\phi = 0$ at $t = 0$. The roll rate accuracy is estimated to be ± 0.4 percent.

The initial roll position depends on the receipt of the roll position zero (i.e., $\phi = 0$) signal which could be in error due to the sampling rate of the data system. This error could be a bias equal to or less than the amount calculated as

$$(\text{Error in } \phi) = p \times 5.5 \times 10^{-4} \text{ sec}$$

The digital outputs from both transducers were recorded. In addition, the roll rate output was sent to a standard VKF Magnus control console to allow automatic control of the model spin rate. The desired spin rate was obtained by a comparator network which switched the turbine off when the voltage from the frequency-to-voltage converter equaled a pre-set voltage on the Magnus console. This console could be set in an automatic mode which turned the brake off, initiated the turbine, switched the turbine off, and at the appropriate time (i.e., when the model left the tunnel centerline), reset the brake. In addition, the brake and turbine could be manually controlled from the console.

2.4.6 Mass Addition System

The nose mass addition system (Fig. 17) was remotely fired from the Magnus Control Console. The system (Fig. 17a) comprised a 7,500 psi rated 40-in.³ bottle, pressure transducer, a squib-actuated valve, a regulator, and a mass injection nose tip. The on-board high-pressure bottle for the mass injection contained a Statham 5,000-psia transducer (Figs. 17a and b) to monitor the entrapped pressure. The estimated accuracy for this gage is ± 2 percent.

The valve (Figs. 17b and c) included a fill port for the high-pressure bottle and a normally closed flow passage. The mass flow through the valve was initiated by firing a squib which forced a piston to shear an insert blocking the passageway. The valve was refurbished after each operation by disassembling, cleaning, and replacing the squib and insert. The valve components are shown in Fig. 17c along with a photograph of a sheared insert after a valve operation.

Three regulators were used with the system (Figs. 17a and b): 10 psia, 30 psia, and 100 psia. These regulators provided mass flow rates of 0.002, 0.005, and 0.018 lbm/sec, respectively, depending somewhat on the nose tip used.

2.4.7 3-DOF Instrumentation

The 3-DOF instrumentation system provides a means of measuring the motion of a model by sensing the angular position of the spherical gas bearing. Two sets (pitch and yaw) of variable reluctance angular transducers set at orthogonal axes on the gas bearing housing provide continuous analog signals proportional to the angular displacements θ and ψ of the nonrolling axes.

The model roll position and roll velocity are measured with three light emitting and reflective light transistors. Two of the light transducers work in conjunction with alternating reflective and nonreflective lines fixed to the outer race of the gas bearing. One of these light transducers is out of phase (90 deg) with respect to a reflective line so that roll direction can be determined. The third light transducer senses a reflective line affixed to a bracket attached to the bearing which rolls with the model. The passing of this line over the light transducer resets the roll position counter at a predetermined zero roll position of the model. The outputs of the light transducers are input to a bidirectional counter which has an output corresponding to the roll position of the model. The output of the light transducers is also fed to a frequency-to-voltage converter which outputs an analog signal proportional to the roll velocity of the model. The angular position (θ , ψ , and ϕ) and roll velocity (p) signals are sent to the tunnel high-speed scanner which relays data to the VKF computer for data reduction.

3.0 TEST DESCRIPTION

3.1 DYNAMIC GAGE CALIBRATION

The Gardon gages, temp-sensors with analog circuits, and Hy-Therm gages were statically calibrated to determine their factors (i.e., (Btu/ft²-sec)/mv). In addition to these static calibrations, the dynamic response of these gages to a heat flux pulse was needed so that the transfer function of the gage could be evaluated. The thermal pulse generator used in this dynamic calibration was described in Section 2.4.3. The whole calibration procedure was accomplished in a semiautomatic mode of operation, using a small data acquisition computer. The shutter speed was set; the data recording system was activated; the lamp was turned on; the shutter was activated to open and close while the output from the photocell and gage were recorded as a function of time; and the lamp was turned off. A data sampling rate of 7.9×10^{-4} sec was used for the calibrations. The data reduction program was limited to 512 data samples, which means that the overall length of the signal recorded was 0.4 sec.

3.2 3-DOF TELEMETRY CALIBRATION

The telemetry instrumentation channels were calibrated periodically during the test (initially after each configuration change) by inputting a known signal to the TM package by means of a PDA calibration instrument and reading the outputs on the tunnel digital data system.

3.3 TEST CONDITIONS

The tests were conducted at Mach numbers 5 and 8 and free-stream Reynolds number per foot range between 0.5×10^6 and 6×10^6 . A summary of the test conditions is given below.

M_∞	p_o, psia	$T_o, ^\circ\text{R}$	q_∞, psi	$\rho_\infty \times 10^3, \text{lbm/ft}^3$	$V_\infty, \text{ft/sec}$	$h_o, \text{Btu/lbm}$	$Re_\infty/\text{ft} \times 10^{-6}$
5.03	42	659	1.36	1.90	2,572	160	1.8
5.04	87	675	2.79	3.81	2,604	163	3.6
5.06	150	680	4.74	6.42	2,616	165	6.0
7.90	100	1,150	0.49	0.35	3,576	278	0.5
7.92	120	1,210	0.58	0.40	3,670	293	0.6
7.95	250	1,245	1.18	0.79	3,724	301	1.2
7.99	550	1,305	2.54	1.62	3,813	316	2.5
8.00	850	1,350	3.90	2.40	3,880	327	3.6

A summary showing all the configurations that were tested is presented in Table 1.

3.4 TEST PROCEDURES

The desired test conditions were established in the wind tunnel, and then the procedures described in the following subsections were used to record the test data.

3.4.1 Spin Test Technique and Data Reduction

Model data (i.e., force and heat transfer) were obtained in either the pitch-pause or continuous sweep modes.

The spin dynamic data were obtained in the pitch-pause mode at predetermined α and p values. A preset delay was used after each spinup to allow the spin to stabilize and turbine-induced vibrations to dampen out. Each data group for this mode comprised 600 loops taken at a preset data loop period (DLP) depending on the spin rate shown below.

Spin Rates, p, <u>deg/sec</u>	DLP, <u>sec</u>
< 600	0.0093
600 < p < 1500	0.0047
>1500	0.0035 or 0.0023

For the dynamic data, the model was positioned at zero angle of attack, and the spin console settings were made for its automatic operation. The model was injected, the brake was released, the turbine was turned on, and the tunnel fairing doors were closed. When the model achieved the desired spin rate, the turbine was turned off, and the data recording sequence was initiated. As soon as the data were recorded, the brake was manually set, and the model was retracted and cooled. The block diagram of the systems used to record these data is shown in Fig. 18, and the sequence of events is outlined in Fig. 19. During the take data sequence, the RADS program waited until roll position zero (i.e., $\phi = 0$) was indicated before initiating the actual take data cycle for the multiverter channels.

The no spin, fixed ϕ data were obtained in the continuous sweep mode with sweep rates of 0.5 deg/sec and 1 deg/sec in Tunnel A and Tunnel B, respectively. The data were recorded at a DLP of 0.0093 sec until the sweep terminated.

The data were reduced by either of two techniques depending on the data type (i.e., static or dynamic). For the static data the raw data from the balance and heat gages were smoothed using the digital Kaiser-Bessel filtering technique. Then, the smoothed force data were corrected for first and second-order interactions and model weight effects. The corrected data were used to calculate the coefficients (C_N , C_m , C_Y , C_n , X_{cpN}/ℓ , and X_{cpY}/ℓ).

Conventional methods were used to calculate heat flux rates (Ref. 2) from the smoothed data, and this information was normalized in the form of Stanton numbers (referenced to the difference between tunnel stilling chamber temperature (T_o) and an assumed model surface temperature of 540°R). This constant T_w was requested by PDA to compute Stanton number. An adjustment was made to the calculated Stanton numbers to account for gage installation effects. This adjustment was determined in the following manner:

1. Data were recorded at $\alpha = 0$ for the 1.5-in.-radius nose at a condition in which a laminar boundary layer existed over the model. A fairing based on analytical results was drawn through the experimental values, and if any points deviated from this fairing, the results were adjusted by the equation:

$$\left[S_{t_{\infty} \text{ adjusted}} = K_N (S_{t_{\infty} \text{ adjusted}}) \right]$$

to move them near the faired curve.

2. Data were then recorded at $\alpha = 0$ for the sharp nose at the highest Reynolds number so that most of the gages were in the region of a turbulent boundary layer. A new set of K_N was then determined, as before, for each gage in the turbulent region. The two adjustment factors (K_N) for each gage were then compared, to determine an adjustment factor that was used for that gage for all of the test results.

Conventional data reduction techniques along with the adjustment factors were combined with a Fast Fourier Transform (FFT) technique for calculating the dynamic heat-transfer data. The procedure for analyzing transient sensor output signals which are produced by undefined input signals are well documented (Refs. 3 and 4). Any transient signal can be viewed in the frequency domain as a spectrum (amplitude distribution of the real and imaginary terms as a function of frequency), and the FFT algorithm provides the numerical procedure needed to transform digitally recorded transient data from the time domain into the frequency domain. Brigham (Ref. 5) has suggested that the FFT, in many respects, is analogous to using natural (or common) logarithms as a means of substituting simple arithmetic operations such as addition and subtraction for multiplication and division. In the frequency domain, certain numerical operations on a function such as convolutions, correlations, energy content, and discrete digital filtering can be performed quite simply. In particular, the FFT can be used to determine the response or transfer function of a linear measuring system which is defined in terms of the distorted output of a sensor and the known calibration pulse which caused the sensor response. A computer calculates the Fourier transforms of both the input and output time histories, and ratios the two transforms to obtain the transfer function of the sensor (Fig. 20). It should be noted that the Gardon gage, Hy-Therm gage, and the temp-sensor with its analog circuit are assumed to be functioning as linear measuring systems over the frequency range of interest in this test program.

When a transient of the sensor is recorded, the distorted output is digitized, transformed into the frequency domain using the FFT, and multiplied by the previously calculated sensor transfer function. This process produces a frequency-domain version of the unknown input signal from which sensor distortion has been supposedly removed. Transformation back into the time domain will now reproduce the unknown input signal, free of distortion.

A typical dynamic Gardon gage calibration is presented in Fig. 21. The idealized input and the gage output are presented as a function of time. The short input pulse is required so that the higher frequencies are adequately defined. The spectrum of the gage output shows that the signal does not contain any measurable frequency components at frequencies greater than 100 Hz. The Fourier transforms of the input and output were combined to produce the transfer function presented in Fig. 21b according to the equation:

$$H(f) = I(f)/O(f) = T[I(t)]/T[O(t)]$$

where

I = input signal
 O = output signal
 T = transform
 H = transfer function
 t = time, sec
 f = frequency, Hz

The amount that the various frequency components are amplified and phase-shifted is clearly indicated. It should be noted that the 60-cycle noise in the gage output is clearly indicated in Fig. 21a and could easily be digitally filtered. Furthermore, it is not necessary to know the exact heat flux input in order to determine the transfer function. Since the static scale factors are available, the magnitude term can be normalized by the d-c or zero frequency value. The Gardon gage transfer function is well defined up to 60 Hz, and the amplification is about 40.

A typical dynamic calibration of a temp-sensor with an analog circuit is presented in Fig. 22. The calibration procedure used is the same as that used for the Gardon gages. For approximately the same heat flux input, the output of the temp-sensor is about 1,000 times greater than that of the Gardon gage. The greater output is indicated by the high-frequency signal content of the signal spectrum. The transfer function (Fig. 22b) is well defined up to 320 Hz, and the amplification is about 4.

The temp-sensor is sensitive to light as well as heat. This photoelectric effect, in conjunction with the analog circuit, produces a large spike in the gage output when the shutter opens or closes. The effect is a very high frequency response and is not believed to influence the transfer function in the frequency range of interest.

A dynamic calibration of a Hy-Therm gage is presented in Fig. 23. The output of the Hy-Cal gage is about three times that of a Gardon gage for the same heat transfer rate. The transfer function (Fig. 23b) is well defined up to about 90 Hz where the amplification is about 60.

It should be noted that the data sample rate can have a considerable effect on accurately defining the input and output signals. If they are not defined properly, the null points (e.g., Fig. 22a) of the input and output transforms will not match, and the transfer function will have gross errors.

The dynamic data were reduced in the manner indicated in Fig. 20 using the FFT program and 512 data samples, and the Fourier transforms of both the input and output calibration signals were obtained. These were then ratioed to obtain the transfer function of the gage. This transfer function was multiplied by the Fourier transform of the distorted data signal which was obtained during the test. This resulted in a reconstructed input signal (or inferred the gage input) without distortion once it was transformed back into the time domain (using the inverse transform).

The high-frequency noise was digitally filtered from the gage data signal by setting both the magnitude and the phase angle of the gage transfer function to zero for selected frequencies. Listed below are the high-frequency filtering ranges for each model spin range.

<u>Model Spin Rate,</u> <u>P,</u> <u>deg/sec</u>	<u>Cutoff Frequency, Hz</u>
< 700	15
<2,000	20
<5,000	70
<12,000	100

A dynamic response function for the balance was not determined. The FFT was used primarily as a means to filter the force data, resolve the data as a function of roll position, and account for model dynamics such as unbalance. The frequencies were filtered (i.e., magnitude set to zero at the specified frequencies) as shown below:

<u>Model Spin,</u> <u>deg/sec</u>	<u>Filtered Frequencies, Hz</u>	
	<u>Normal Force</u> <u>and Pitching Moment</u>	<u>Side Force</u> <u>and Yawing Moment</u>
0 to 600	>4.5	>4.5
1,300	>6.0	>6.0
3,300	>25	>11.5
4,000	>25	6 to 9.5, >11.5
6,500	>25	6 to 15, >19

The unbalance was recorded by spinning the model while it was retracted from the tunnel flow. The spin was set to the same rate as that of the test data. These data (called "tank tares") were filtered and resolved as a function of roll position and then subtracted from the test data.

The procedures used for processing the dynamic data were adapted from the work reported in Ref. 6.

3.4.2 3-DOF Test Technique and Data Reduction

Before testing, each configuration was spun up and released near $\alpha = 0$ at atmospheric conditions, and data were recorded from which the model unbalance could be determined.

When the desired test conditions were established, the model was injected into the tunnel at $\alpha = 0$. The model was spun to an initial roll velocity which varied from -700 to +700 deg/sec. The rotating arms were retracted, and the initial pitch and yaw conditions were established by air jets.

Outputs from the angular position, angular velocity, and heat rate instruments were input to a high-speed digital converter which relayed the digital data to a disk file every 0.0052 sec. The results of pretest calibrations of the angular position instruments and heat gages along with calibration of the rate gyroes supplied by PDA were read into the data reduction program as card constants. These data together with telemetry instrumentation calibrations taken several times during the test were used to compute the model attitude, angular velocity, and heat rates which were tabulated, plotted, and put on digital tapes.

The final data reduction to moment coefficients will be accomplished by PDA using the information supplied on digital tape. Representative results are presented herein to illustrate the model motion data.

4.0 ACCURACY OF MEASUREMENTS

4.1 TEST CONDITIONS

The accuracy of the basic measurements (p_o and T_o) was discussed in Section 2.4.1. Based on repeat calibrations, these errors were found to be

$$\frac{\Delta p_o}{p_o} \times 100 = 0.2 \text{ percent and } \frac{\Delta T_o}{T_o} \times 100 = 0.5 \text{ percent at } M_\infty = 5$$

and 0.1 percent and 0.4 percent, respectively at $M_\infty = 8$.

Uncertainties in the tunnel free-stream parameters and the model aerodynamic coefficients were estimated using the Taylor series method of error propagation, Eq. (1):

$$(\Delta F)^2 = \left(\frac{\partial F}{\partial X_1} \Delta X_1 \right)^2 + \left(\frac{\partial F}{\partial X_2} \Delta X_2 \right)^2 + \left(\frac{\partial F}{\partial X_3} \Delta X_3 \right)^2 + \dots + \left(\frac{\partial F}{\partial X_n} \Delta X_n \right)^2 \quad (1)$$

where ΔF is the absolute uncertainty in the dependent parameter $F = F(X_1, X_2, X_3, \dots, X_n)$ and X_n is the independent parameter (or basic measurement). ΔX_n is the uncertainty (error) in the independent measurement (or variable).

The accuracy (based on 2-sigma deviation) of the basic tunnel parameters (p_o and T_o) (see Section 2.4.1) and the 2-sigma deviation in Mach number determined from test section flow calibrations were used to estimate uncertainties in the other free-stream properties using Eq. (1). The computed uncertainties in the tunnel free-stream conditions are summarized in the following table:

		Test Condition Uncertainty (\pm), percent					
M_∞	$Re_\infty/ft \times 10^{-6}$	M_∞	q_∞	ρ_∞	V_∞	h_o	Re_∞/ft
5.03	1.8	0.5	2.0	1.9	0.3	0.5	1.4
5.04	3.6	0.5	2.0	1.9	0.3	0.5	1.4
5.06	6.0	0.5	2.0	1.9	0.3	0.5	1.4
7.90	0.5	0.4	1.8	1.8	0.2	0.4	1.2
7.92	0.6	0.4	1.8	1.8	0.2	0.4	1.2
7.95	1.2	0.4	1.8	1.8	0.2	0.4	1.2
7.99	2.5	0.3	1.4	1.3	0.2	0.4	1.0
8.00	3.6	0.3	1.4	1.3	0.2	0.4	1.0

4.2 SPIN TEST DATA

The accuracy of the static heat-transfer data reduced in the form of Stanton number cannot be accurately determined because of the unknown wall temperature. The data reduction of the dynamic data is further complicated by the transfer function and FFT data reduction technique. However, for the heat-transfer rate (\dot{q}), the accuracy is estimated to be ± 5 percent for the Gardon gages. Therefore, the test results should be used only to identify transition front location and not for establishing absolute levels.

The balance accuracies (Section 2.4.4) were combined with uncertainties in the tunnel parameters, using the Taylor series method of error propagation, to estimate the uncertainty of the aerodynamic coefficients, and these are presented below:

M_∞	Re_∞/ft $\times 10^{-6}$	Static Data (b = 0) Uncertainty (\pm) at Maximum Measured Coefficient Value			
		C_N	C_m	C_Y	C_n
5.03	1.8	0.004	0.0027	0.00041	0.00021
5.04	3.6	0.004	0.0027	0.00040	0.00020
5.06	6.0	0.004	0.0026	0.00040	0.00020
7.92	0.6	0.004	0.0028	0.00041	0.00021
7.95	1.2	0.004	0.0025	0.00037	0.00019
8.00	3.6	0.003	0.0015	0.00027	0.00014

The basic precision of the aerodynamic coefficients was also computed using only the balance uncertainty along with the nominal test conditions, using the assumption that the free-stream flow nonuniformity is a bias type of uncertainty which is constant for all test runs. These values, therefore, represent the data repeatability expected and are especially useful for detailed discrimination purposes in parametric model studies.

M_∞	Re_∞/ft $\times 10^6$	Static Data (b = 0) Repeatability (\pm) Measured Coefficient Value			
		C_N	C_m	C_Y	C_n
5.03	1.8	0.0010	0.0006	0.00008	0.00005
5.04	3.6	0.0005	0.0003	0.00004	0.00002
5.06	6.0	0.0003	0.0020	0.00002	0.00001
7.92	0.6	0.0020	0.0010	0.00020	0.00010
7.95	1.2	0.0010	0.0007	0.00010	0.00006
8.00	3.6	0.0010	0.0002	0.00003	0.00002

For the dynamic data, there are insufficient means to determine the uncertainties in the force results. The transfer function for the balance was not determined, and the effect of support-induced acceleration forces could not be properly analyzed.

Measurement of the tunnel model-support system attitude in pitch is accurate within ± 0.05 deg based on repeat calibrations. Model attitude corrections were made for balance and sting deflections under air load, and the accuracy of the final model mean angle of attack is estimated to be ± 0.07 deg. The accuracy of the model roll angle (ϕ) is estimated to be in the range from -0.3 to -3.3 deg as discussed in Section 2.4.5 with a roll rate accuracy of ± 0.4 percent.

4.3 3-DOF TEST DATA

The θ and ψ data are presented in the tunnel axis system. A summary of the data uncertainties is given below:

θ, ψ	± 0.10 deg
ϕ	± 2 deg
I_x, I_y, I_z	± 1 percent
Model unbalance	± 0.075 in-lb
Tilt of Principal Inertia Axis	< 0.018 deg

5.0 RESULTS AND DISCUSSION

Typical data from the heat-transfer-rate gages are shown in Fig. 24. The uncorrected St_{∞} is shown for reference with its frequency spectrum. It is seen, by comparing the uncorrected St_{∞} in Figs. 24a and b, that the signal is greatly attenuated by the increasing spin. The transfer function was applied to both signals (see Section 3.4) to generate the corrected St_{∞} (plotted versus time and ϕ in each of the figures). Note that this correction brings Figs. 24a and b into very close agreement.

The response of the temp-sensor and Hy-Therm gages are shown by the plots in Figs. 24c and d. At this spin, it is easily seen that the temp-sensor has a much better response than the Hy-Therm (compare the uncorrected St_{∞} values). The temp-sensor time limitation (Section 2.4.2) and some unexplained noise problems with those gages made the data much less dependable than that of the Gardon gages. Therefore, the results presented, henceforth, will be limited to the Gardon gage data which have been corrected for dynamic response. Sufficient data were obtained with the temp-sensors to substantiate the Gardon gage results at the high spin rates.

The Stanton number data in Fig. 24 show an asymmetry about the $\phi = 180$ deg position. Analysis of data from other adjacent gages for several spin levels indicate a randomness in this asymmetry. Some gages might have the peaks and valleys shifted to

the right of the 180-deg position, whereas adjacent gages might have the curves shifted to the left of the 180-deg position. It is assumed that if the asymmetry were due to spin all the gages would show a shift in the same direction. An explanation of this asymmetry is provided by analyzing the data reduction procedures (see Fig. 20). At a spin on the order of 6,000 deg/sec, the Gardon gage results would have been phase shifted [see Fig. 21b] approximately 115 deg by the FFT data reduction procedure. The asymmetry in Fig. 24b is approximately 16 deg at this spin level, a relatively small value compared to the phase shift. Therefore, it is concluded that the asymmetry is not due to the spin but due to the phase angle incorporated in the data reduction.

The heat-transfer-rate distributions along the model are shown in Figs. 25 and 26 for the two Mach numbers. There is no significant effect of spin on the distributions in the turbulent (Fig. 25a), laminar (Fig. 25b), or transitional (Fig. 26c) flow regimes. The theoretical results show good agreement with the data.

The agreement between static heat transfer and dynamic heat transfer is further illustrated by Fig. 27. The model was held fixed at several roll positions, and the model was swept from -6 to +6 deg angle of attack to obtain the static data shown at $\alpha = 3$ deg by the circles. There is good agreement between the static and dynamic results. The static data served to confirm such characteristics as the dip at $\phi = 180$ at $x/\ell = 0.609$ in the dynamic results caused by the transitional nature of the boundary layer on the lee side of the model.

The behavior of the heat-transfer rate around the model at the instrumented locations is shown in Fig. 28 for $r_n/r_b = 0.042$ at $M_\infty = 8$, $p = 402$ deg/sec, $Re_{\infty}/ft = 3.6 \times 10^6$, and $\alpha = 3$ deg. These data show transition beginning at $x/\ell = 0.461$ on the leeward side ($\phi = 180$ deg) and between $x/\ell = 0.609$ and 0.700 on the windward side ($\phi = 0$). At the base of the model, the flow appears to be fully turbulent completely around the model.

The distribution along the top-ray of the model for the continuous sweep static data is illustrated in Fig. 29. At angles of attack less than approximately -4 deg (gages on windward side), the boundary layer is turbulent at the most forward gage. Conversely at $\alpha = 0$, the boundary layer begins to transition near the base. Transition begins on the leeward side (i.e., $\alpha > 3$ deg) at $x/\ell = 0.461$. Also shown in Fig. 29 is the effect of ablation on the heat-transfer rate and boundary-layer transition. For the extent of camphor surface of this test, the ablation delayed transition for $-6 < \alpha < -3$ deg as noted at $x/\ell = 0.609$ and 0.700 .

Heat-transfer-rate results for nose bluntness ratios (ratio of nose radius-to-base radius) of 0.042 spherical, and 0.042 biconic, 0.12 spherical, and 0.20 spherical are presented in the following figures. The end of transition (as defined in Figs. 25 and 26) is plotted for the various spin rates and angles of attack in Figs. 30 through 32. The scatter in the data is within one gage location upstream or downstream of the data fairing for the transition location.

In Fig. 30, for $r_n/r_b = 0.042$, there is a slight asymmetry at $\alpha = 1.2$ deg which does not appear in the $\alpha = 0$ or higher angle of attack data. In addition, the distribution at $\alpha = 0$ is symmetric but shows a region at 90 deg and 270 deg where transition is farther aft. Transition at $\alpha = 6$ deg on the leeward side is ahead of the first gage and is, therefore, indeterminate. The transition front distributions for the more blunt configurations (see Figs. 31 and 32) are very similar. The end of transition at $\alpha = 0$ is uniform for each configuration. For $r_n/r_b = 0.12$ at $\alpha = 1.2$ deg (Fig. 31), there is again a slight asymmetry in the front which does not appear at the other angles of attack. It should be noted that in all three figures (i.e., 30 through 32) there is no evident effect of spin on the transition front location. In Figures 30 and 31, data were available at 45-deg intervals from static-type pitch series which agrees within one gage location with the dynamic-type spin data.

In Figs. 33 through 37, the end of transition is shown located on a foldout of the cone for various angles of attack and nose configurations. In general, the maps are symmetric and represent wide ranges of spin as noted in each figure. No measurable effect of spin on the end of boundary-layer transition could be detected. Note that the shape of the transition front is sensitive to nose geometry, Mach number, Reynolds number, and angle of attack. That is, increasing the nose bluntness and Mach number moved the transition rearward; increasing the Reynolds number moved transition forward. Angle of attack effects were geometry dependent.

Representative force data are shown in Figs. 38 and 39 to illustrate the dynamic data reduction (see Section 3.4.1). The reduced data without filtering and tare corrections for C_Y and C_n are typified by the two plots in Fig. 38. The data show large frequency content and a non-zero level. These force data were filtered and corrected for tank tares (see Section 3.4.1) routinely. The quality of the reduced data are shown in Fig. 39 for the same group of data shown in Fig. 38. There is good agreement between the normal-force and pitching-moment coefficients (Fig. 39a) from the static and dynamic results. In Fig. 39b, the tank tare shows the same non-zero level exhibited in the uncorrected C_Y and C_n (Fig. 38). The reduced aerodynamic data shows a negligible C_Y and C_n level at these test conditions.

Representative force data are shown in Fig. 40 for various spin and static groups. Static Newtonian theory shows good agreement with these data. In all respects, the aerodynamic normal force and moments are unaffected by spin.

In two cases, a side force was measured that was periodic for the spinning model. Both cases were groups where the same camphor nose tip was used. Close examination of pretest and posttest photographs show a small metal shaving (see Fig. 6c and Fig. 41) imbedded in the nose approximately 4 in. from the tip. A plot of the pitching-moment, side-force, and yawing-moment data are shown in Fig. 42 for a typical set of data obtained with this nose tip. These latter data are presented to confirm the confidence that the balance could resolve rather small forces and moments on the order of the stated uncertainties in Section 4.2.

All the force data analyzed from this test showed no measurable effect of spin. Collaboration of this conclusion was evidenced by the lack of any spin effect on the boundary-layer transition front.

Motion plots from the 3-DOF test are illustrated in Figs. 43 and 44 for a sharp cone with and without trips (i.e., turbulent and laminar boundary layers, respectively). Two spin rates for each configuration are shown. Analysis of the motion data will be made by PDA.

6.0 SUMMARY

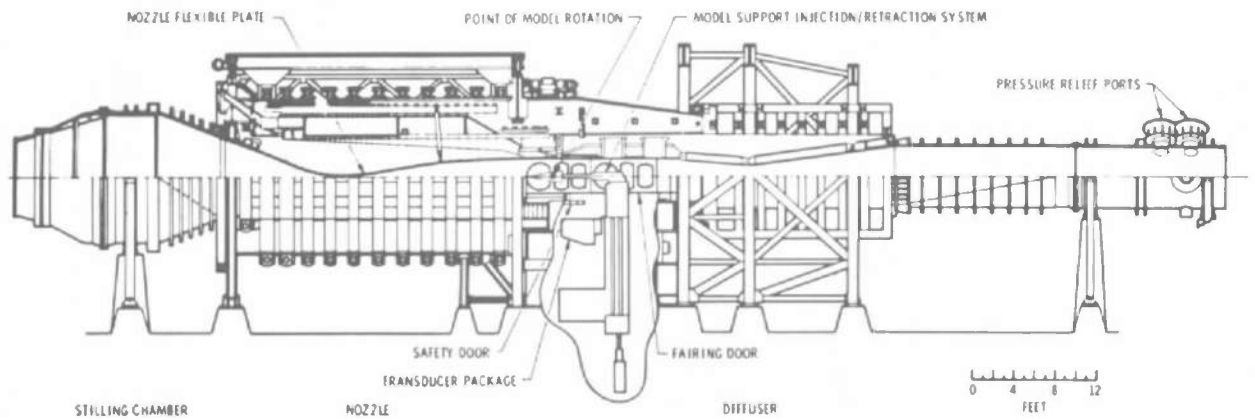
In summary, the data from this program indicate no effect of spin on the measured force and moment data. In addition, the heat-transfer-rate data shows no skewing of the boundary-layer transition front due to the model spin.

The test data showed that increasing the nose bluntness and Mach number moved the end of boundary-layer transition rearward on the model. As expected, increasing the Reynolds number moved transition forward. The effects of angle of attack on the distribution of the end of transition was dependent on the nose geometry.

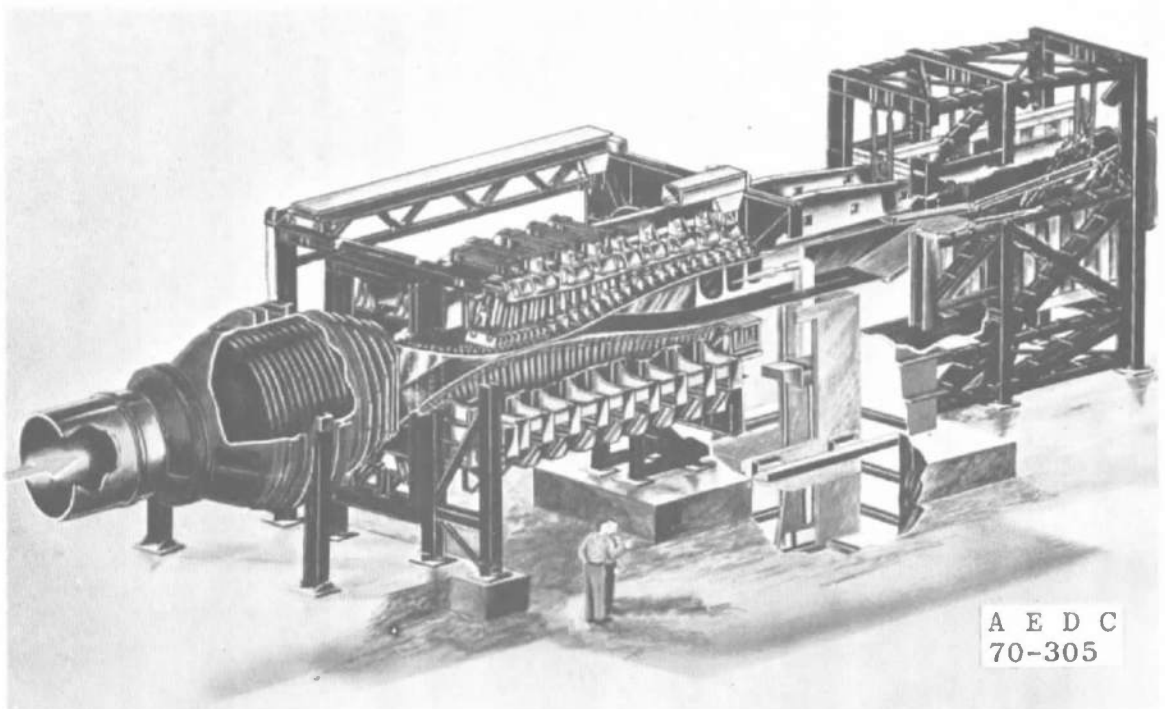
The comparisons between the static and dynamic heat-transfer and force data results confirm that the spin technique is a practical and valuable technique for making transient aerodynamic measurements. The FFT technique provides a useful analysis tool to extract data from the Gardon gage using the transfer function when the Gardon gage is used for measuring transient signals. Continuous sweep heat-transfer-rate data provides useful data for determining transition locations.

REFERENCES

1. Test Facilities Handbook (Tenth Edition). "Von Kármán Gas Dynamics Facility, Vol. 3," Arnold Engineering Development Center, May 1974.
2. Trimmer, L. L., Matthews, R. K., and Buchanan, T. D. "Measurement of Aerodynamic Heat Rates at the AEDC von Kármán Facility." ICIASF '73, Institute of Electrical and Electronics Engineers, Inc., New York, 1973.
3. Harting, Darrell R. "Digital Transient-Test Techniques." Experimental Mechanics. Vol. 12, No. 7, July 1972, pp. 335-340.
4. Bickle, L. W. and Dove, R. C. "Numerical Correction of Transient Measurements." ISA Transactions, Vol. 12, No. 3, 1973, pp. 286-295.
5. Brigham, E. O. The Fast Fourier Transform, Prentice Hall, Inc., Englewood Cliffs, New Jersey, 1974.
6. Jenke, Leroy M. and Strike, W. T. "Boundary-Layer Transition Mapping on an Oscillating 4-deg Cone in a Hypersonic Stream by Means of Dynamic Heat-Transfer Measurements." AEDC-TR-77-108 (ADB025135L), February, 1978. Also AIAA Paper 78-778 presented at the 10th AIAA Aerodynamic Test Conference, San Diego, California, April 19-21, 1978.
7. Adams, John C., Jr. "Implicit Finite-Difference Analysis of Compressible Laminar, Transitional, and Turbulent Boundary Layers along the Windward Streamline of a Sharp Cone at Incidence." AEDC-TR-71-235 (AD734535), December 1971. Also AIAA Paper No. 72-186, January 1972.
8. Patankar, S. V. and Spalding, D. B. Heat and Mass Transfer in Boundary Layers. CRC Press, Cleveland, 1968.



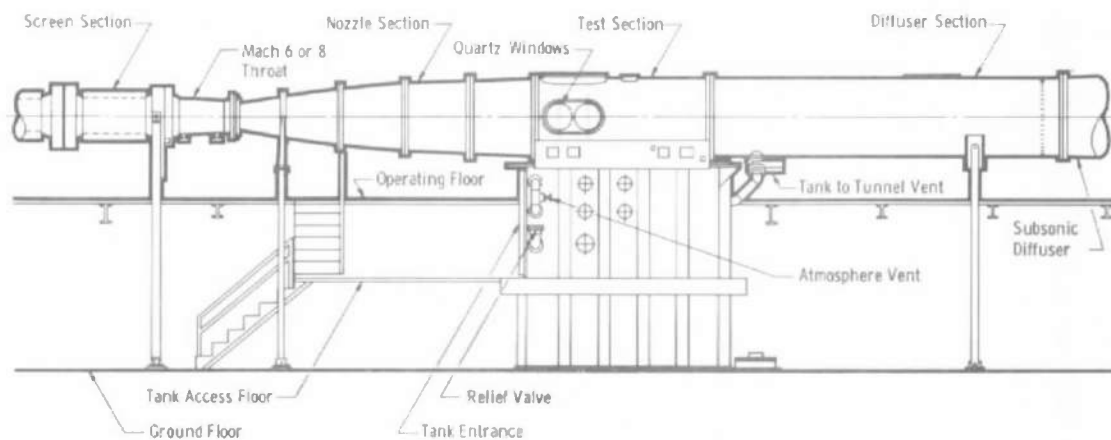
Tunnel Assembly



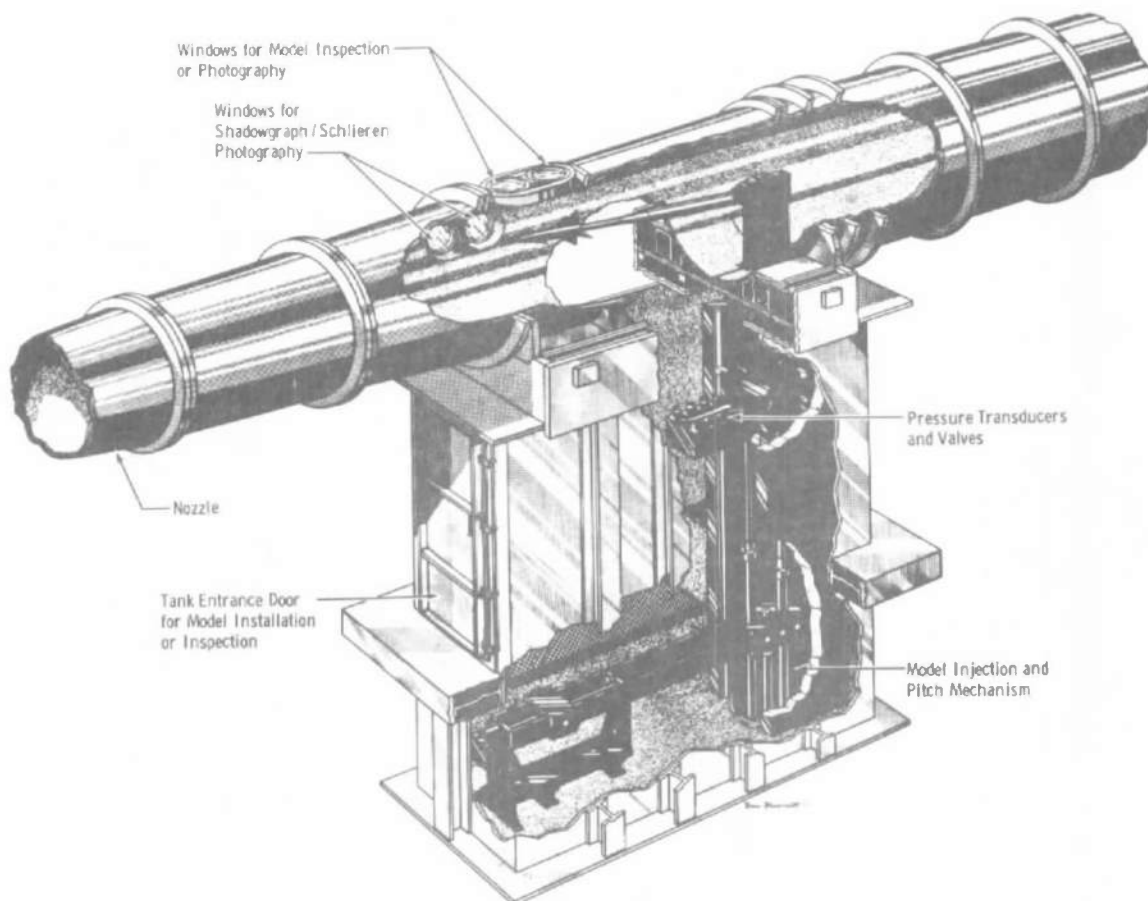
Tunnel Test Section

a. Tunnel A

Figure 1. Test facilities.

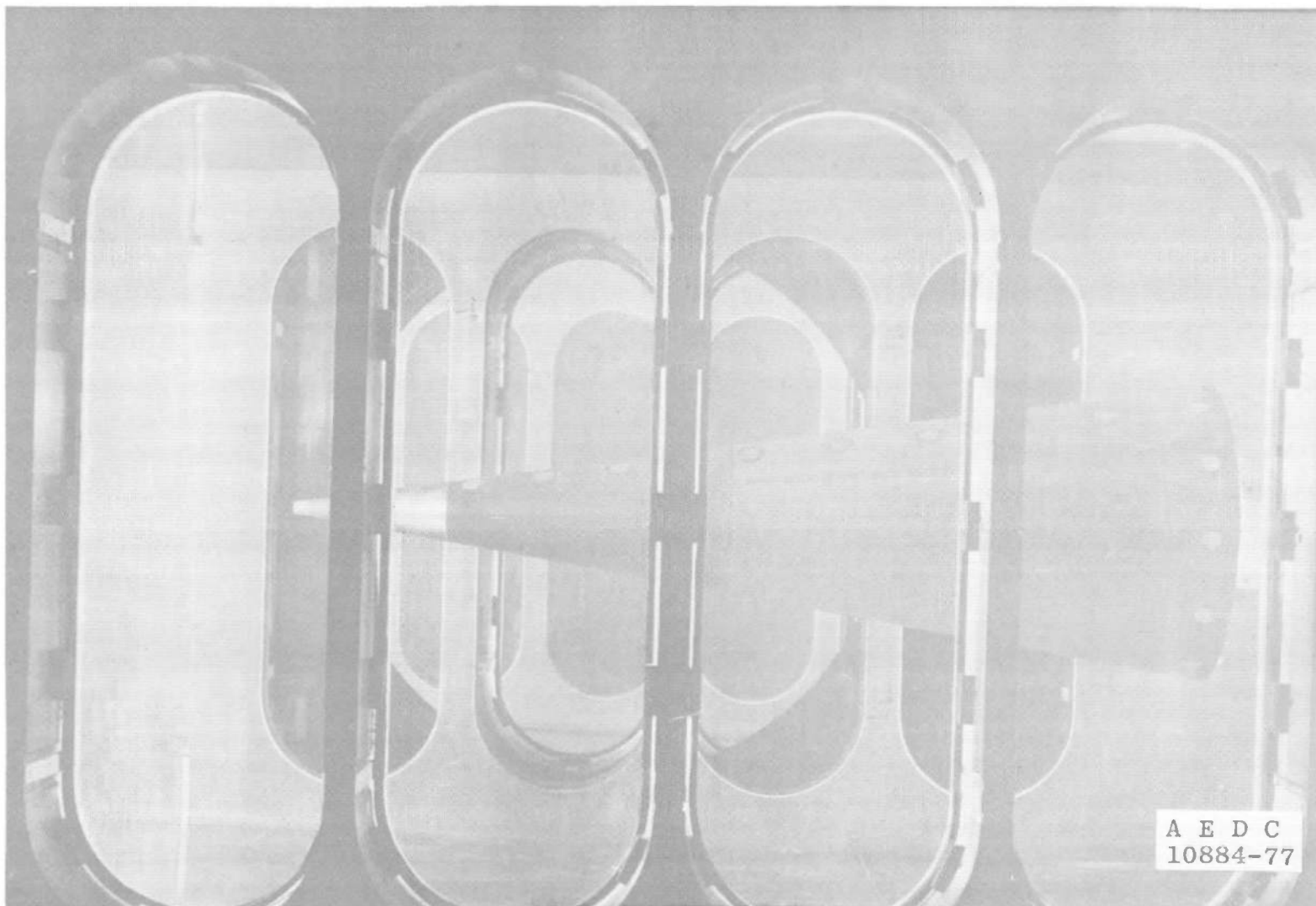


Tunnel Assembly

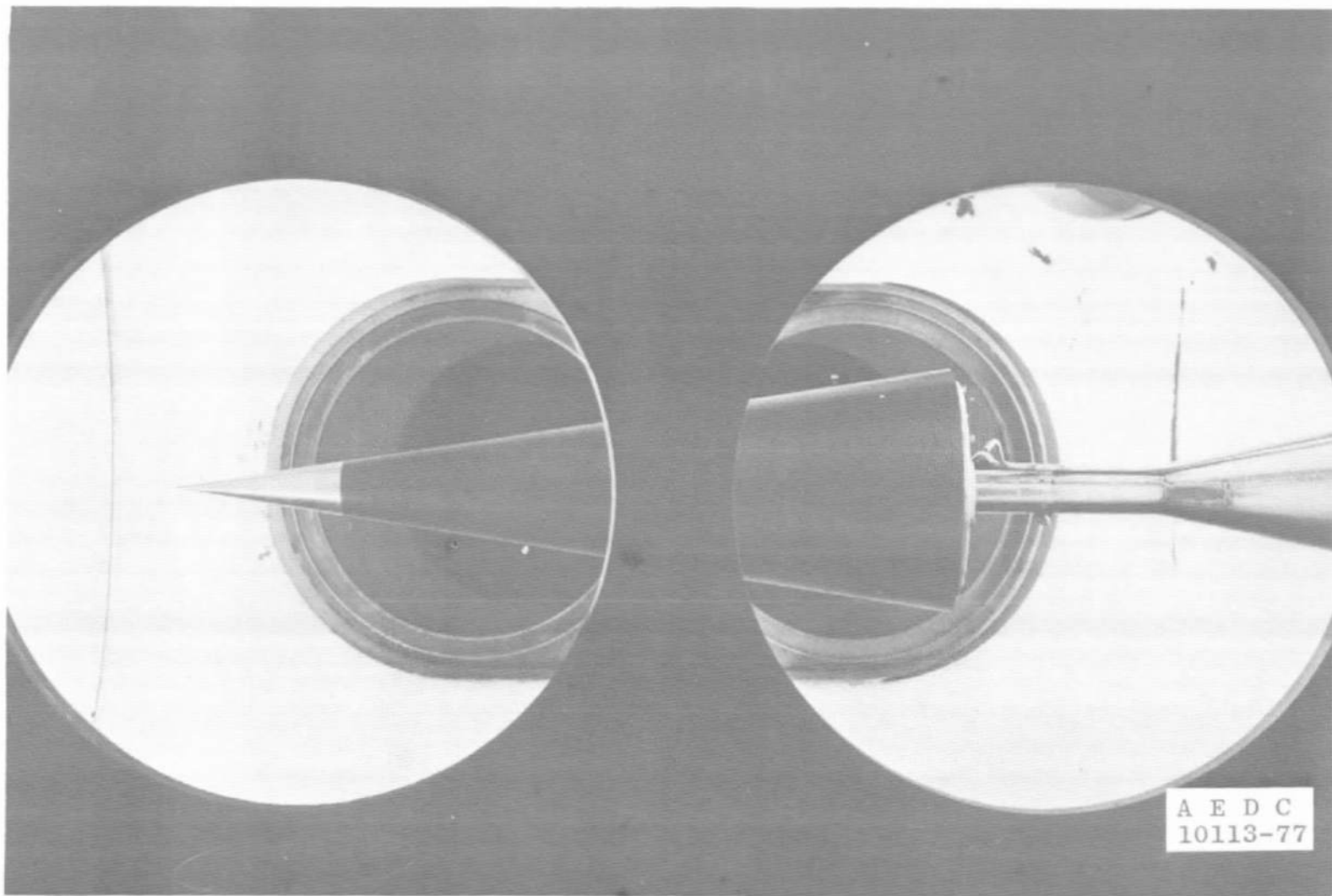


Tunnel Test Section

b. Tunnel B
Figure 1. Concluded.



a. Spin model in Tunnel A
Figure 2. Photographs of model installations.



b. 3-DOF model in Tunnel B
Figure 2. Concluded.

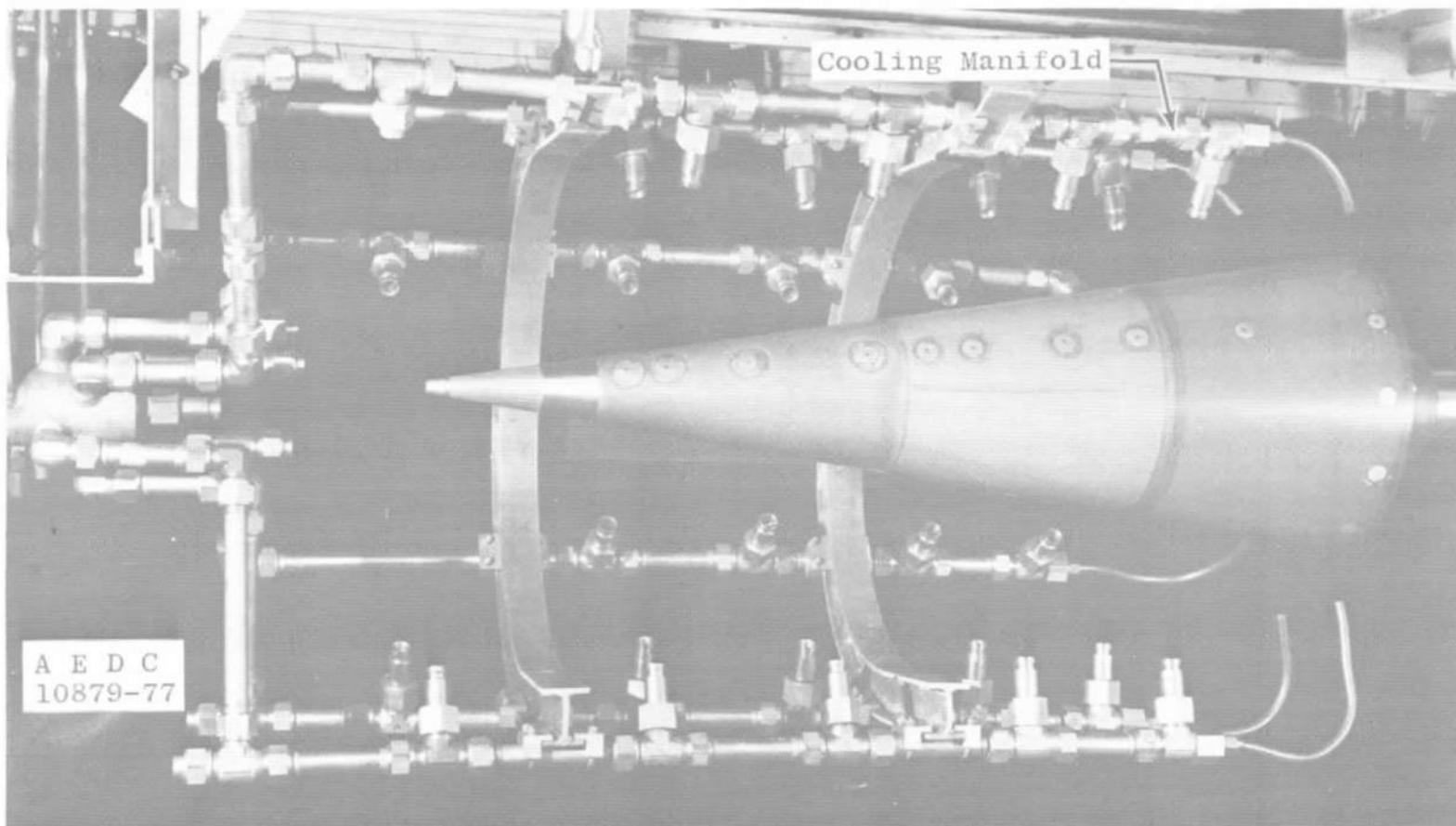
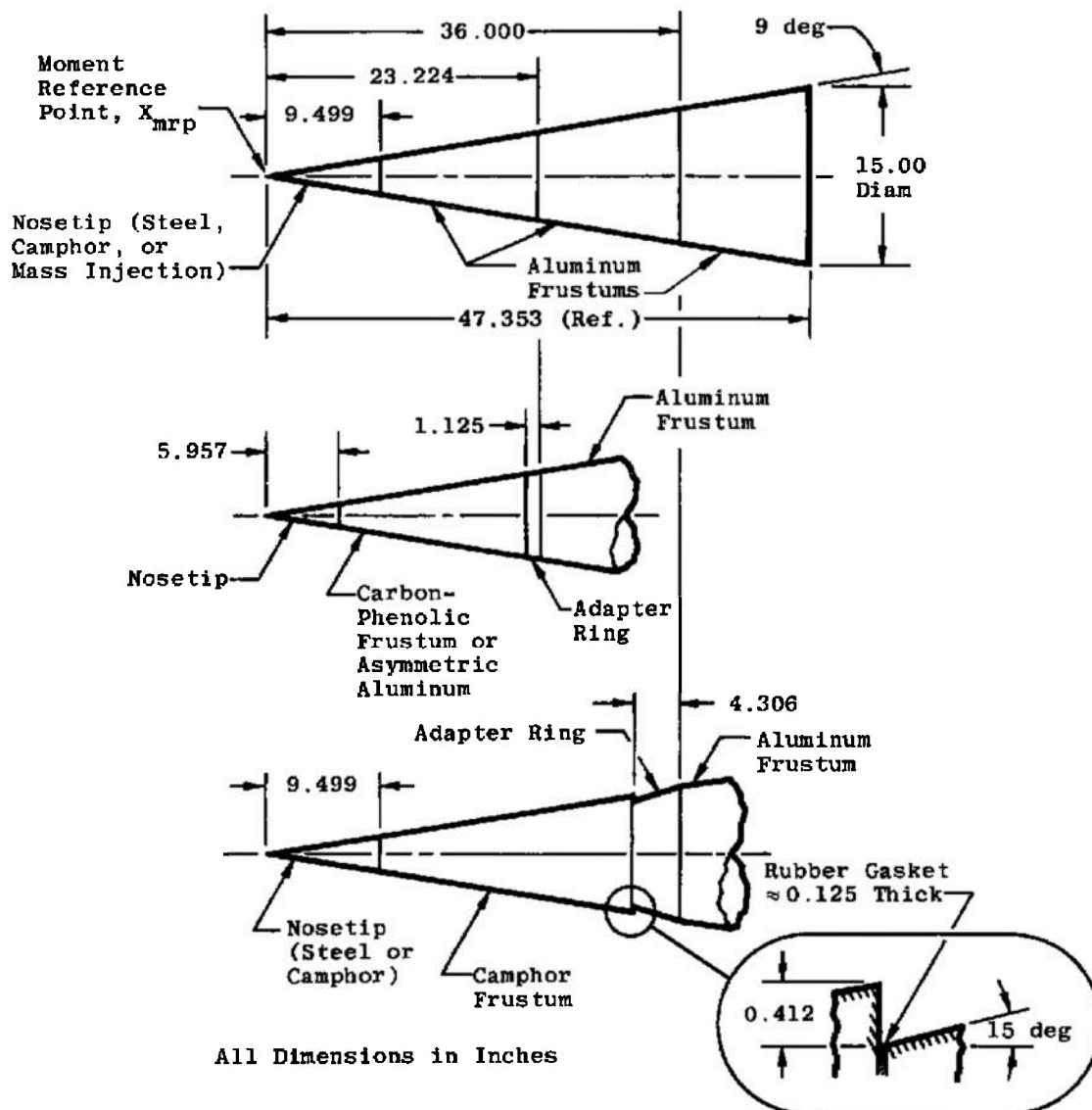
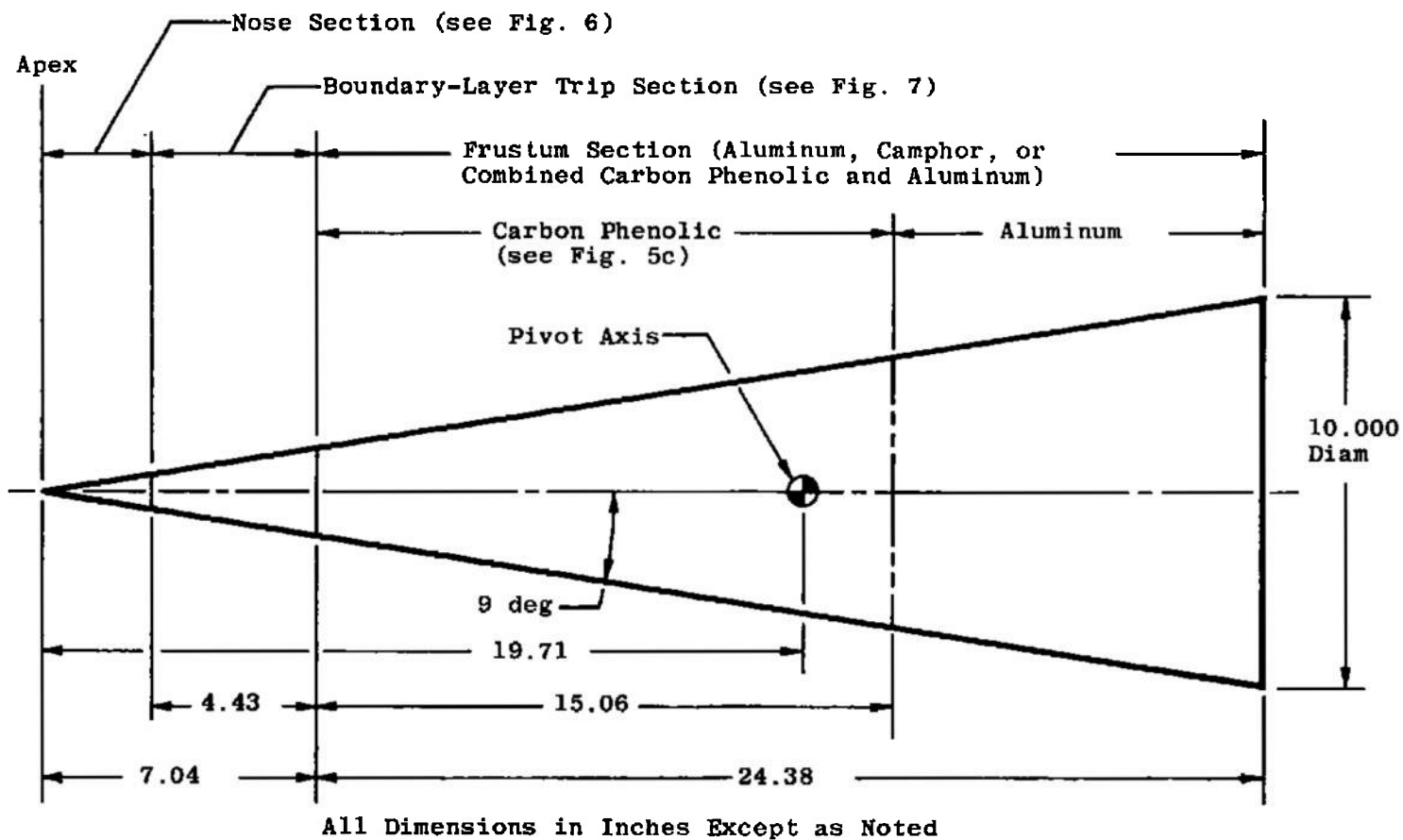


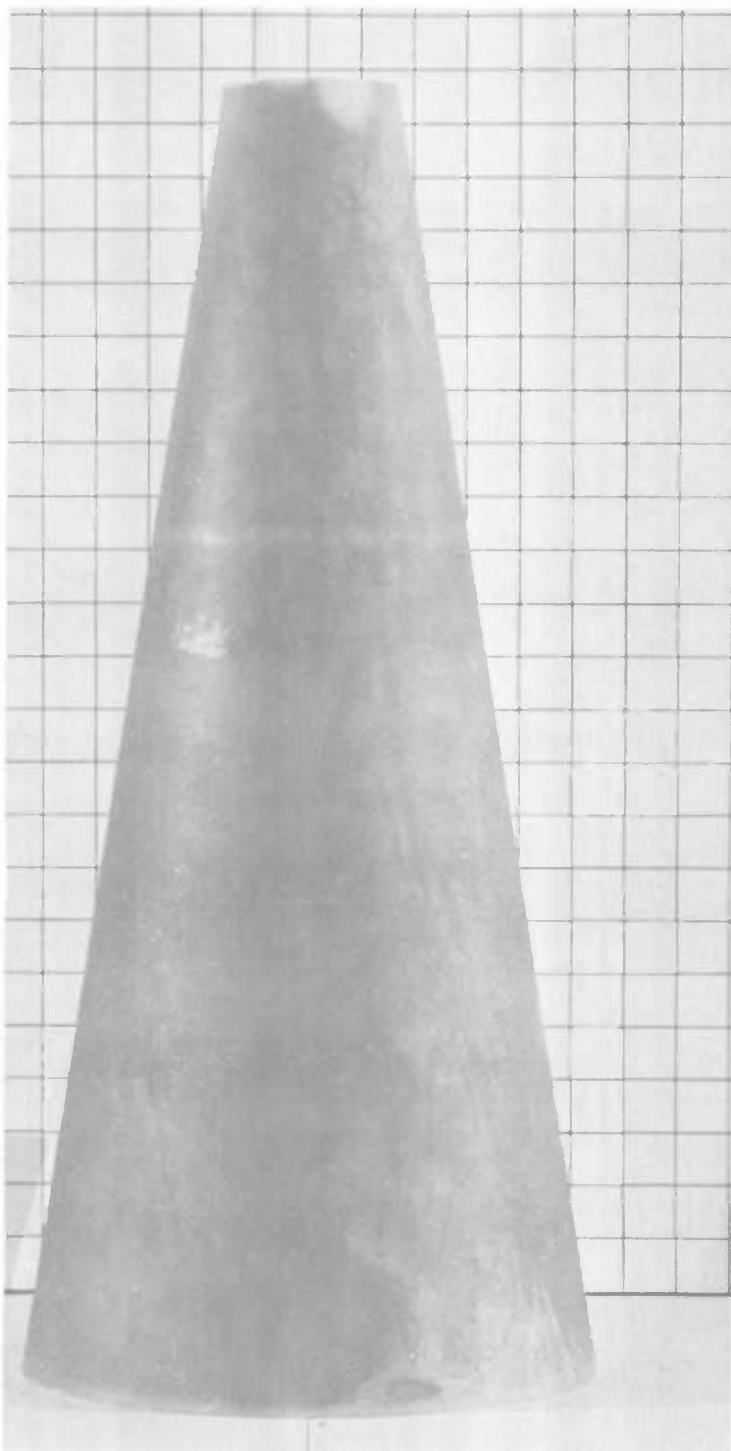
Figure 3. Photograph of model cooling manifold in Tunnel A test section tank.



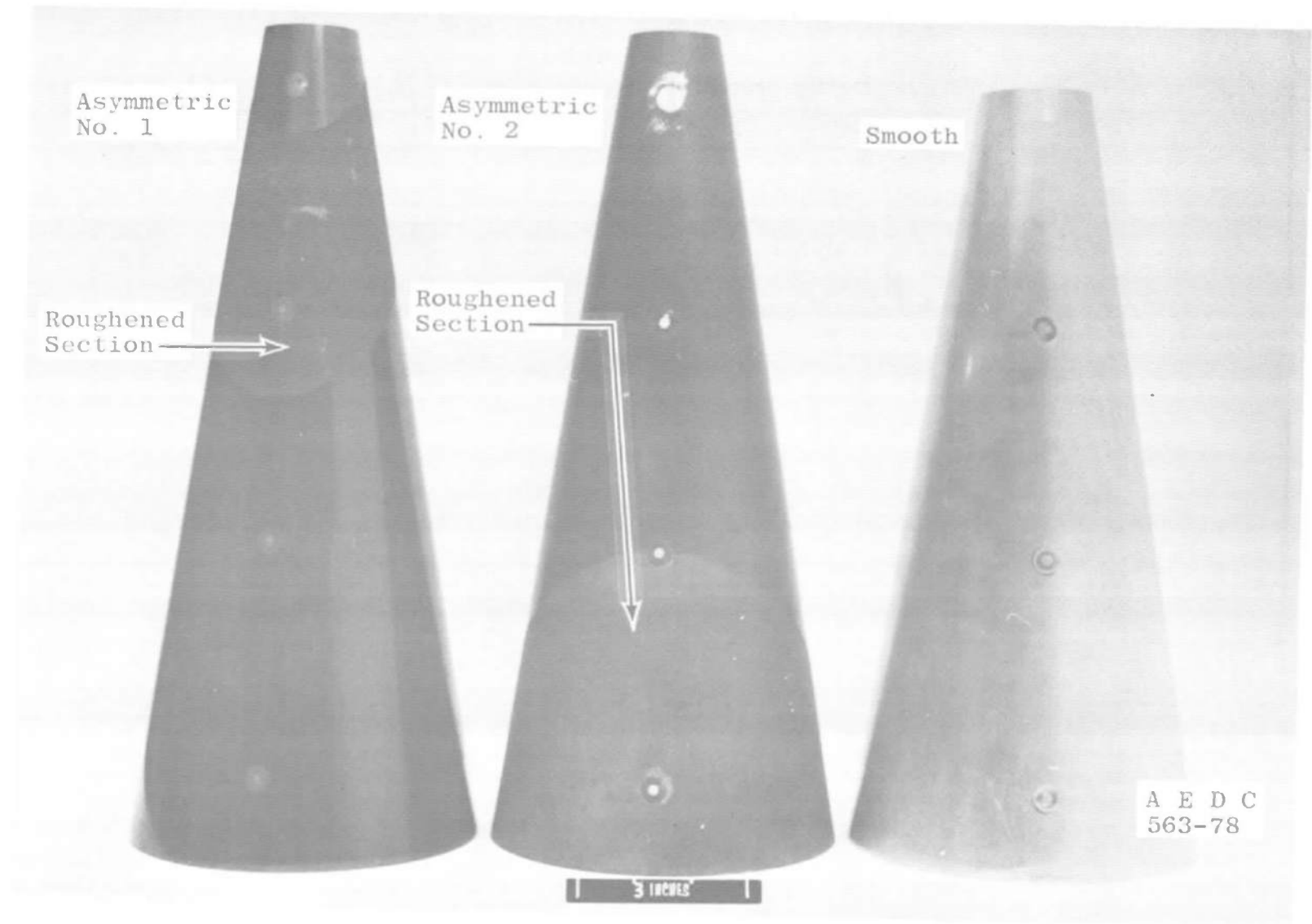
a. Spin model details
Figure 4. Model details.



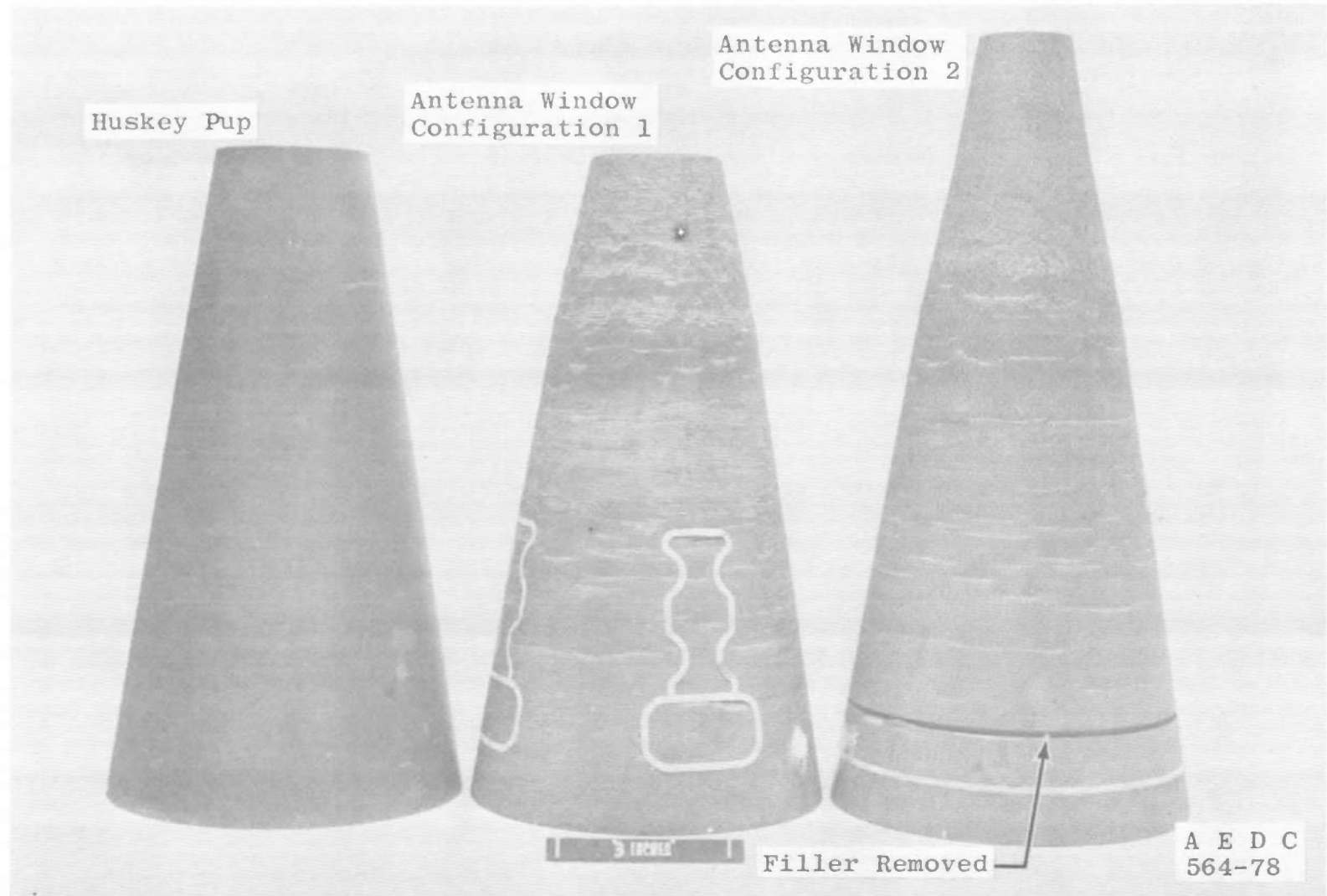
b. 3-DOF, model details
Figure 4. Concluded.



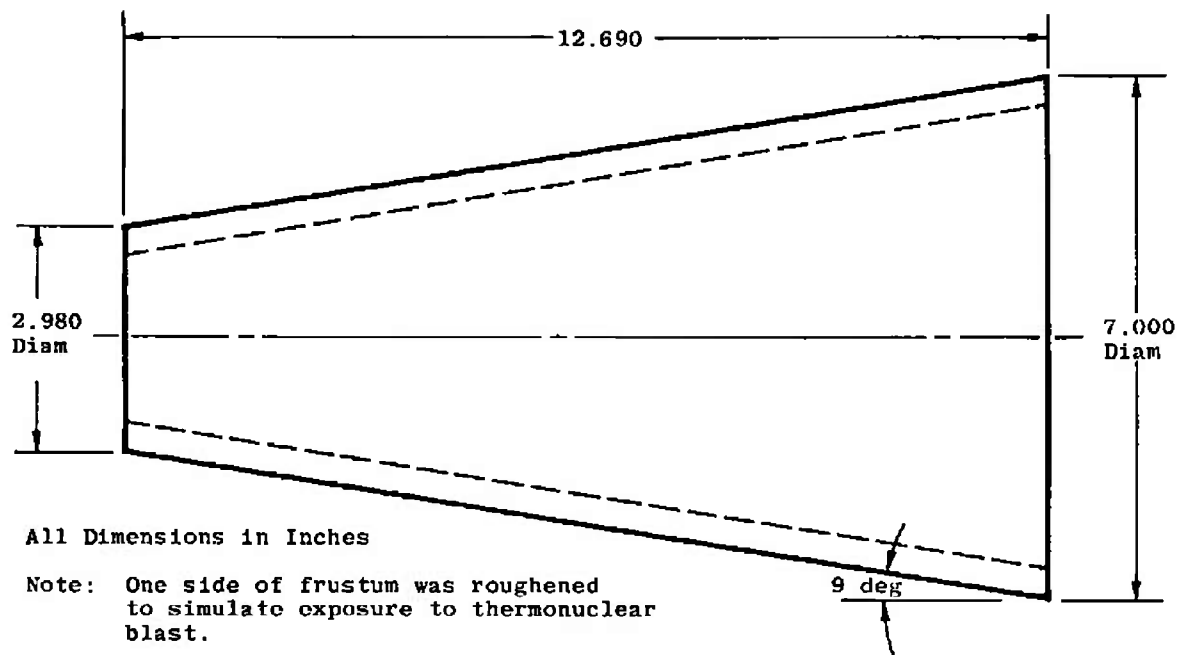
a. Photograph of camphor frustum
(typical pretest photograph)
Figure 5. Frustum details.



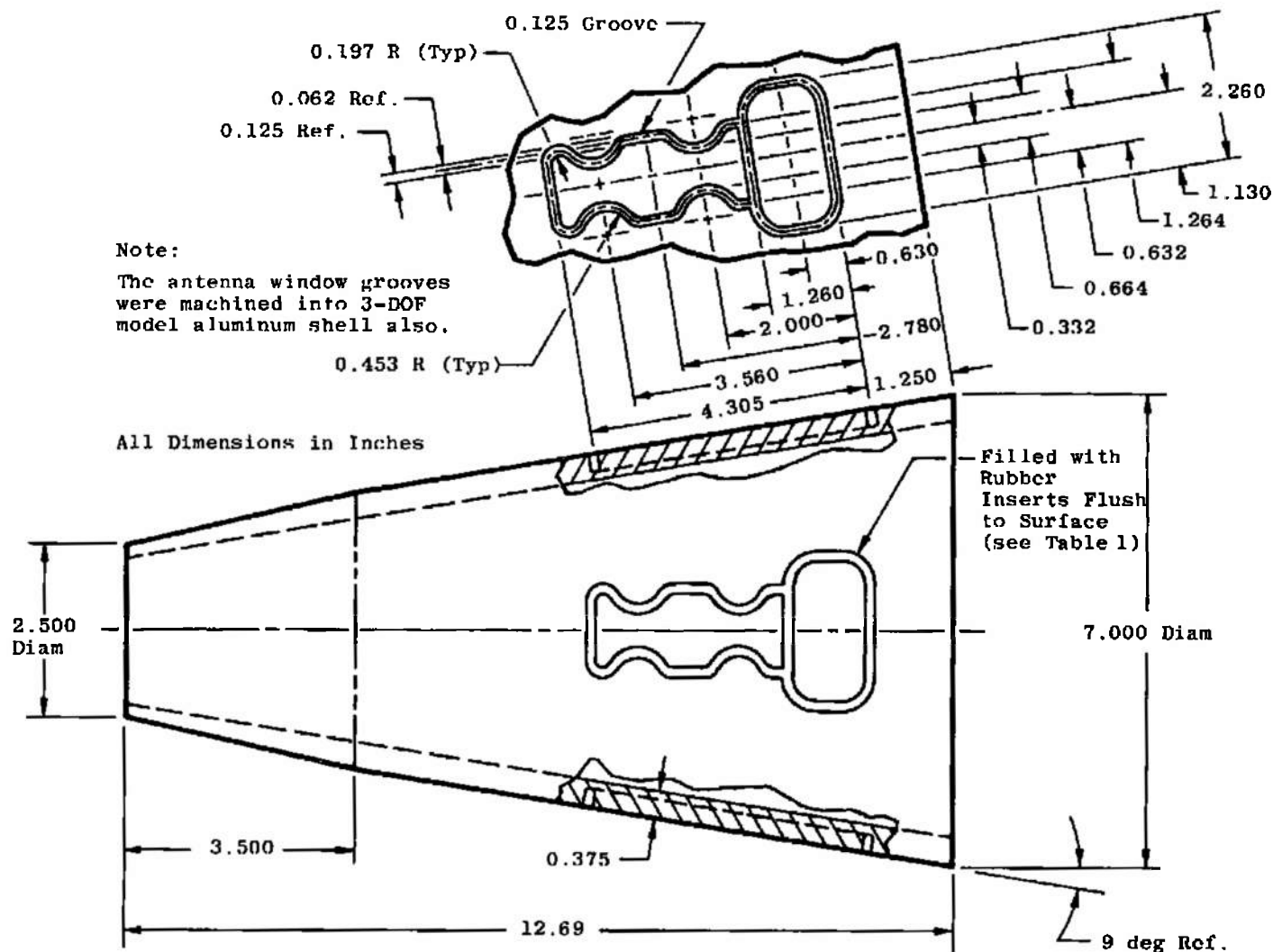
b. Photograph of asymmetric aluminum frustums
Figure 5. Continued.



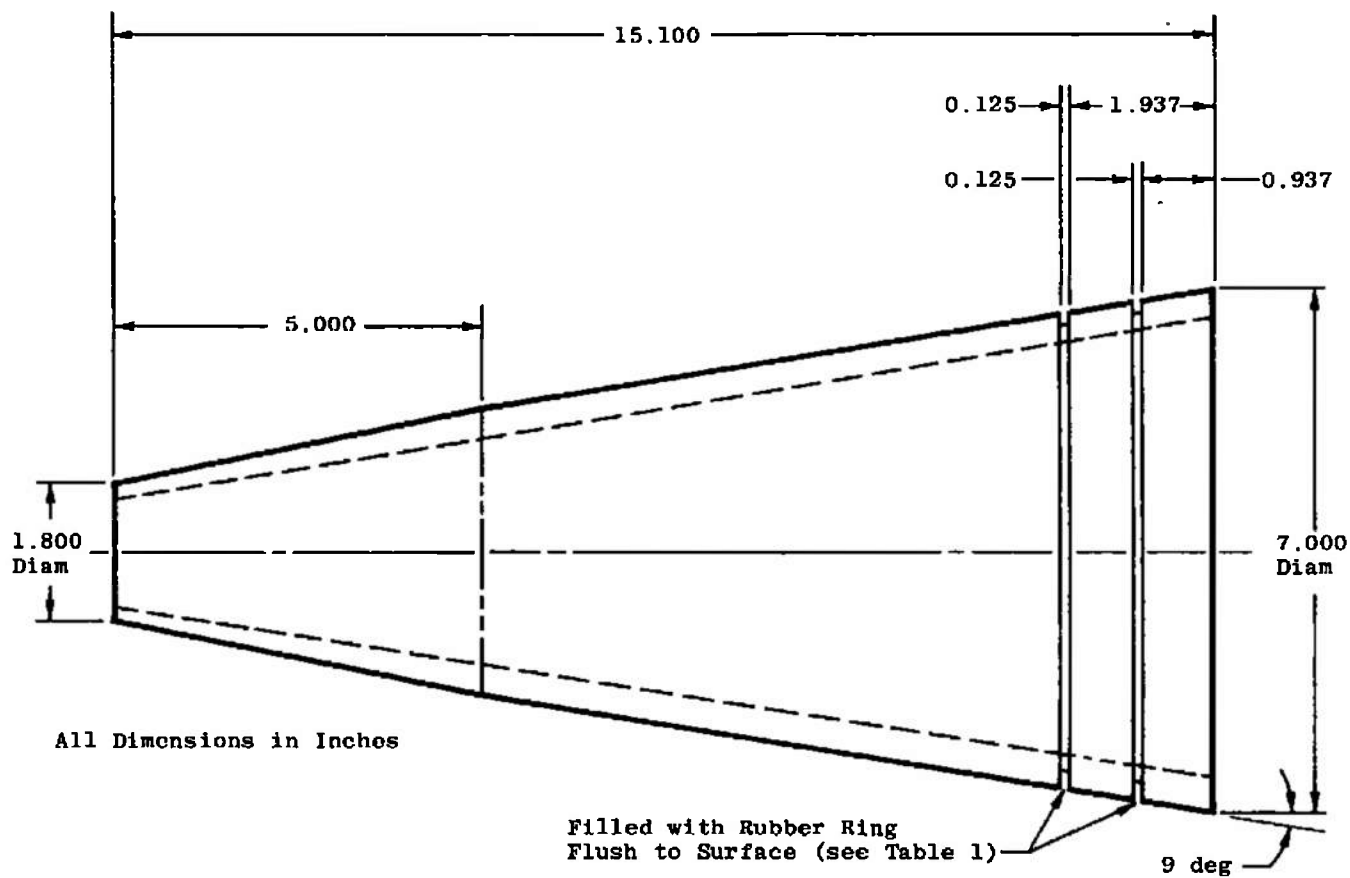
c. Photograph of carbon phenolic frustums
Figure 5. Continued.



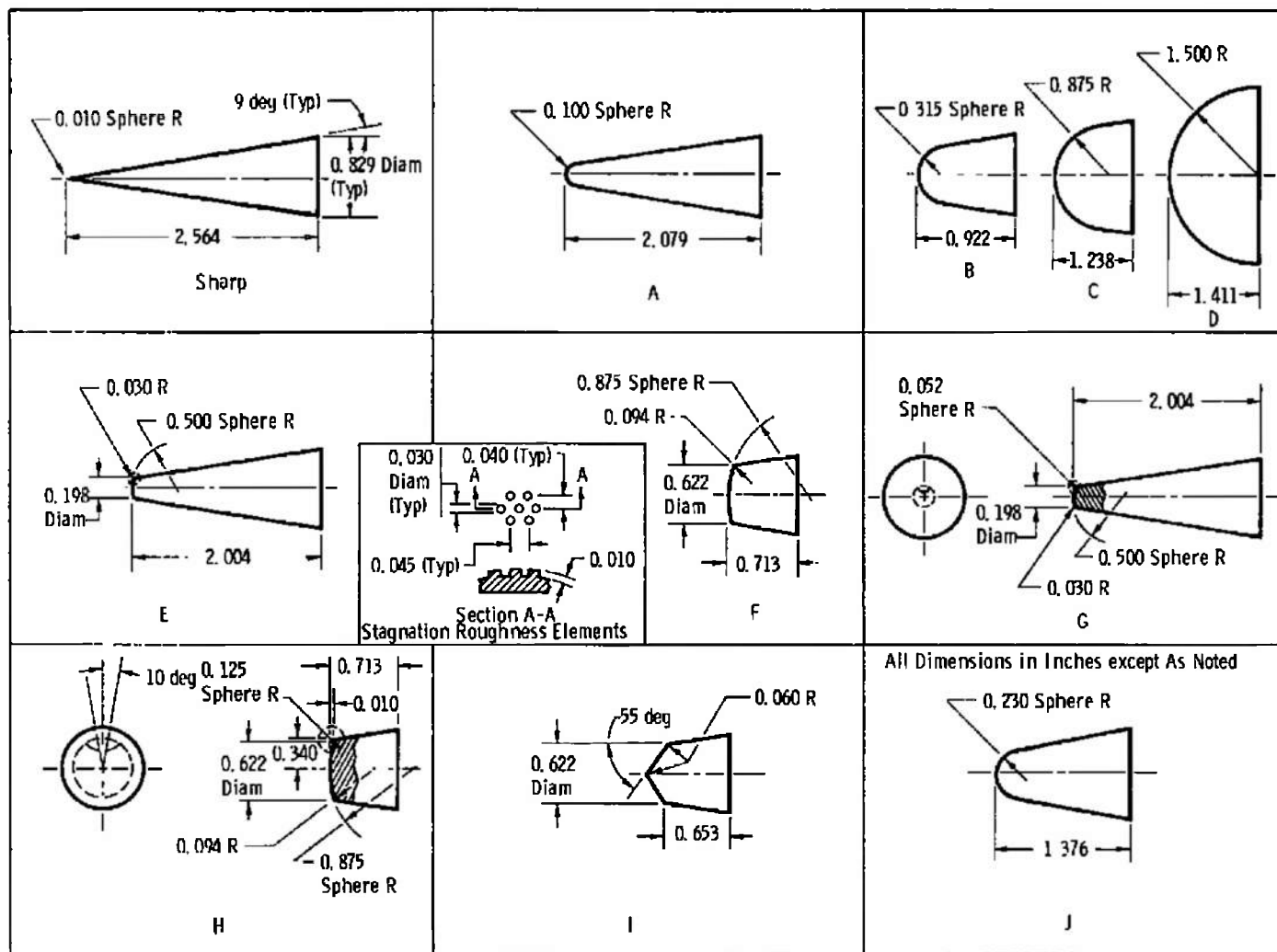
d. Huskey pup-carbon phenolic frustum
Figure 5. Continued.



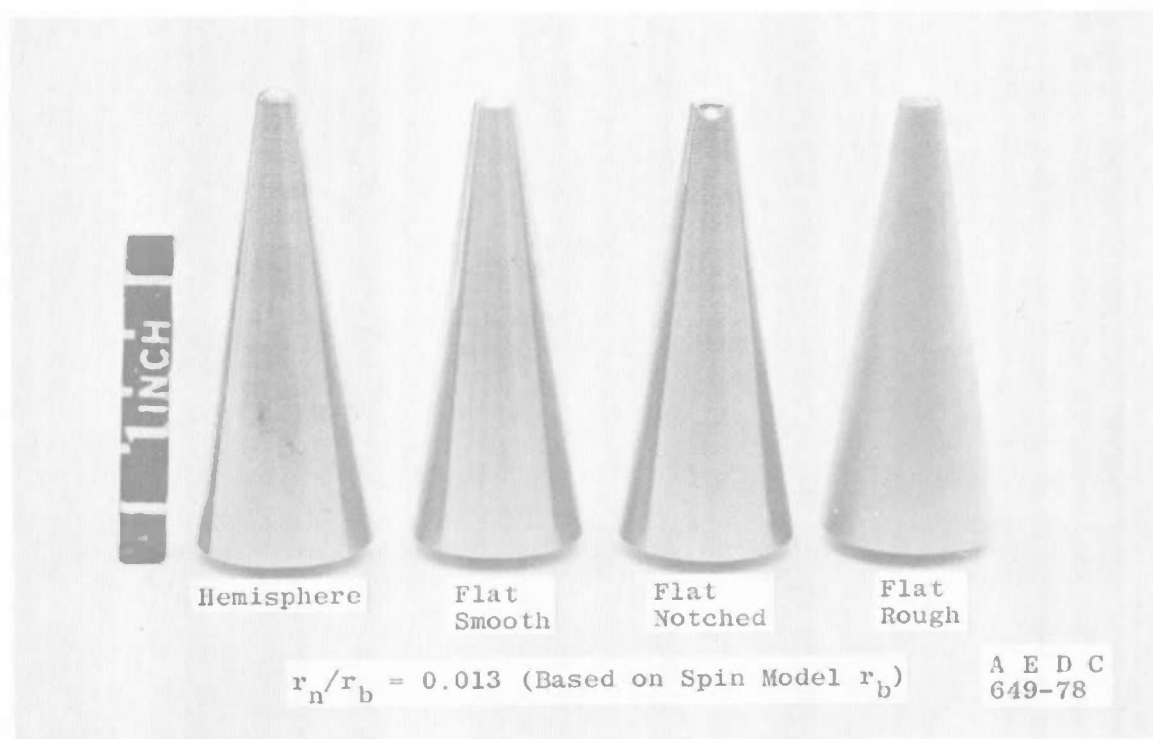
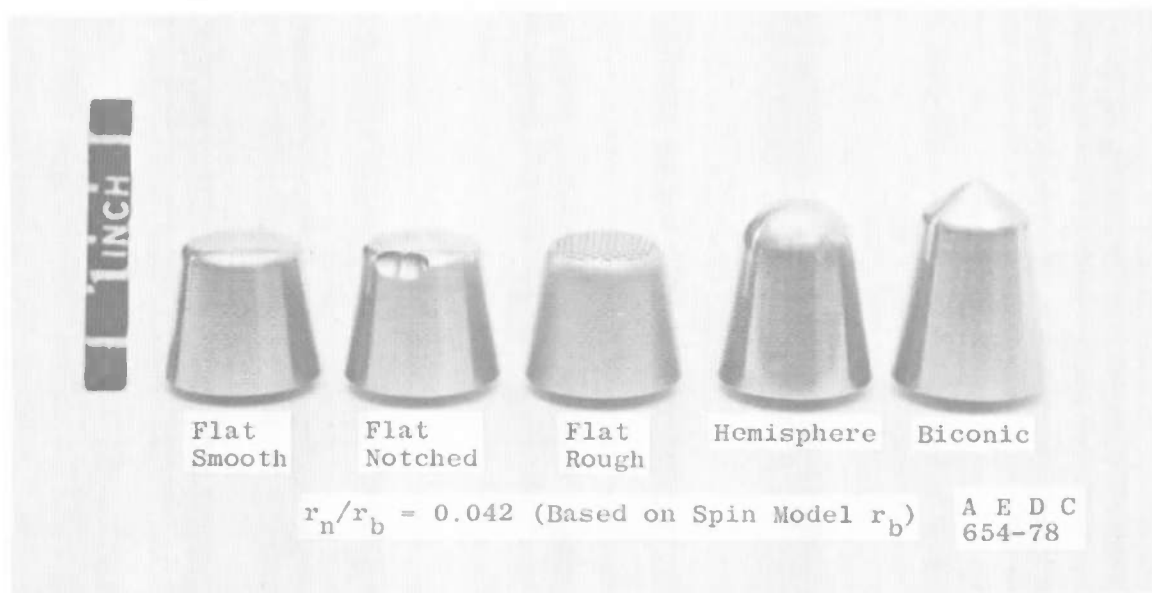
e. Antenna window, Configuration 1, carbon phenolic frustum
Figure 5. Continued.



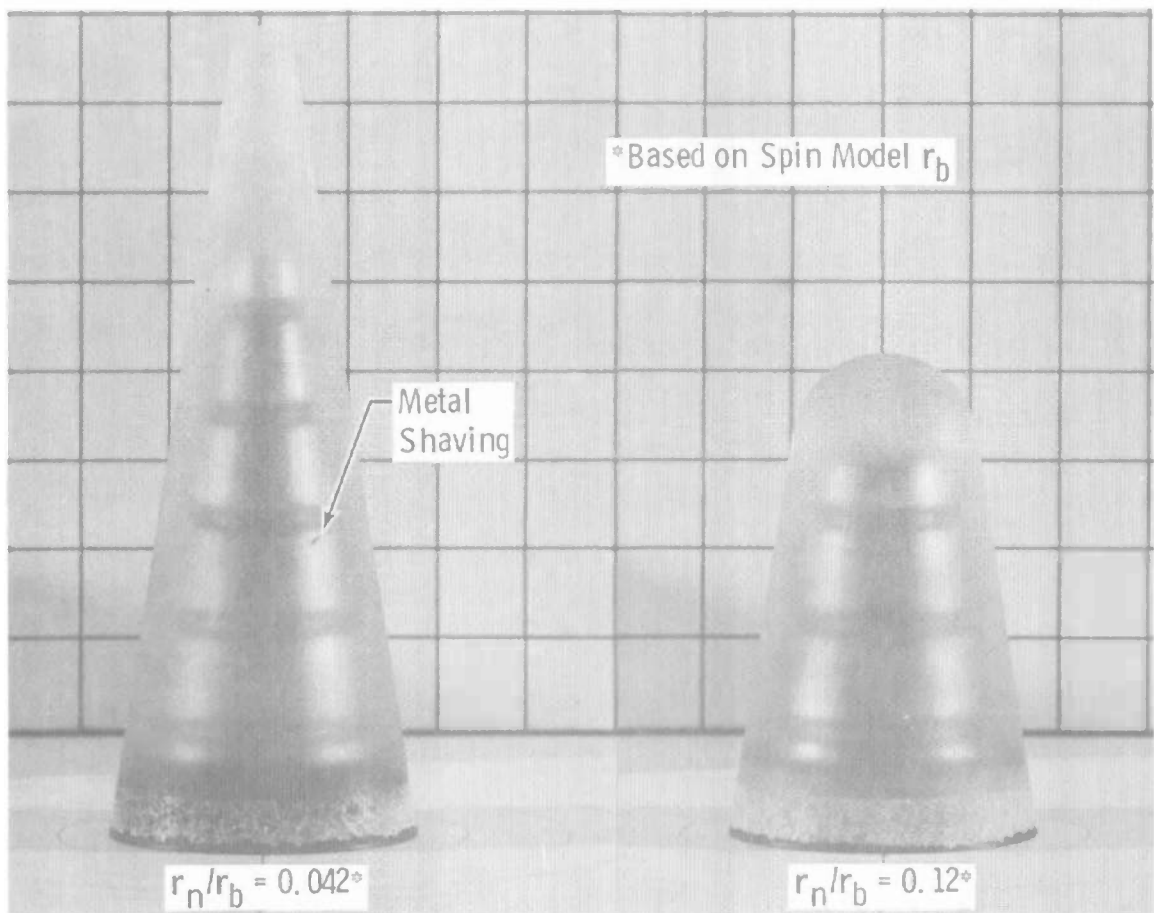
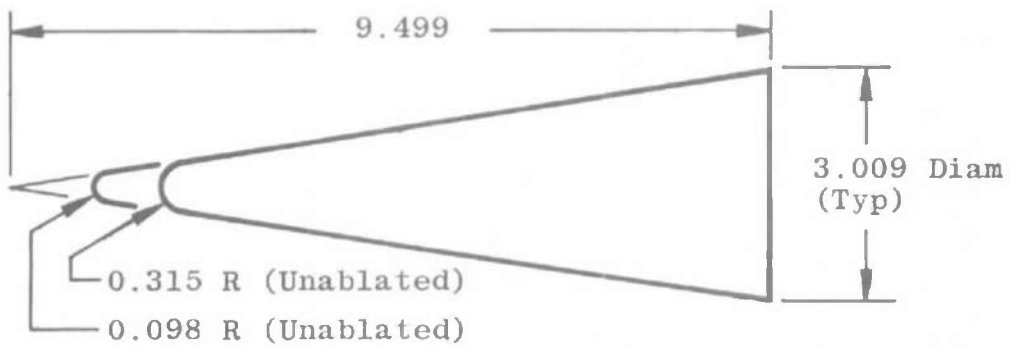
f. Antenna window, Configuration 2, carbon phenolic frustum
Figure 5. Concluded.



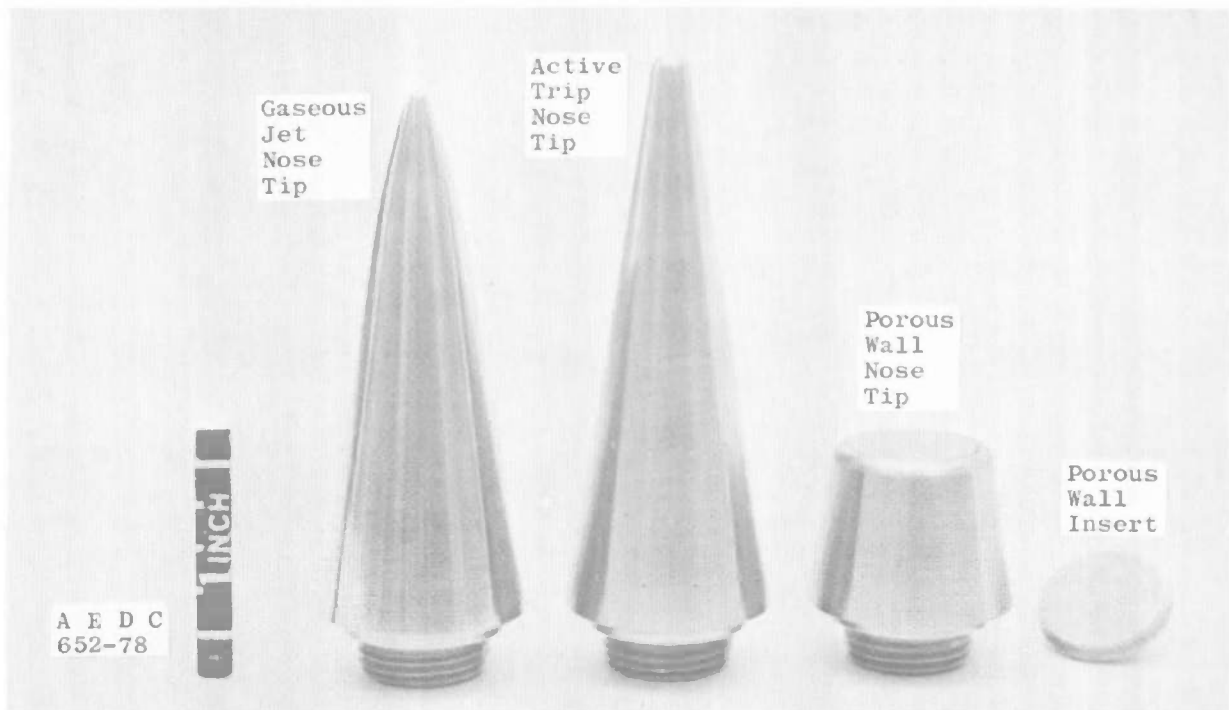
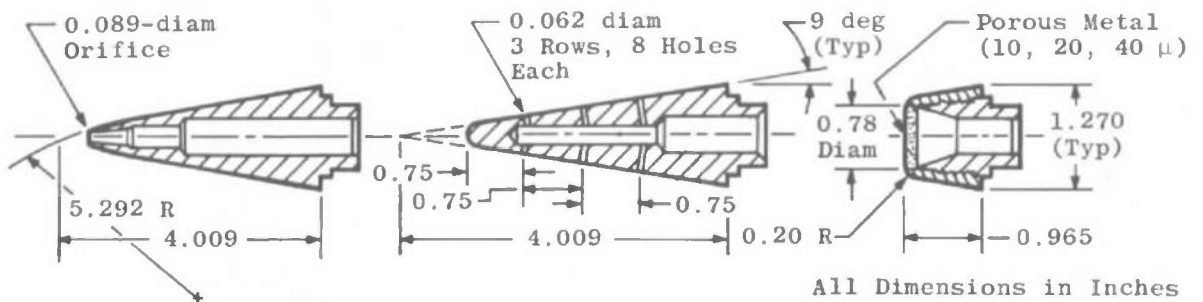
a. Nose dimensions
Figure 6. Nose tip details.



b. Steel noses
Figure 6. Continued.



c. Camphor nose tips (typ)
(pretest photograph)
Figure 6. Continued.



d. Mass injection nose tips
Figure 6. Concluded.

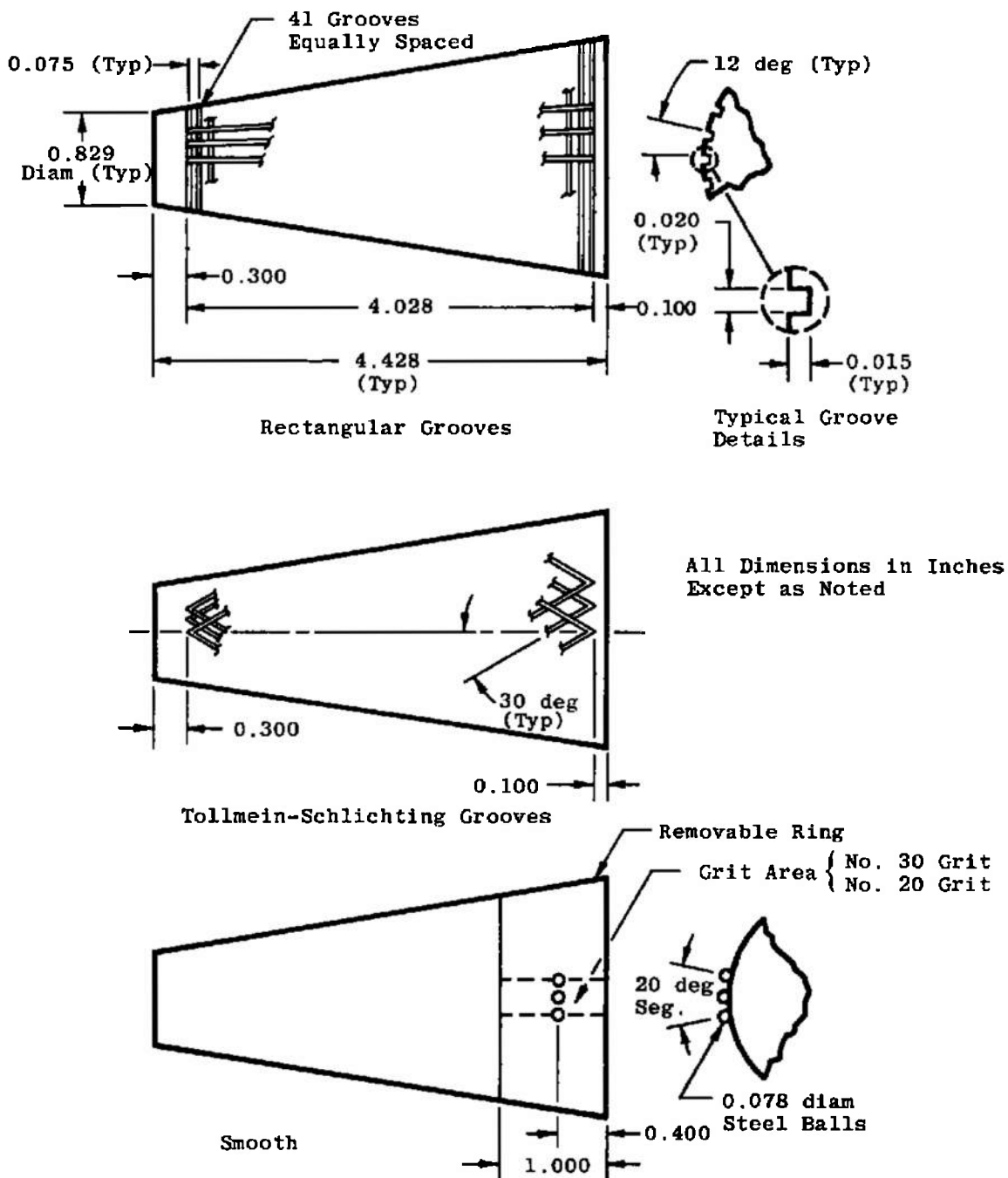


Figure 7. Boundary-layer trips.

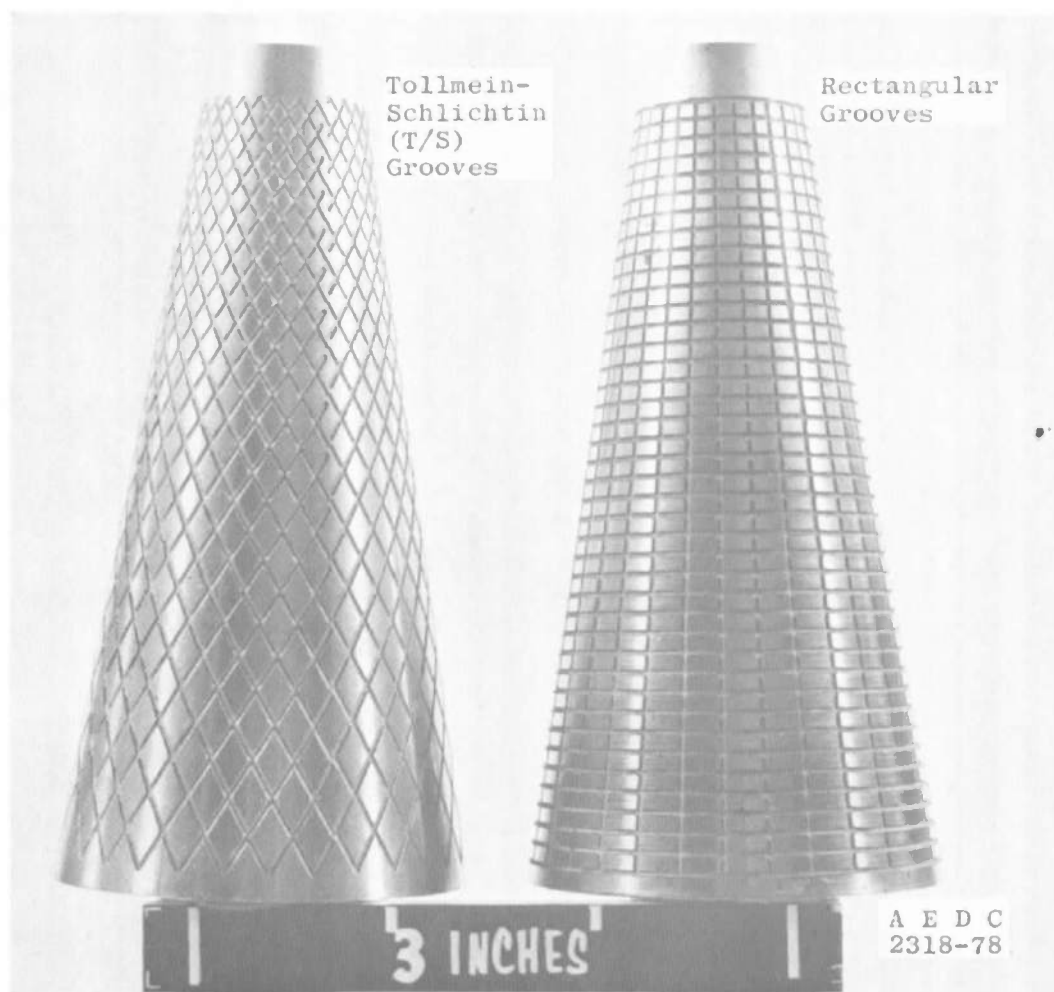


Figure 8. Groove-type trip configurations.

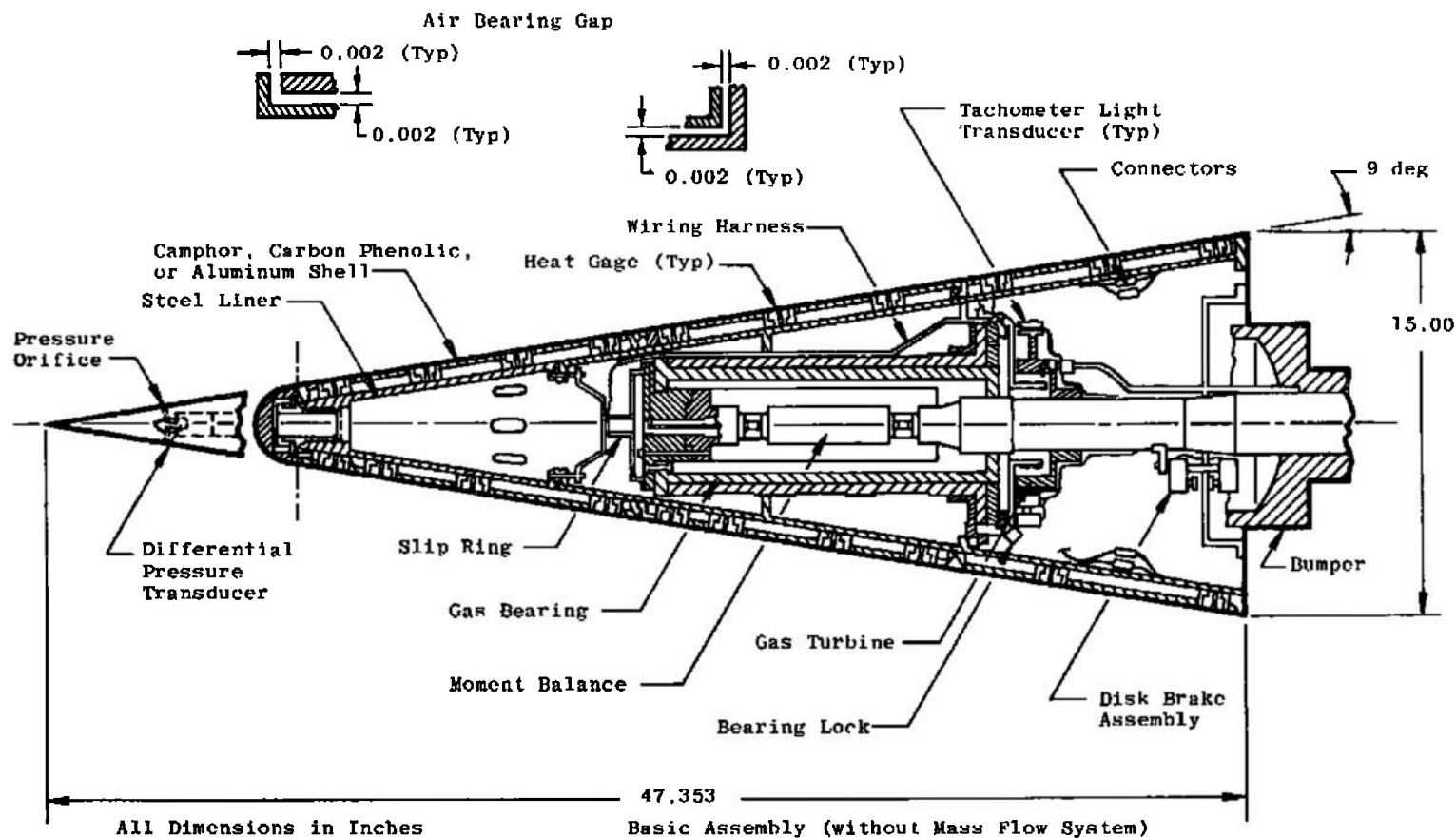
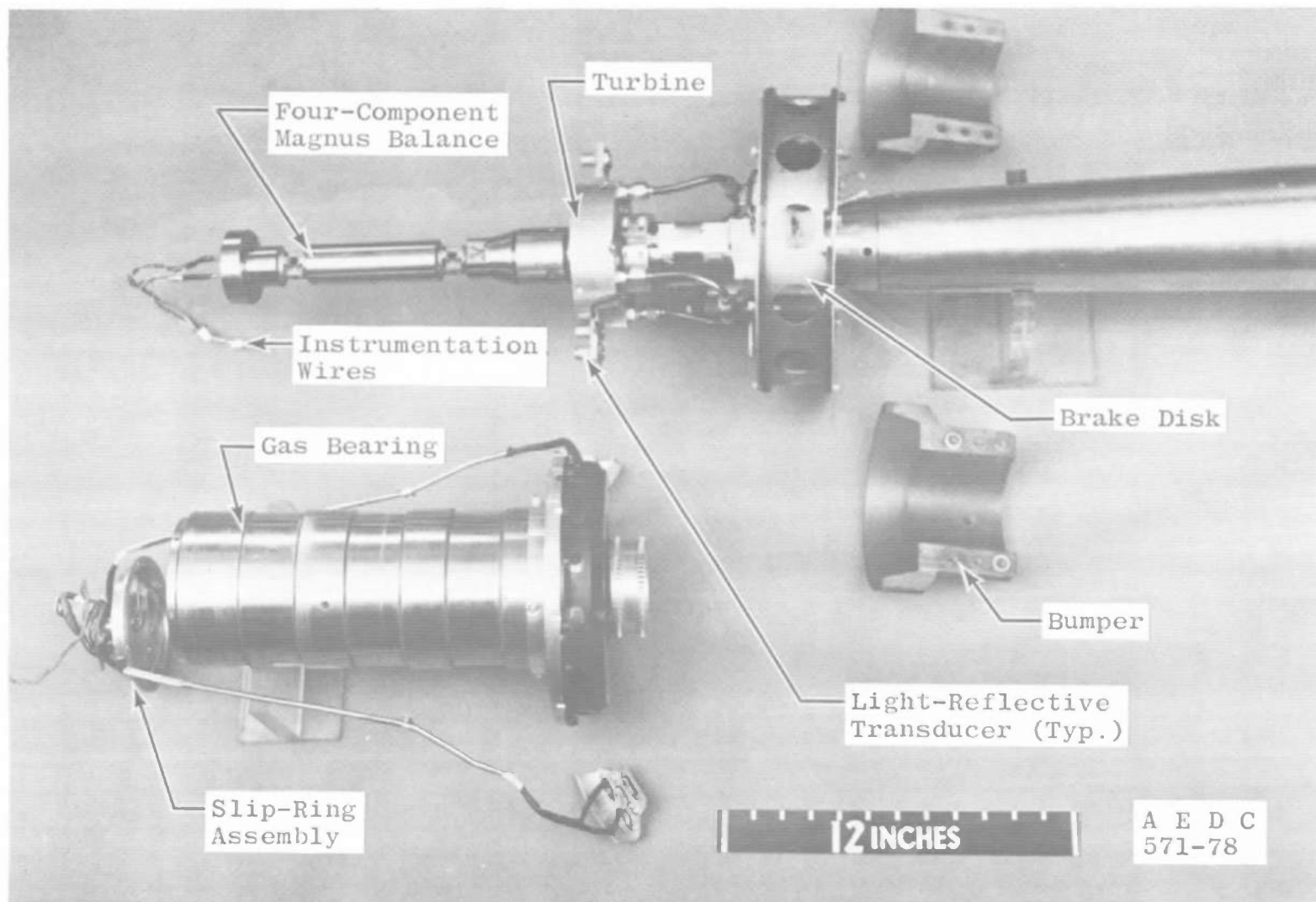
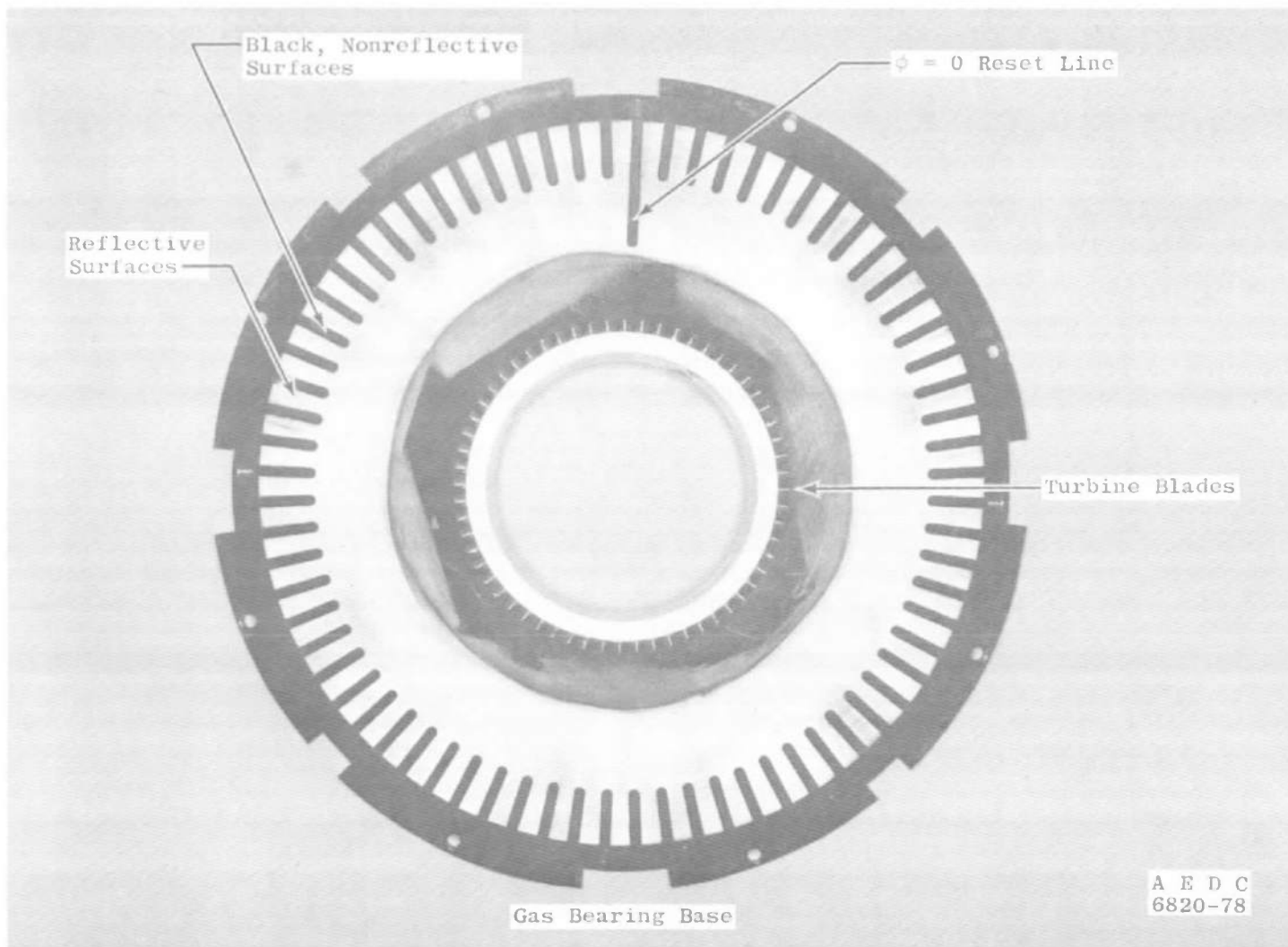


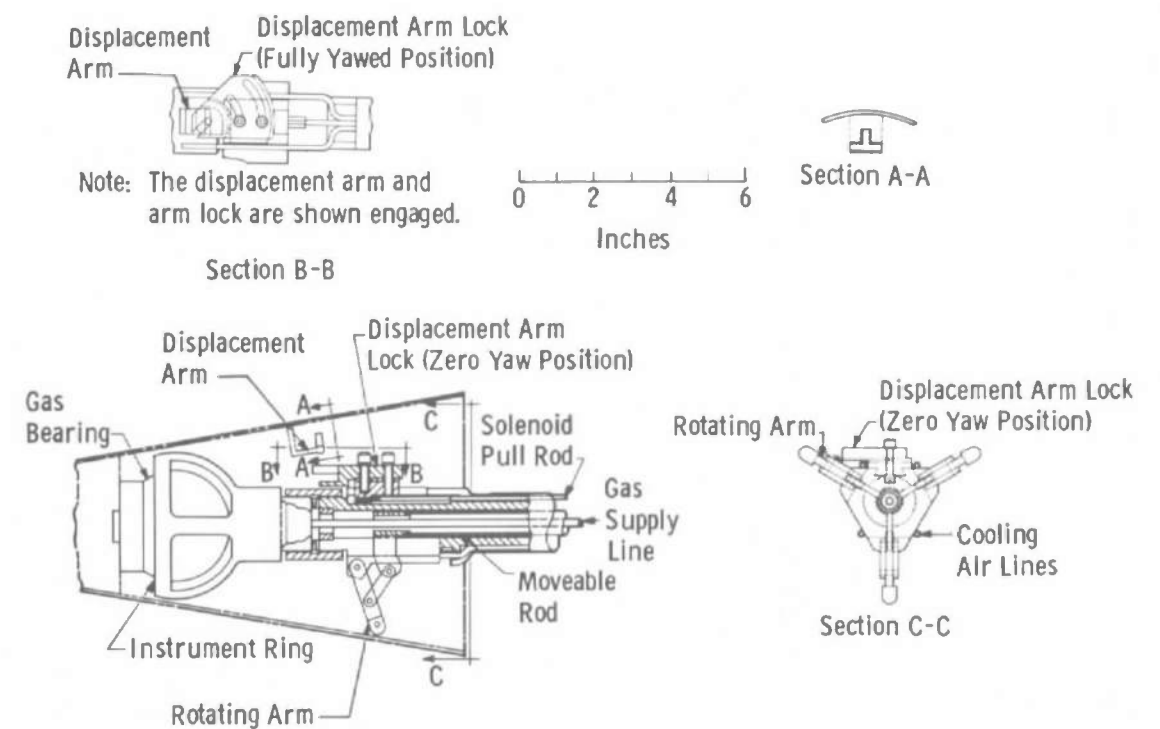
Figure 9. Details of the spin test mechanism.



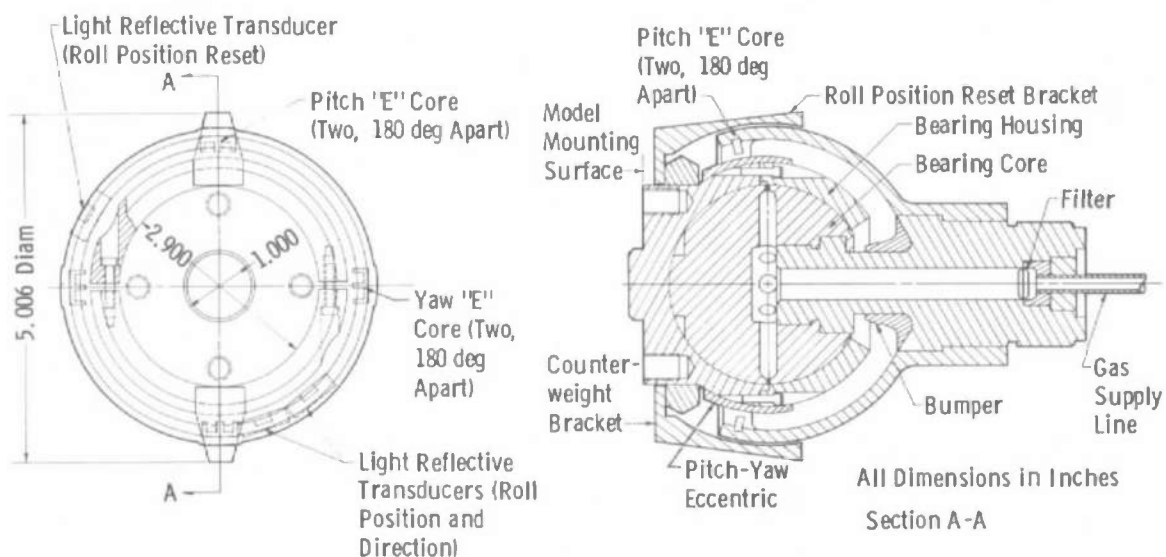
a. Major subsystems
 Figure 10. Photographs of spin test mechanism.



b. Gas turbine drum
Figure 10. Concluded.



a. Balance assembly



b. Balance details

Figure 11. 3-DOF test mechanism (VKF-3.A).

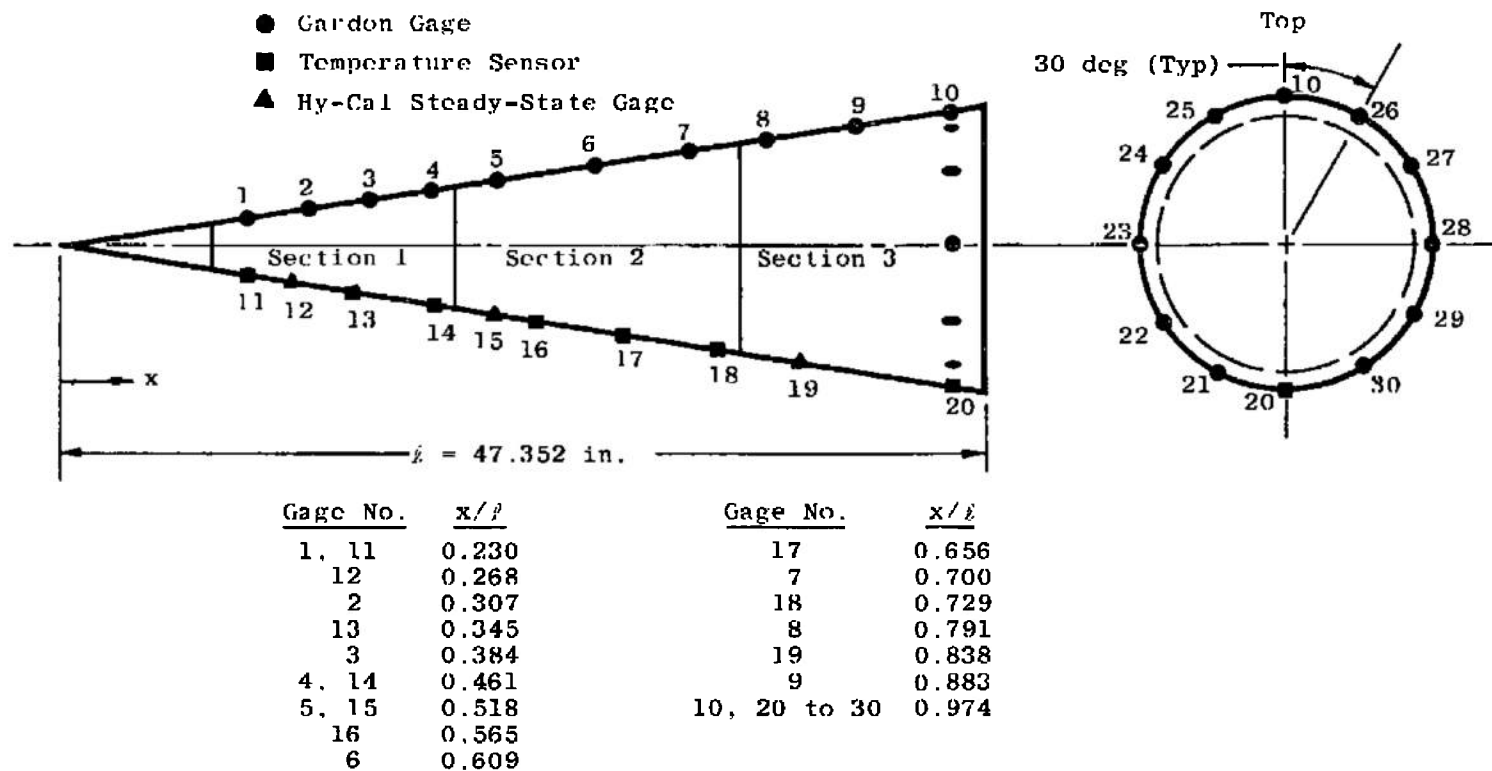
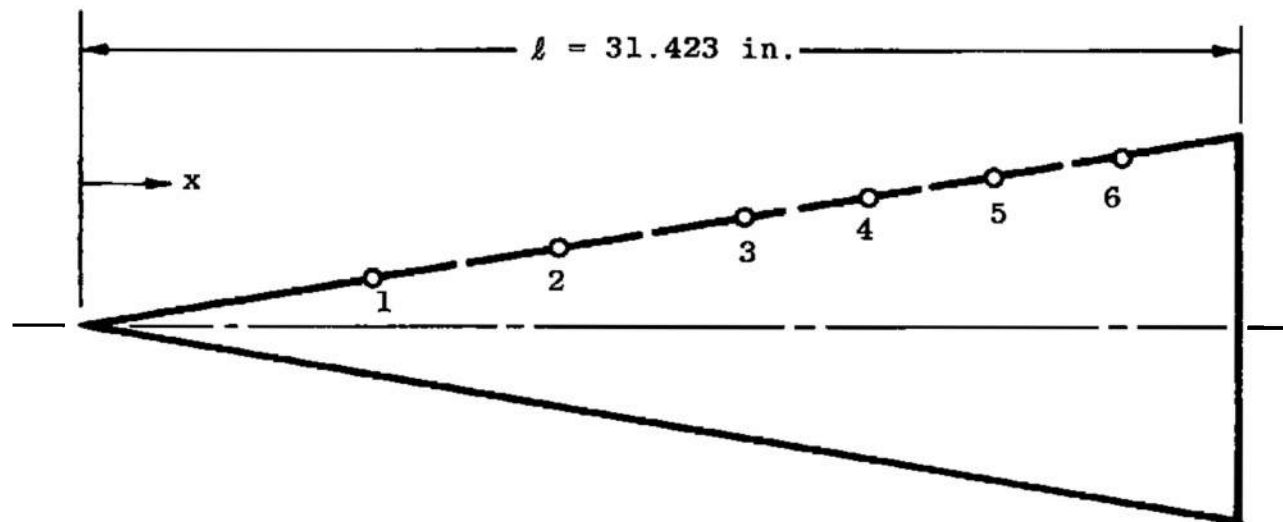
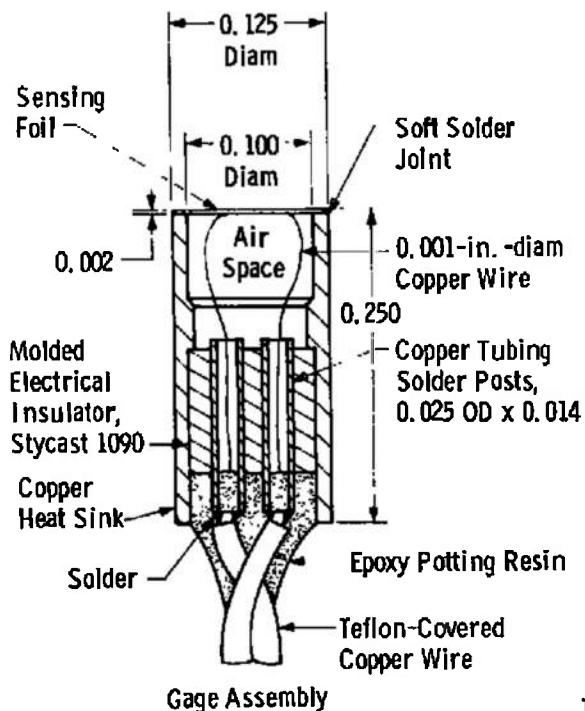


Figure 12. Instrumentation locations on spin model.



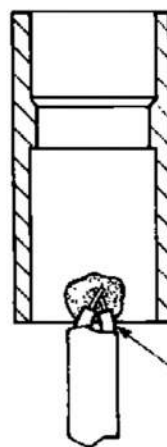
Gage No.	x/l	Gages were either Gardon or Hy-Therm depending on shell.
1	0.277	
2	0.434	
3	0.591	
4	0.696	
5	0.801	
6	0.906	

Figure 13. Instrumentation locations on 3-DOF model.

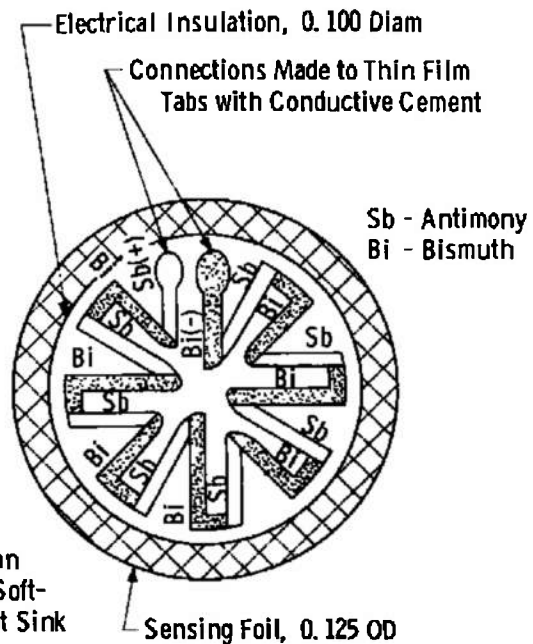


THERMOPILE GARDON GAGE

All Dimensions in Inches

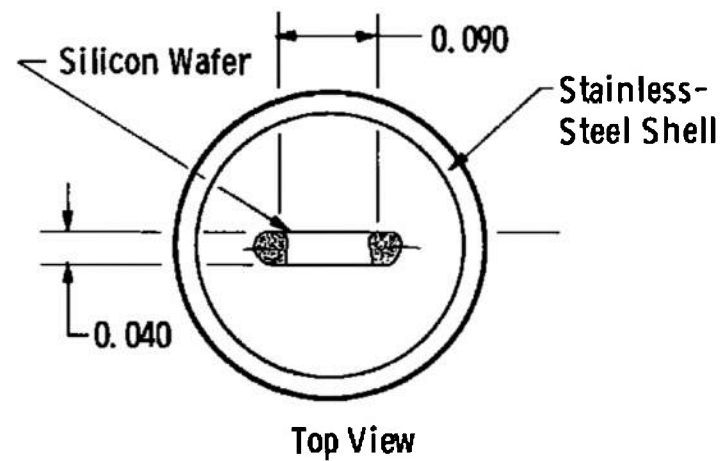
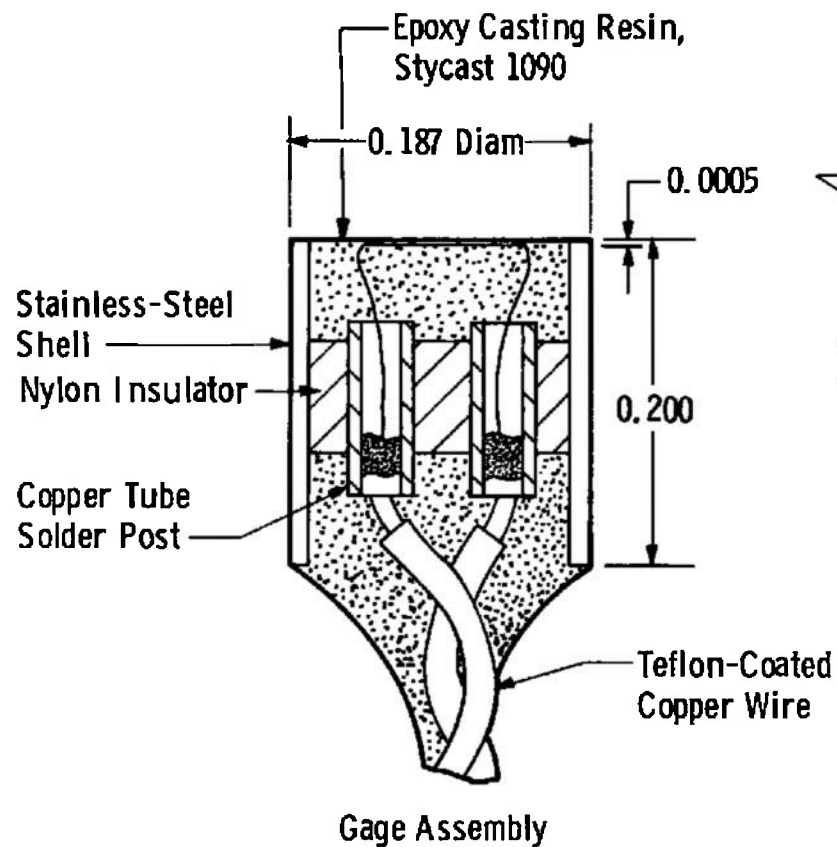


Thermocouple Attachment



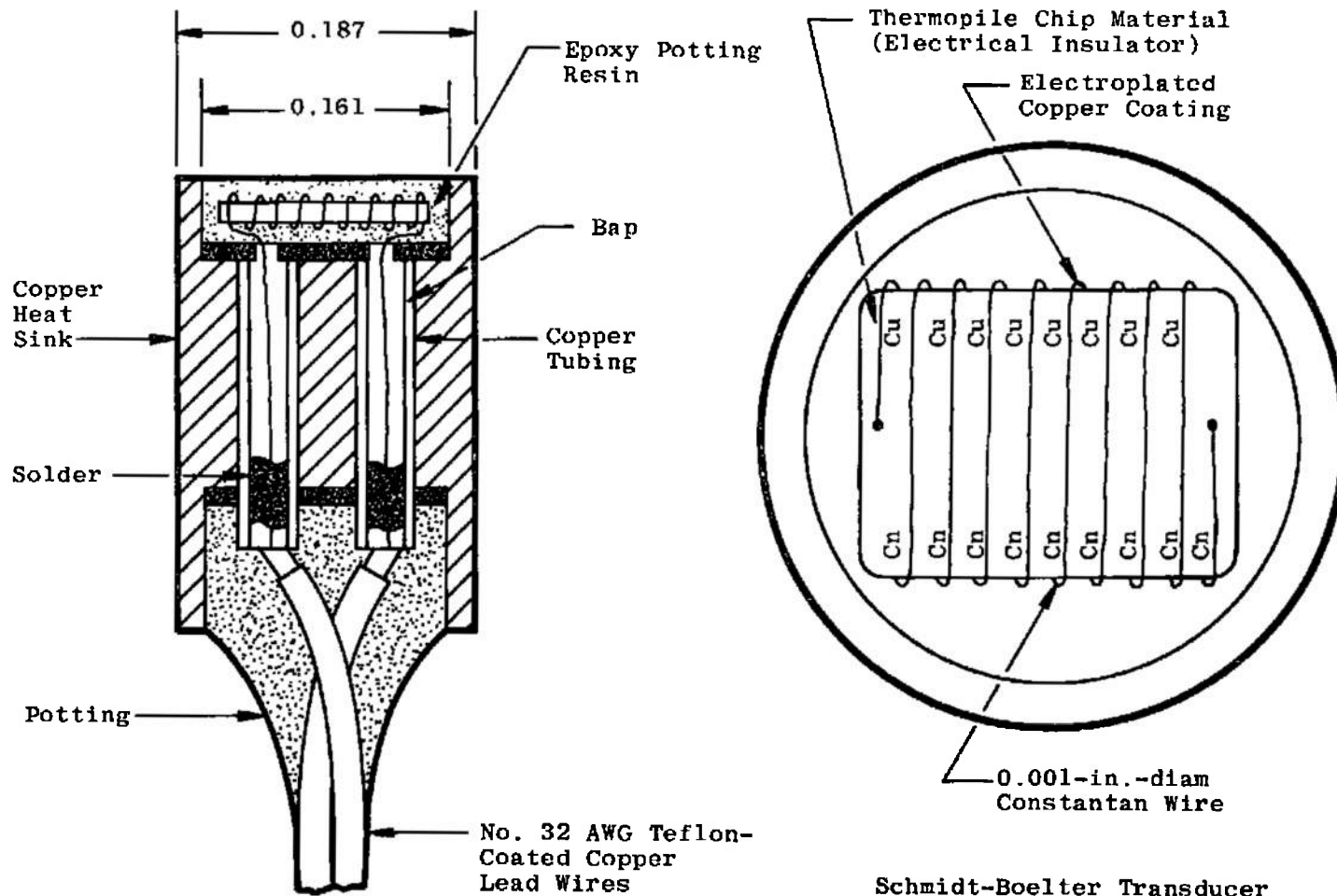
Back View of Sensing Foil

a. Thermopile Gardon gage
Figure 14. Details of heat gages.



All Dimensions in Inches

b. Temp-Sensor gage
Figure 14. Continued.



All Dimensions in Inches

Transducer Assembly Half-Section

Top View of Thermopile Chip

c. Schmidt-Boelter transducer
(typical of Hy-Therm)
Figure 14. Concluded.

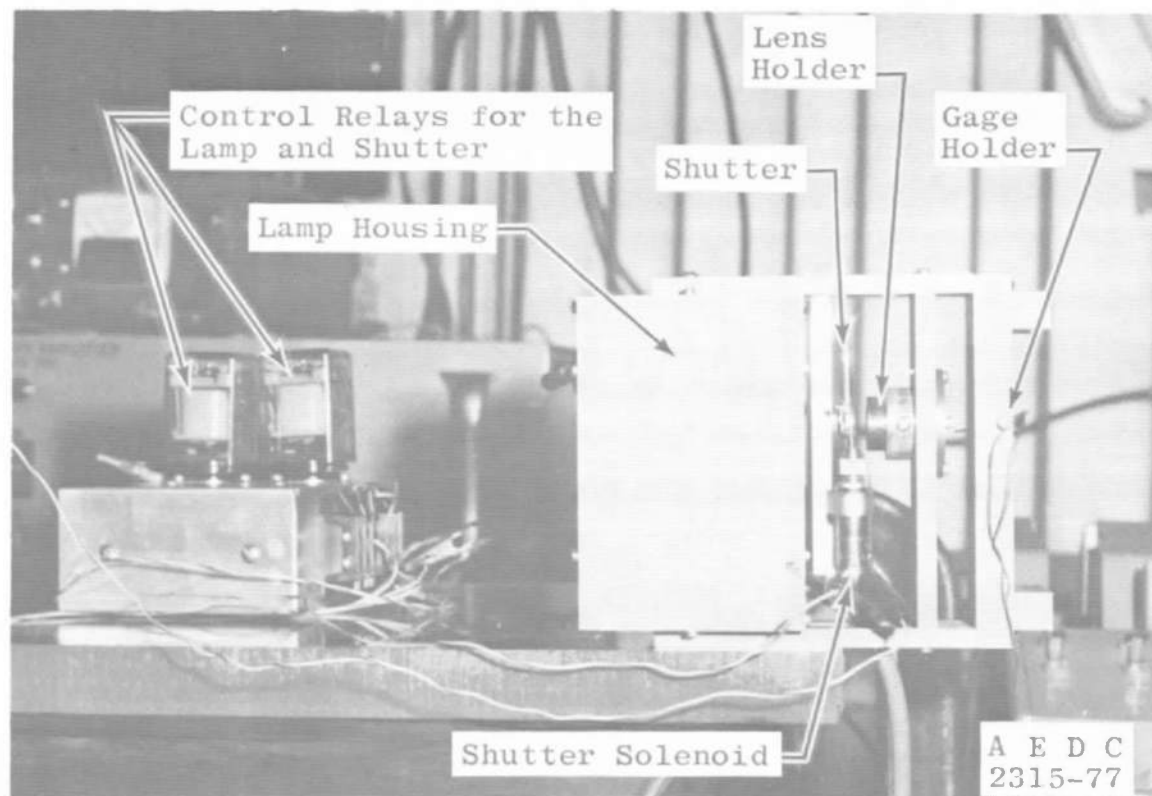


Figure 15. Thermal pulse generator photograph.

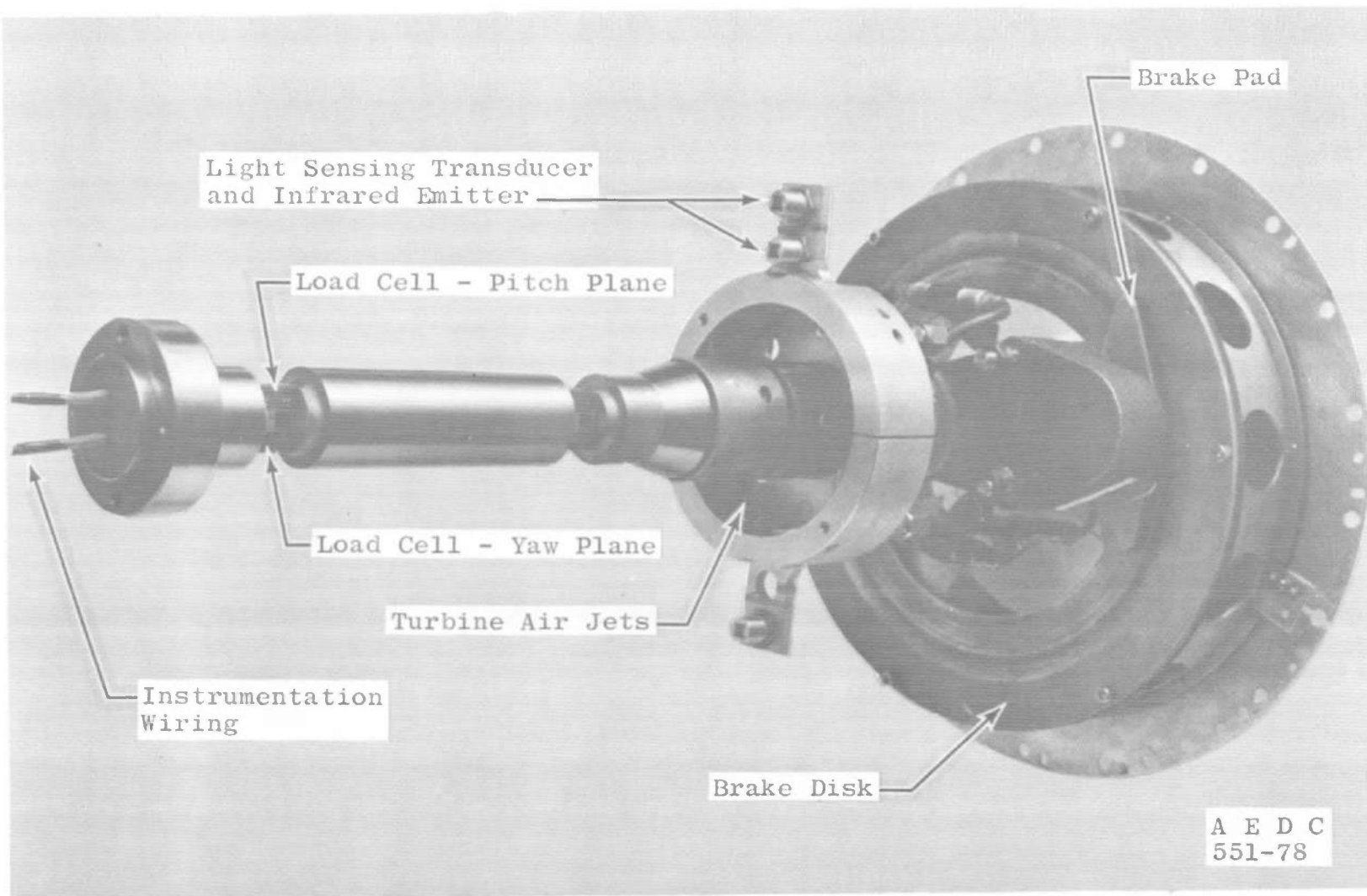
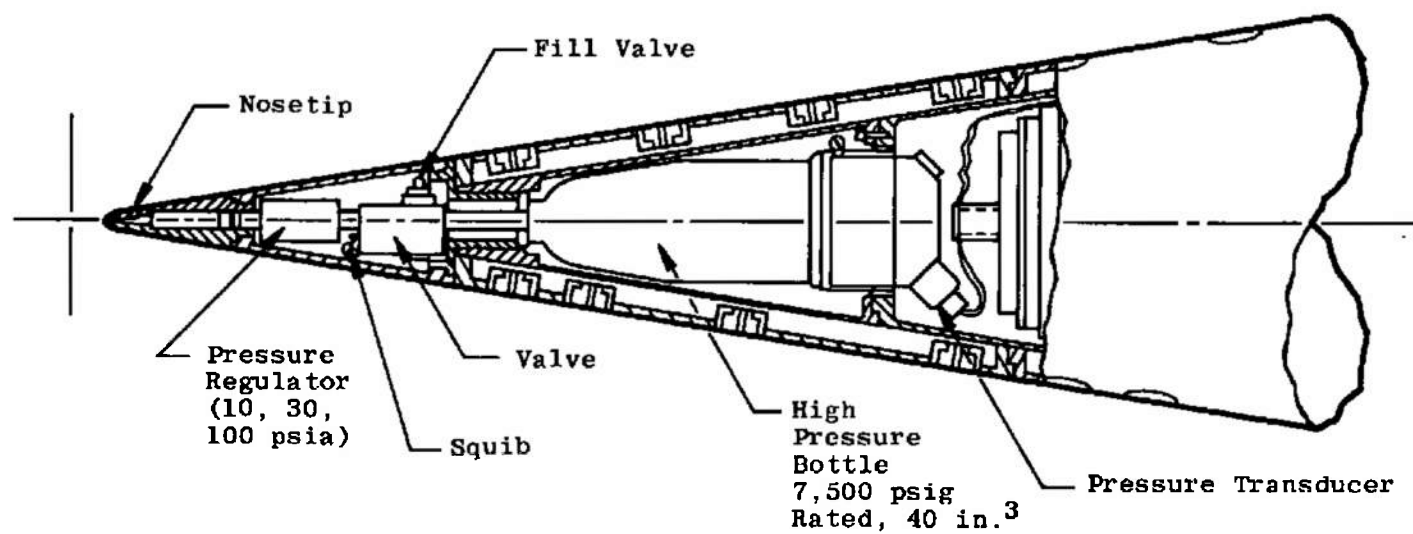
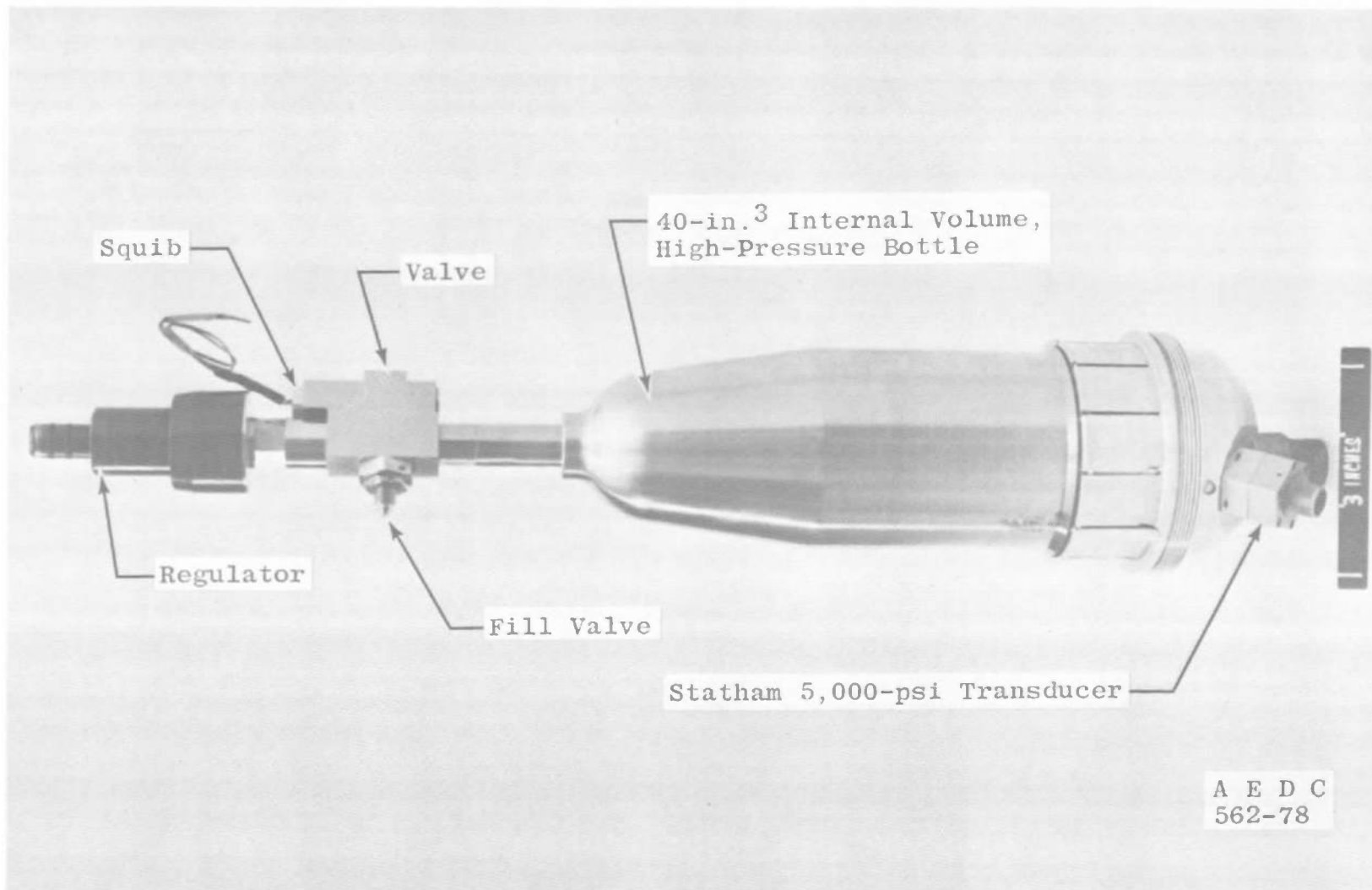


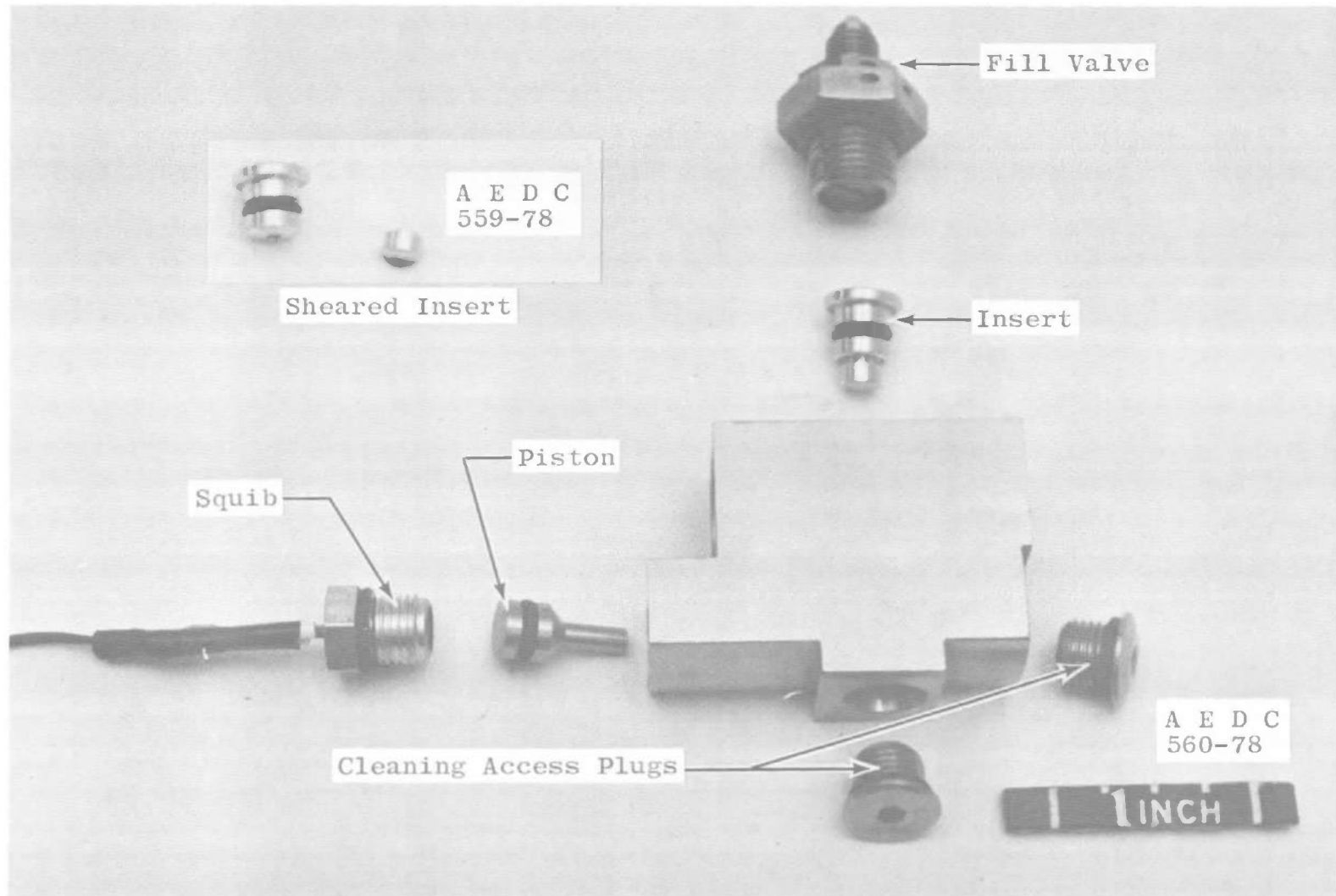
Figure 16. Four-component magnus balance 4.00-Y-34-076.



a. Schematic of mass injection system
Figure 17. Mass (N_2) injection system.



b. Photograph of mass (N₂) injection system
Figure 17. Continued.



c. Photograph of valve components
Figure 17. Concluded.

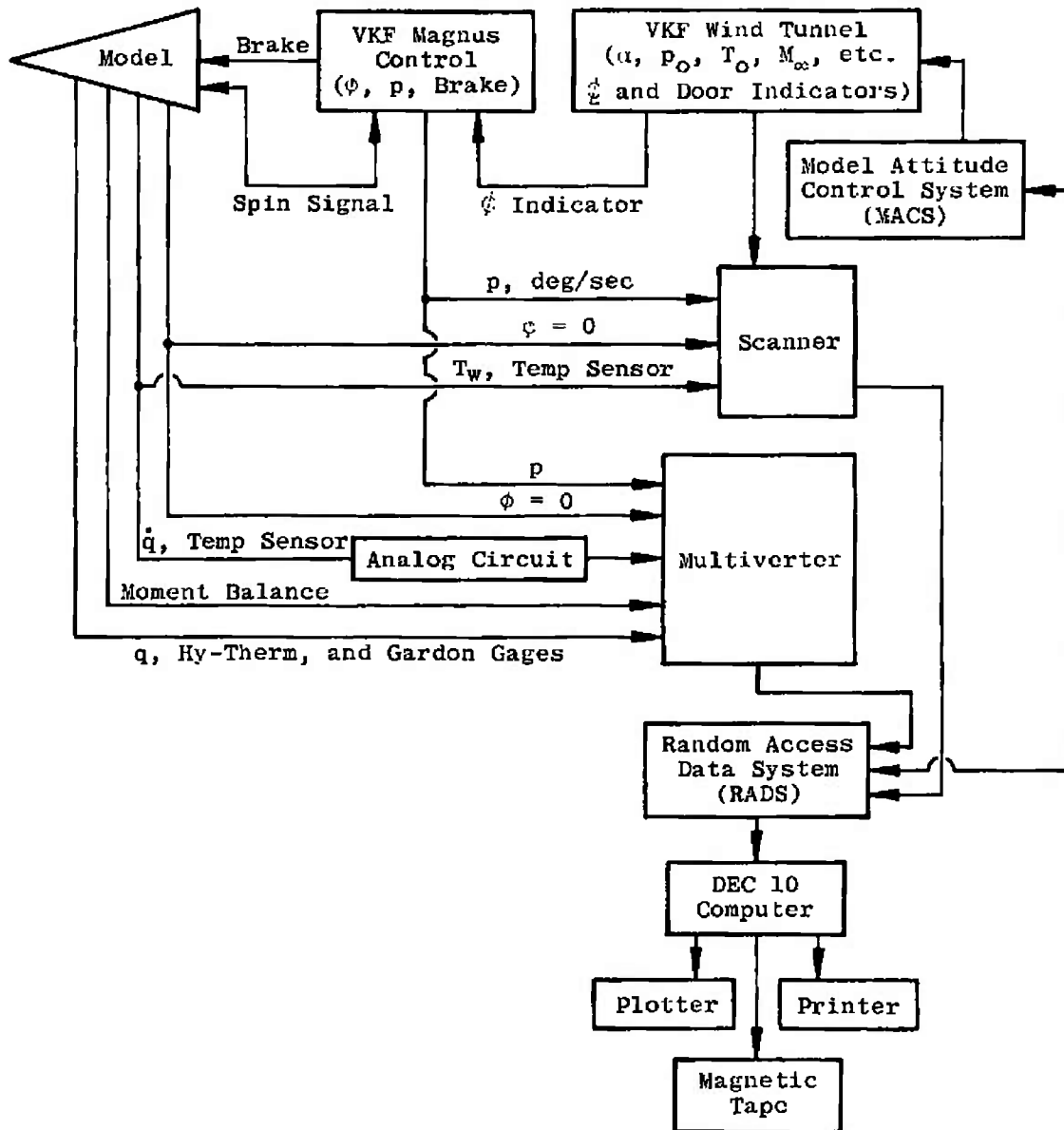


Figure 18. Instrumentation block diagram.

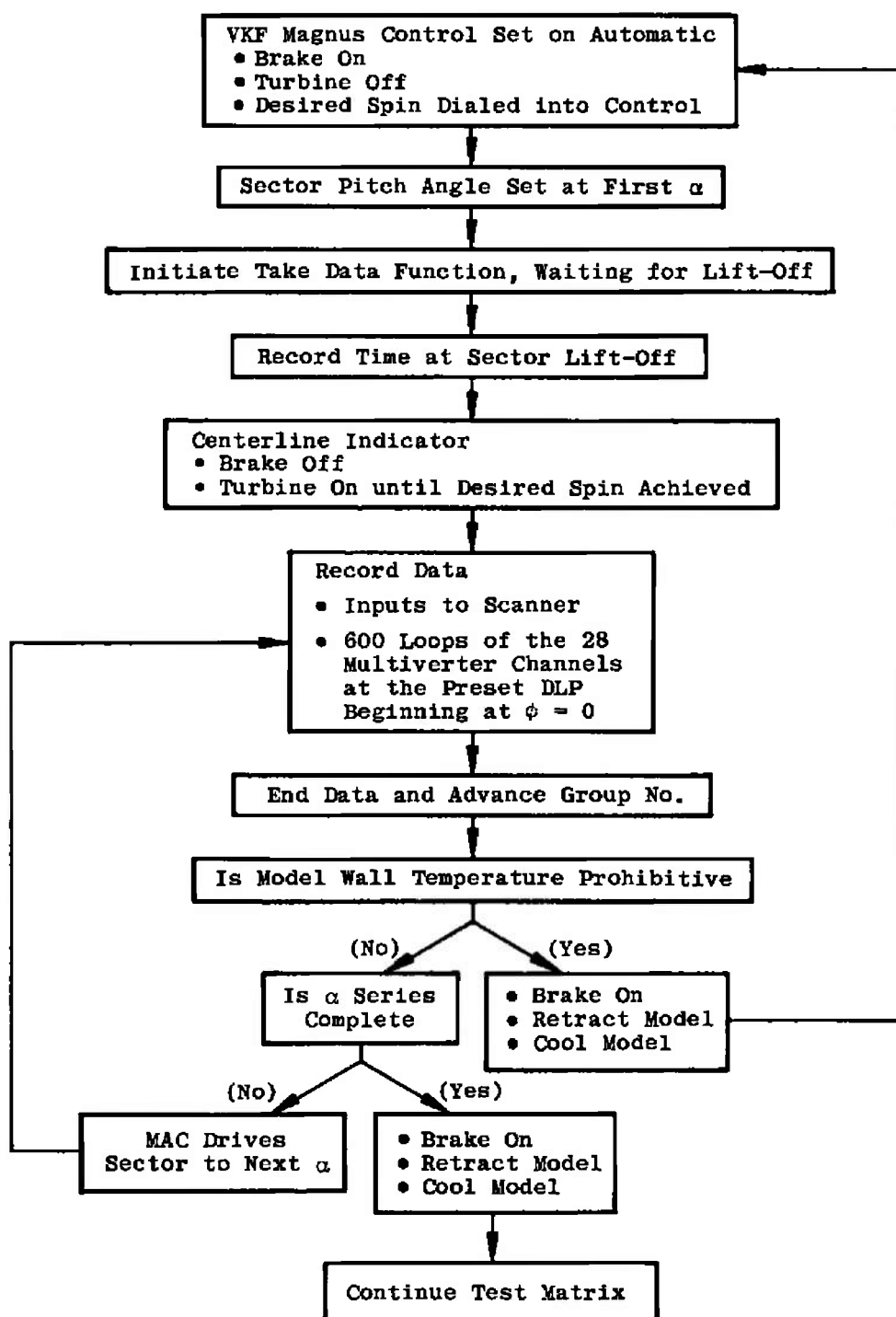


Figure 19. Dynamic data acquisition block diagram.

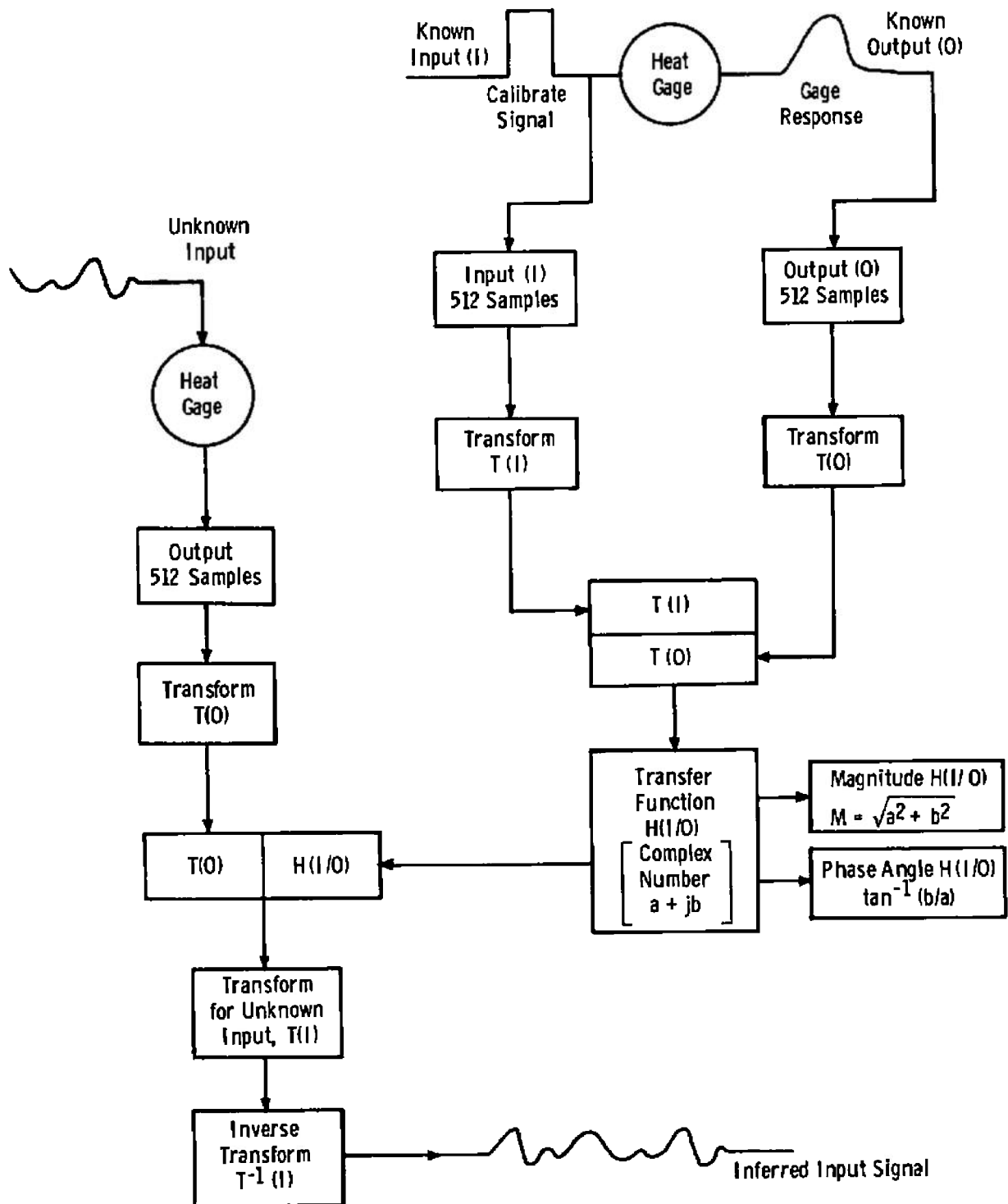
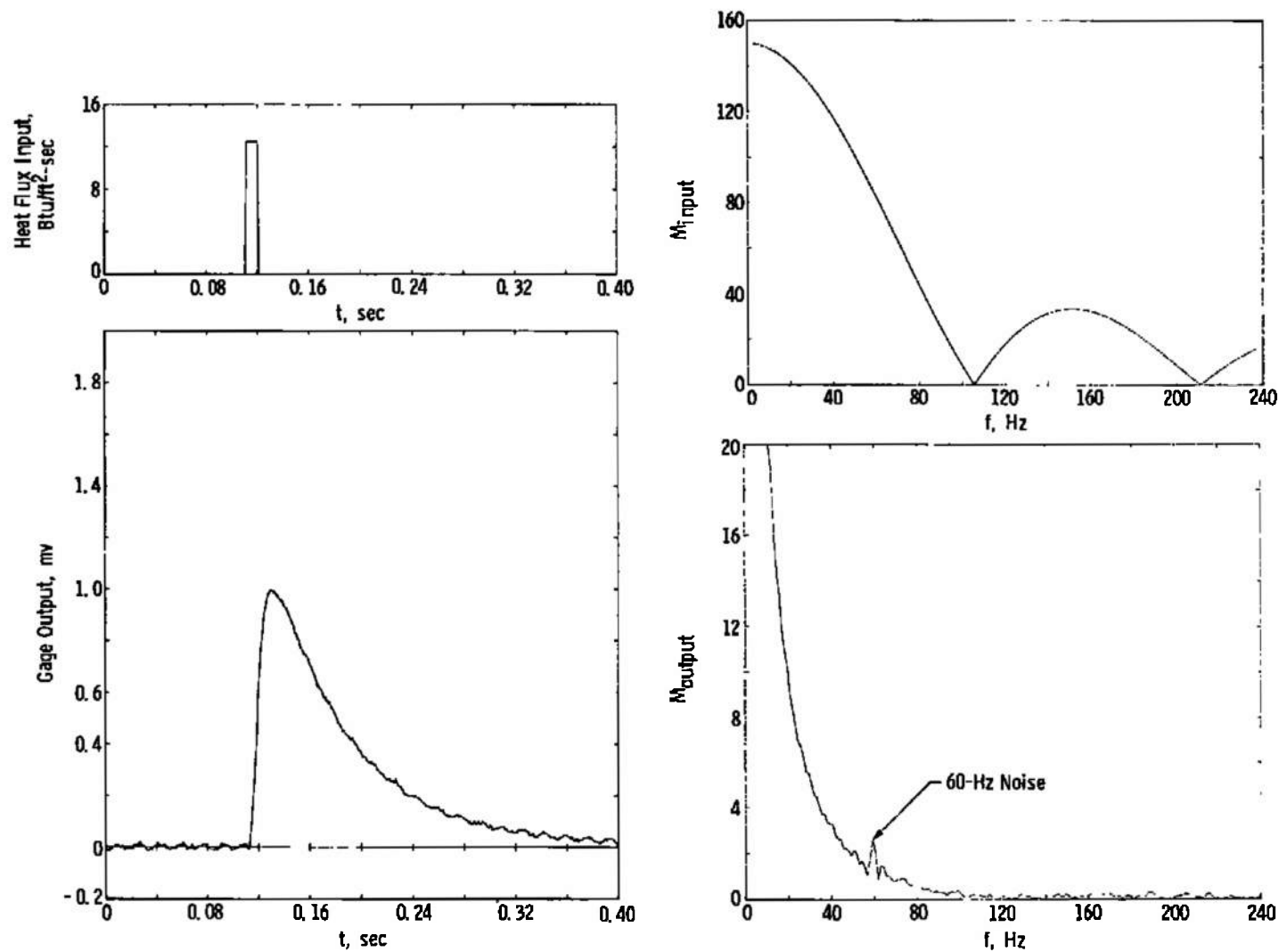
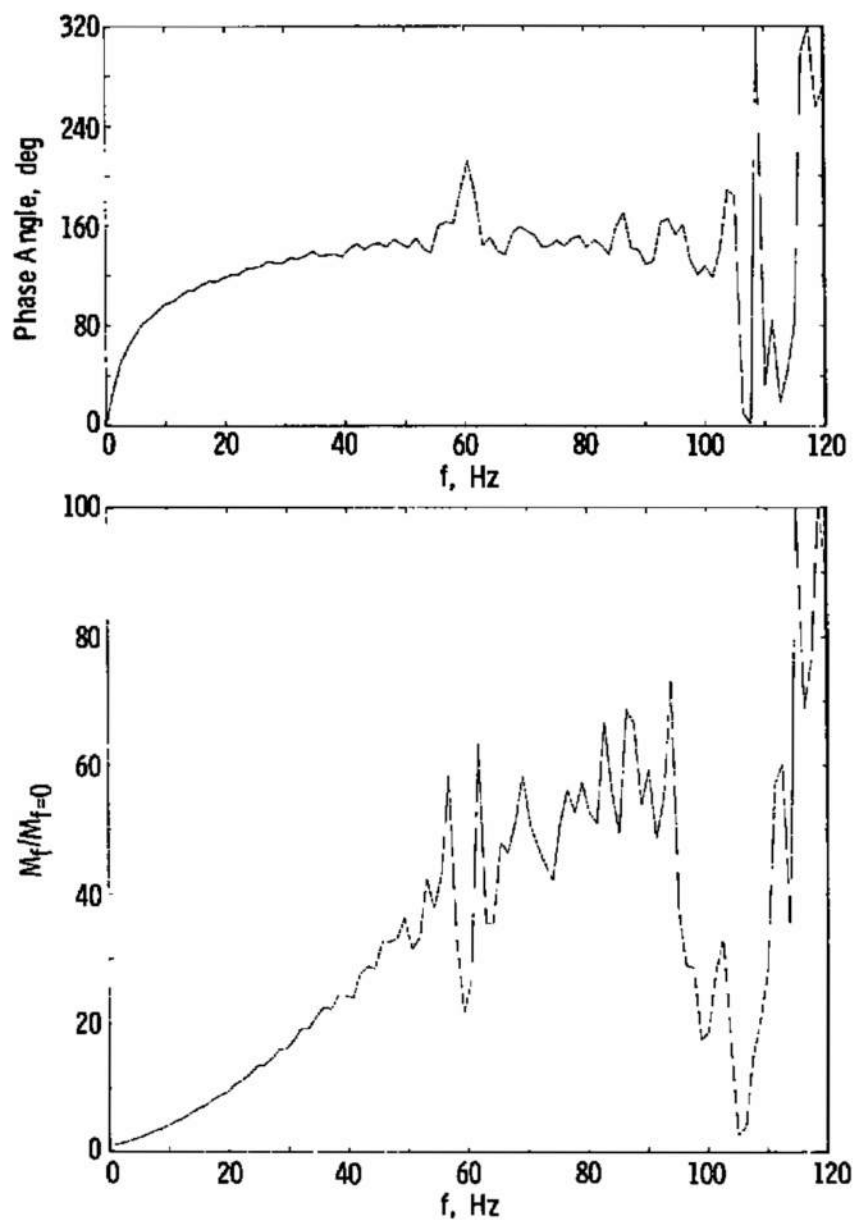


Figure 20. Dynamic data reduction diagram.

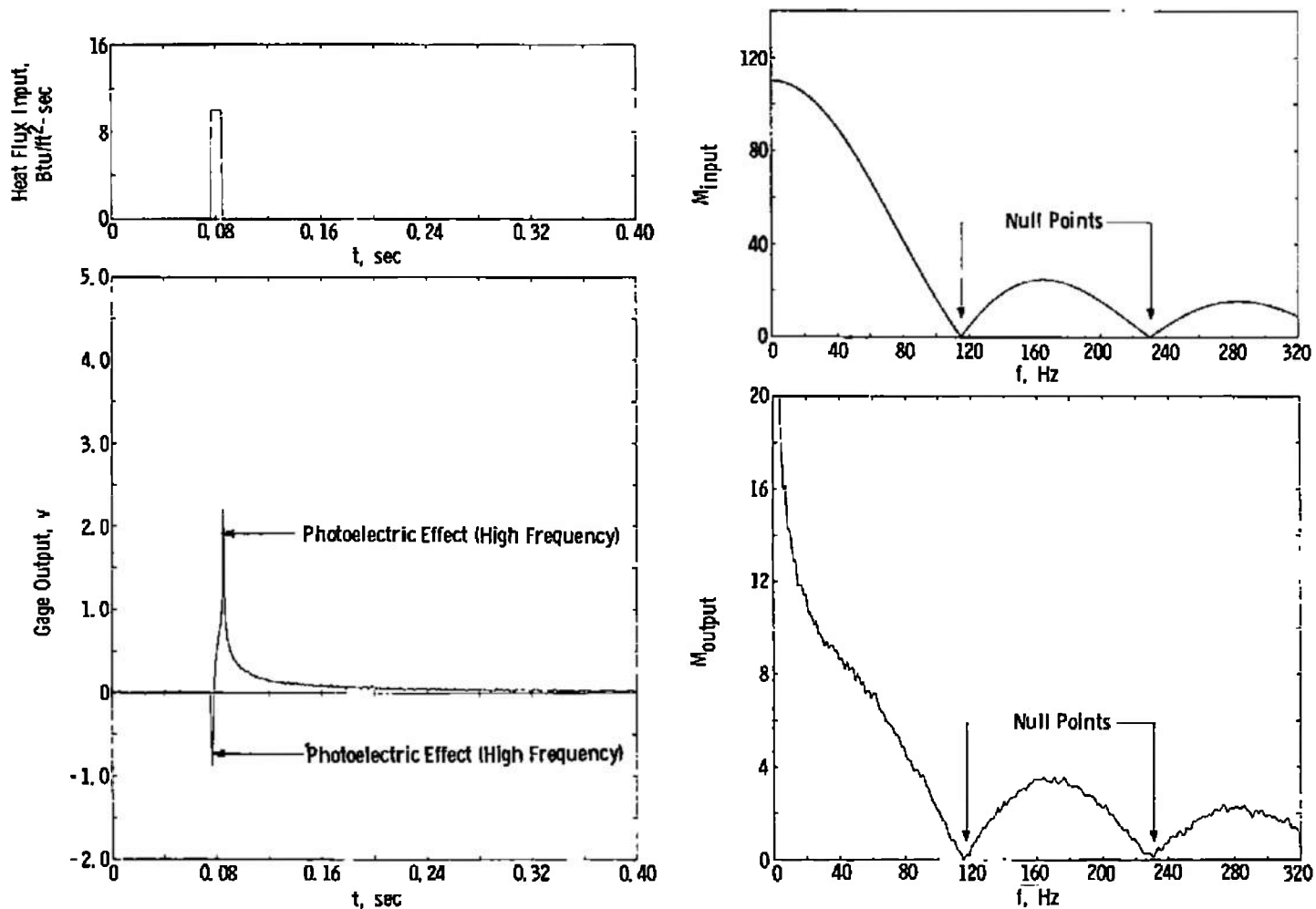


a. Gage input and output

Figure 21. Typical thermopile Gardon gage dynamic calibration.

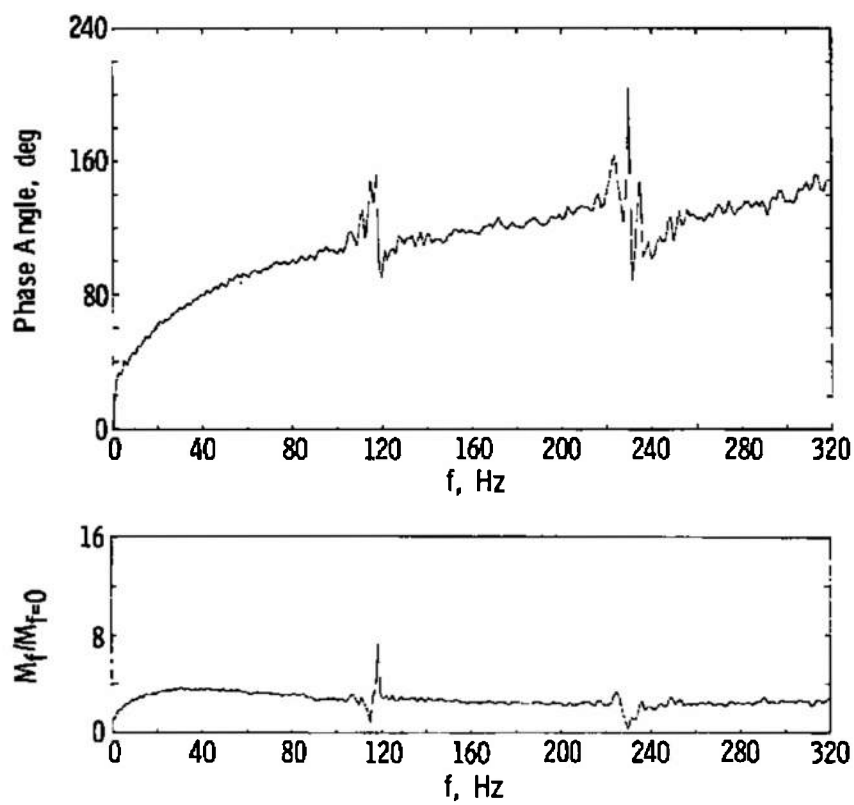


b. Gage transfer function
Figure 21. Concluded.

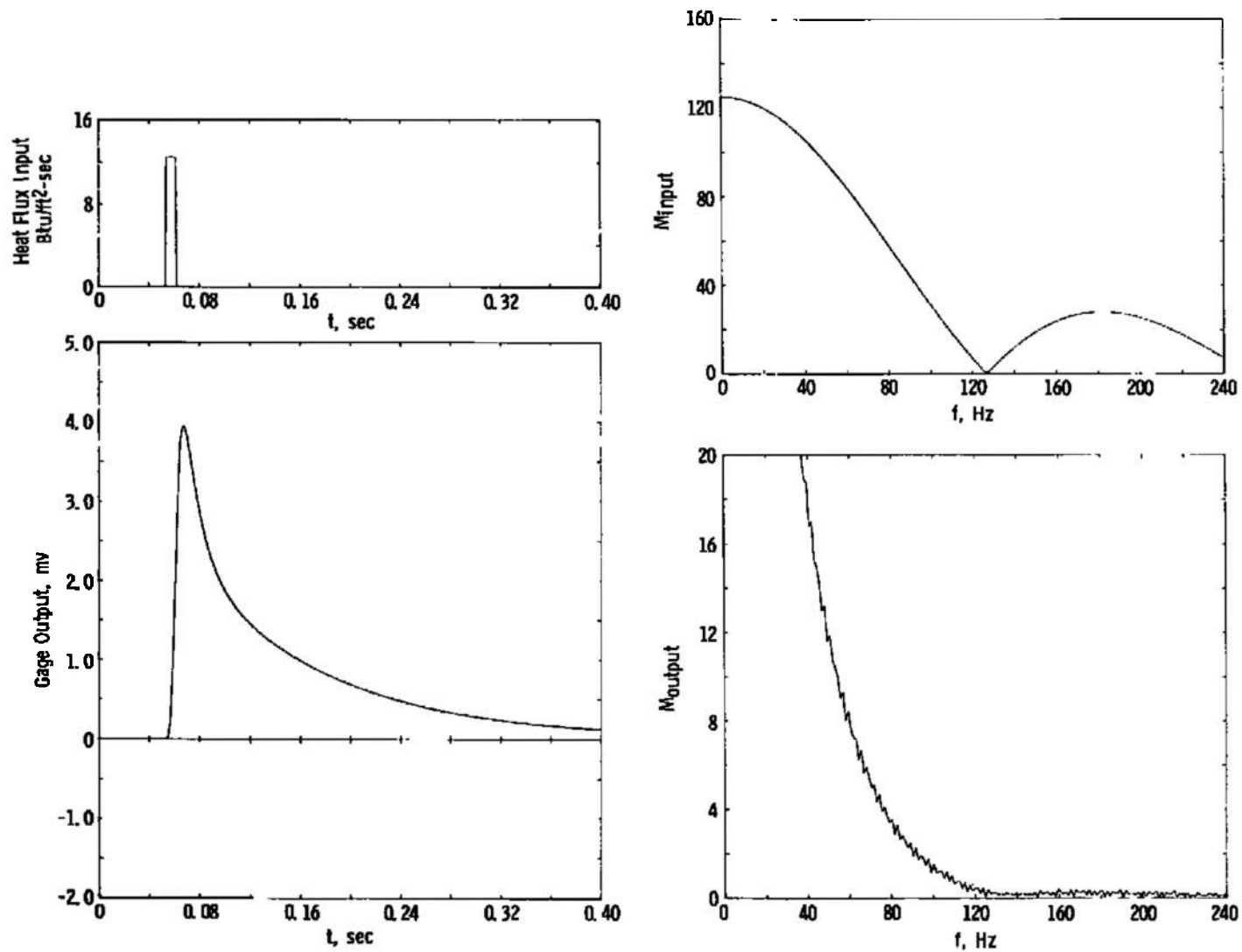


a. Gage input and output

Figure 22. Typical Temp-Sensor with analog circuit dynamic calibration.

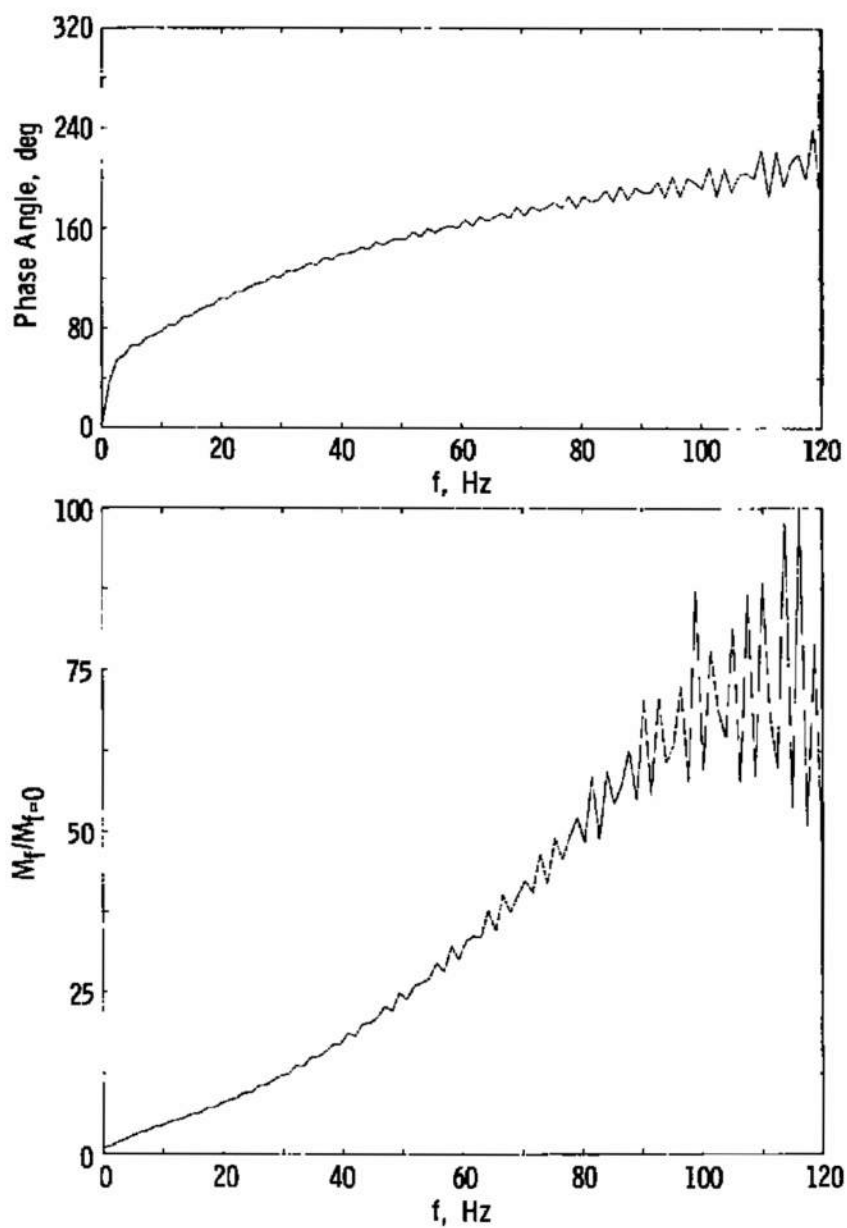


b. Gage transfer function
Figure 22. Concluded.

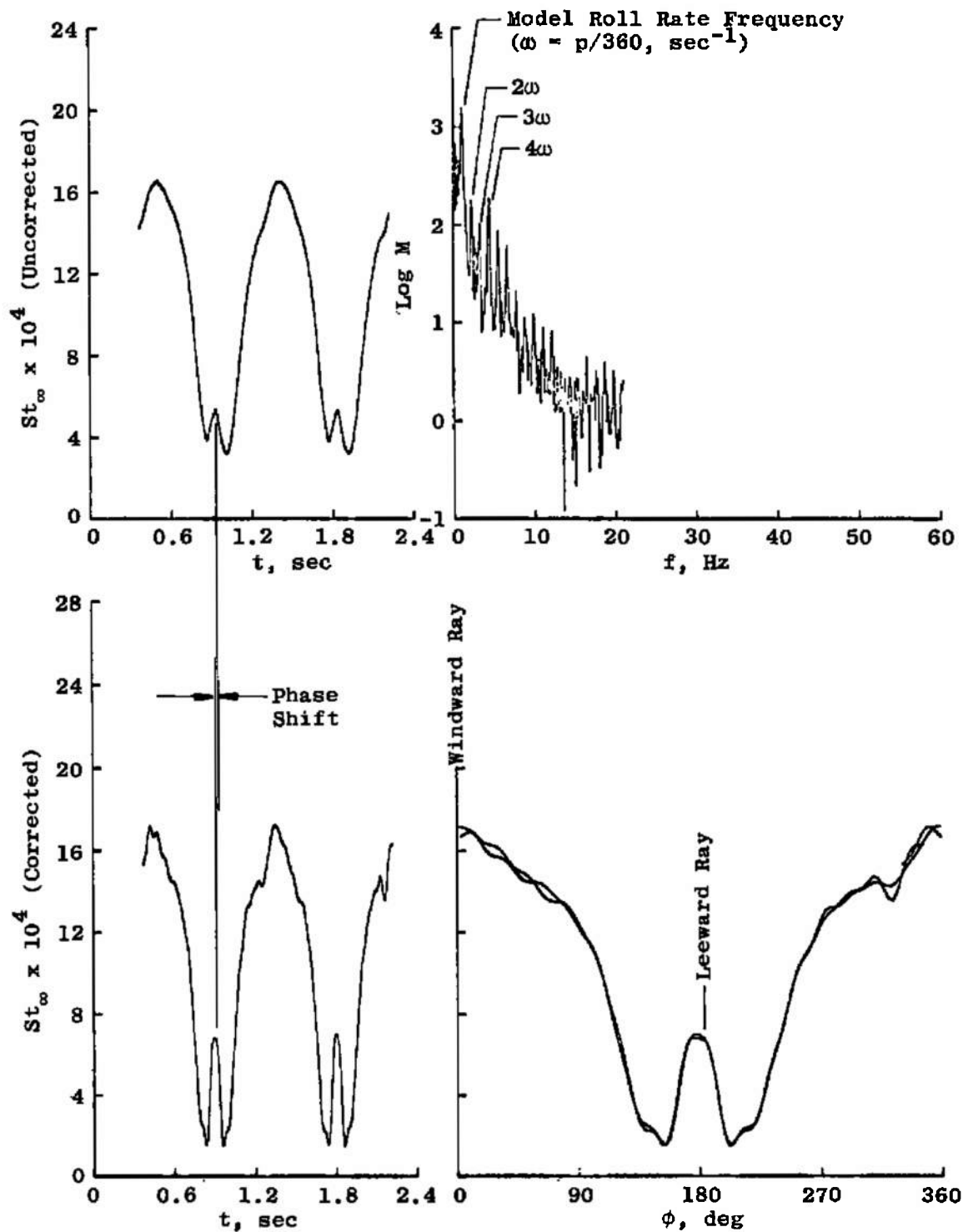


a. Gage input and output

Figure 23. Typical Hy-Therm gage dynamic calibration.

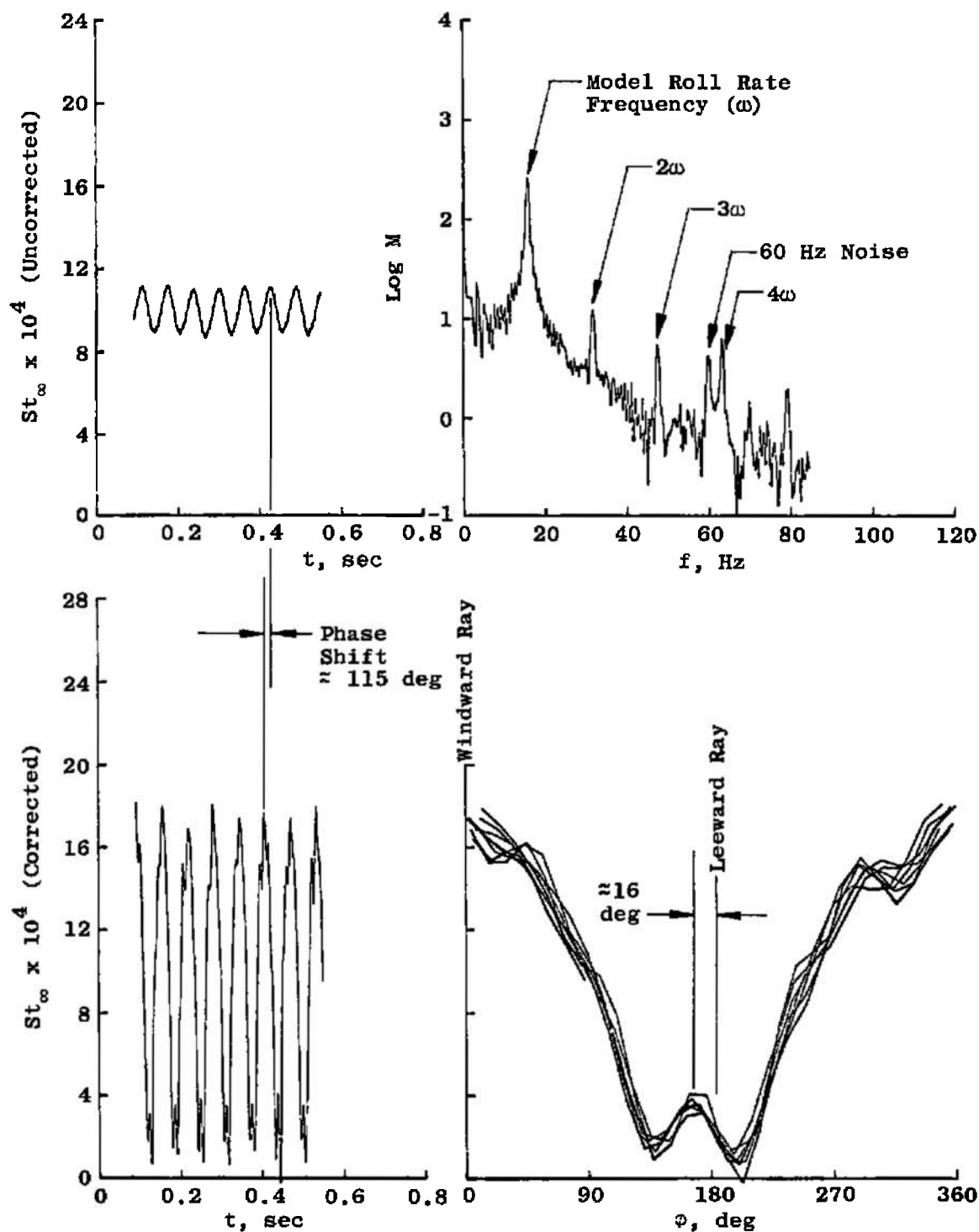


b. Gage transfer function
Figure 23. Concluded.



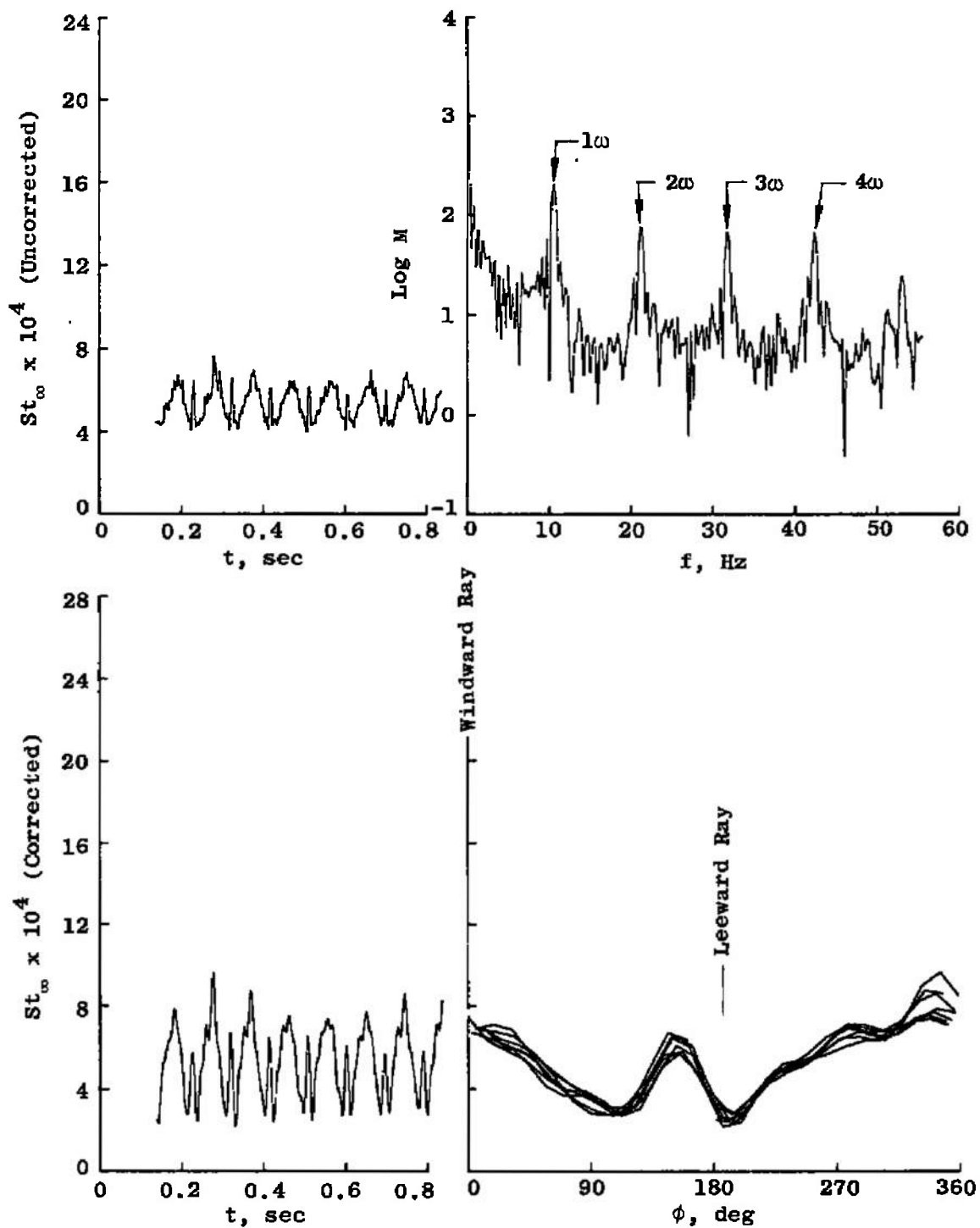
a. Gardon gage 8, $x/l = 0.791$,
 $p = 402 \text{ deg/sec}$, $\alpha = 3 \text{ deg}$

Figure 24. Representative dynamic heat-transfer rate data.



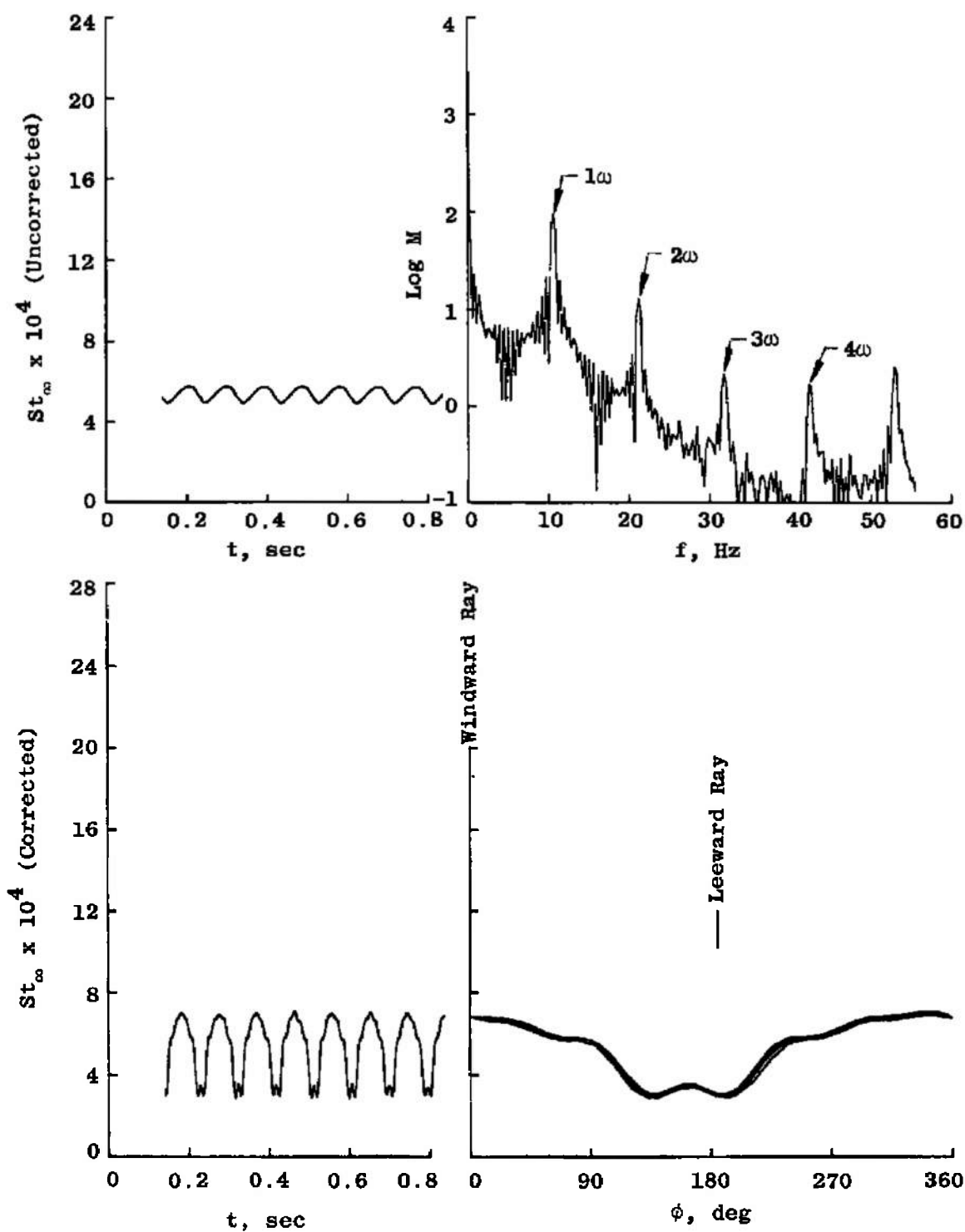
b. Gardon gage, $x/L = 0.791$, $p = 5,726$
deg/sec, $\alpha = 3$ deg

Figure 24. Continued.



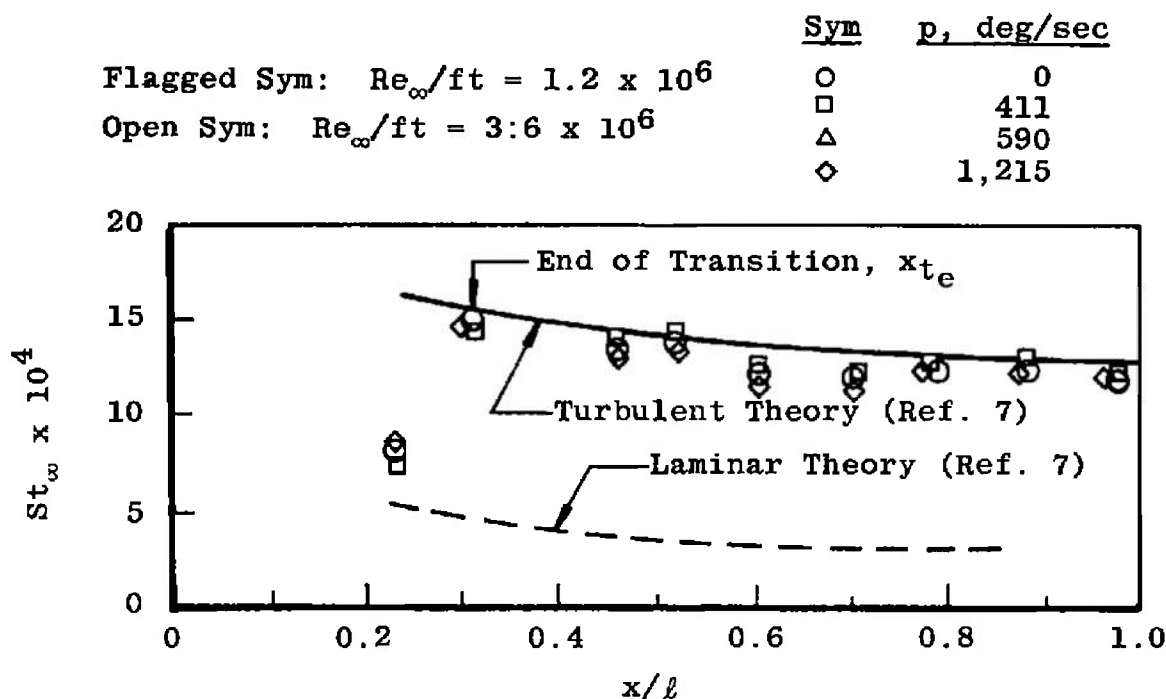
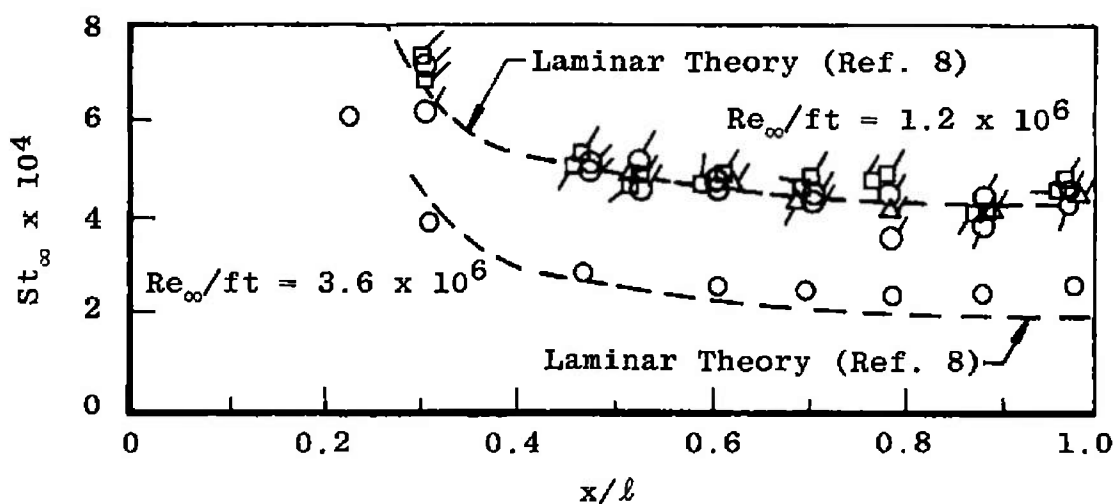
c. Temp sensor, gage 17, $x/L = 0.656$, $p = 3,842$
deg/sec, $\alpha = 3$ deg

Figure 24. Continued.



d. Hy-Therm gage 19, $x/L = 0.838$, $p = 3,842$
deg/sec, $\alpha = 3^\circ$

Figure 24. Concluded.

a. $\alpha = 0$, sharp cone, $Re_\infty/ft = 3.6 \times 10^6$ b. $\alpha = 0$, $r_n/r_b = 0.20$ blunt cone
Figure 25. Heat-transfer distributions at $M_\infty = 8$.

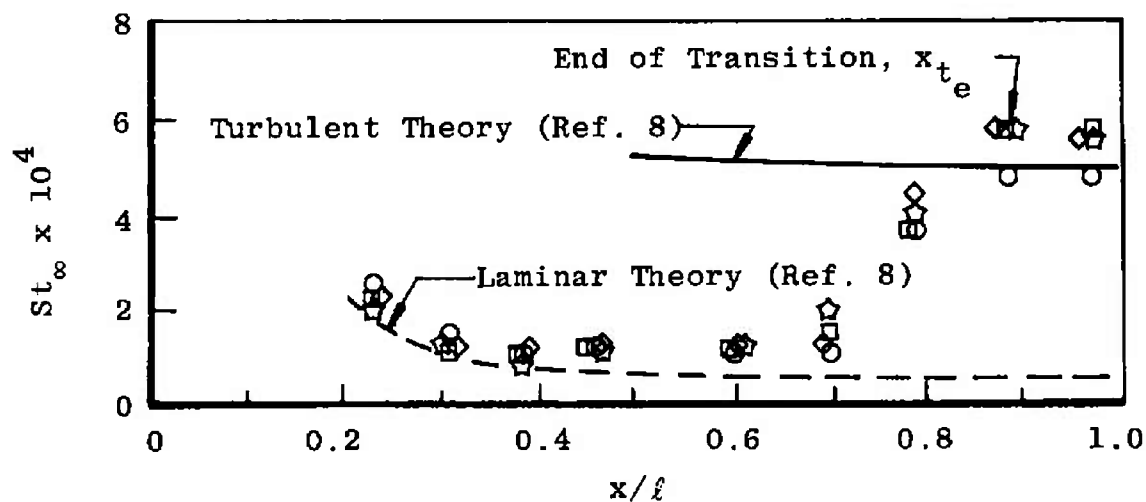
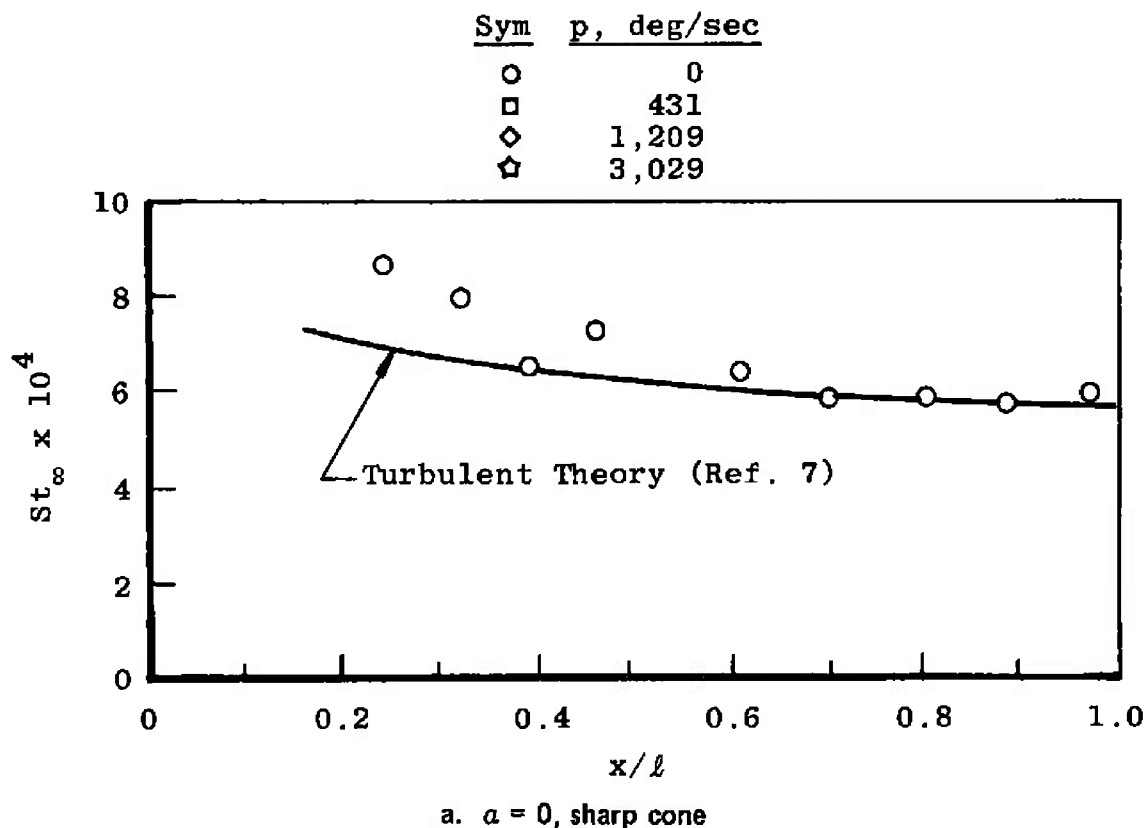


Figure 26. Heat-transfer distributions at $M_\infty \approx 5.06$,
 $Re_\infty/ft = 6 \times 10^6$.

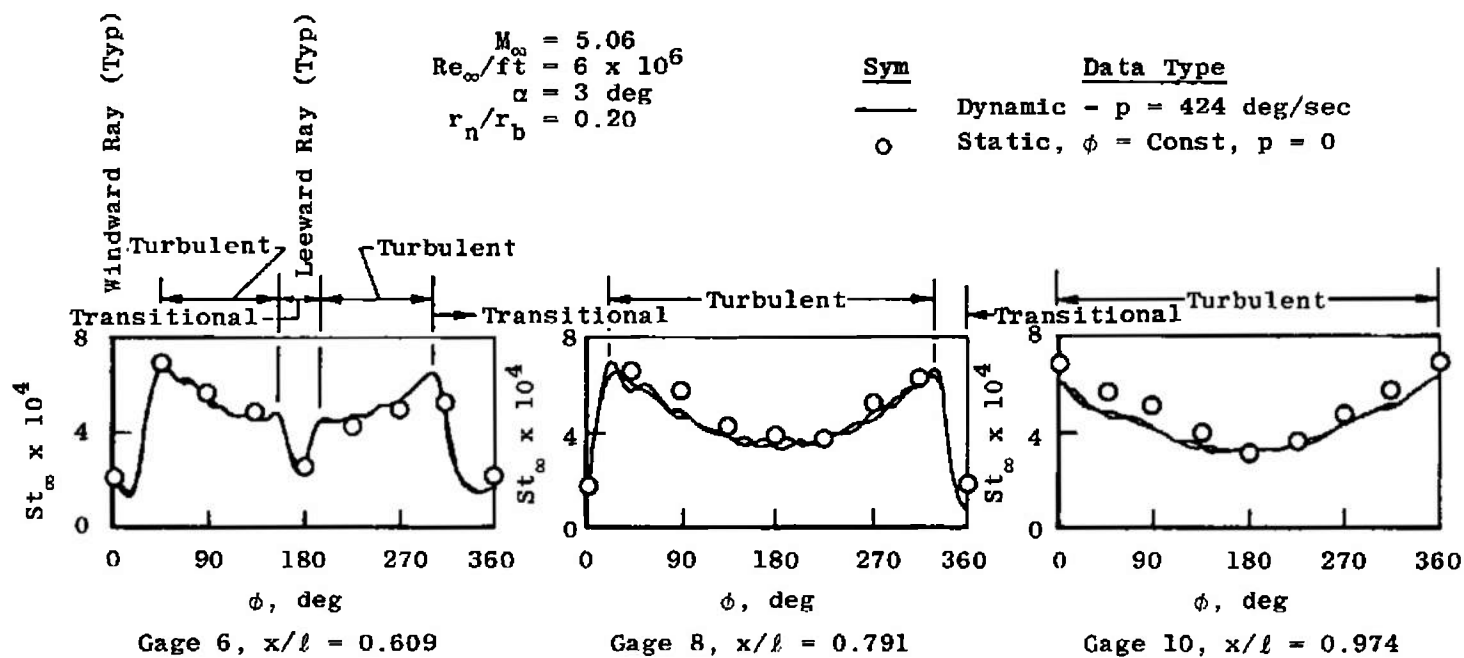


Figure 27. Circumferential heat-transfer rate comparison between static and dynamic data.

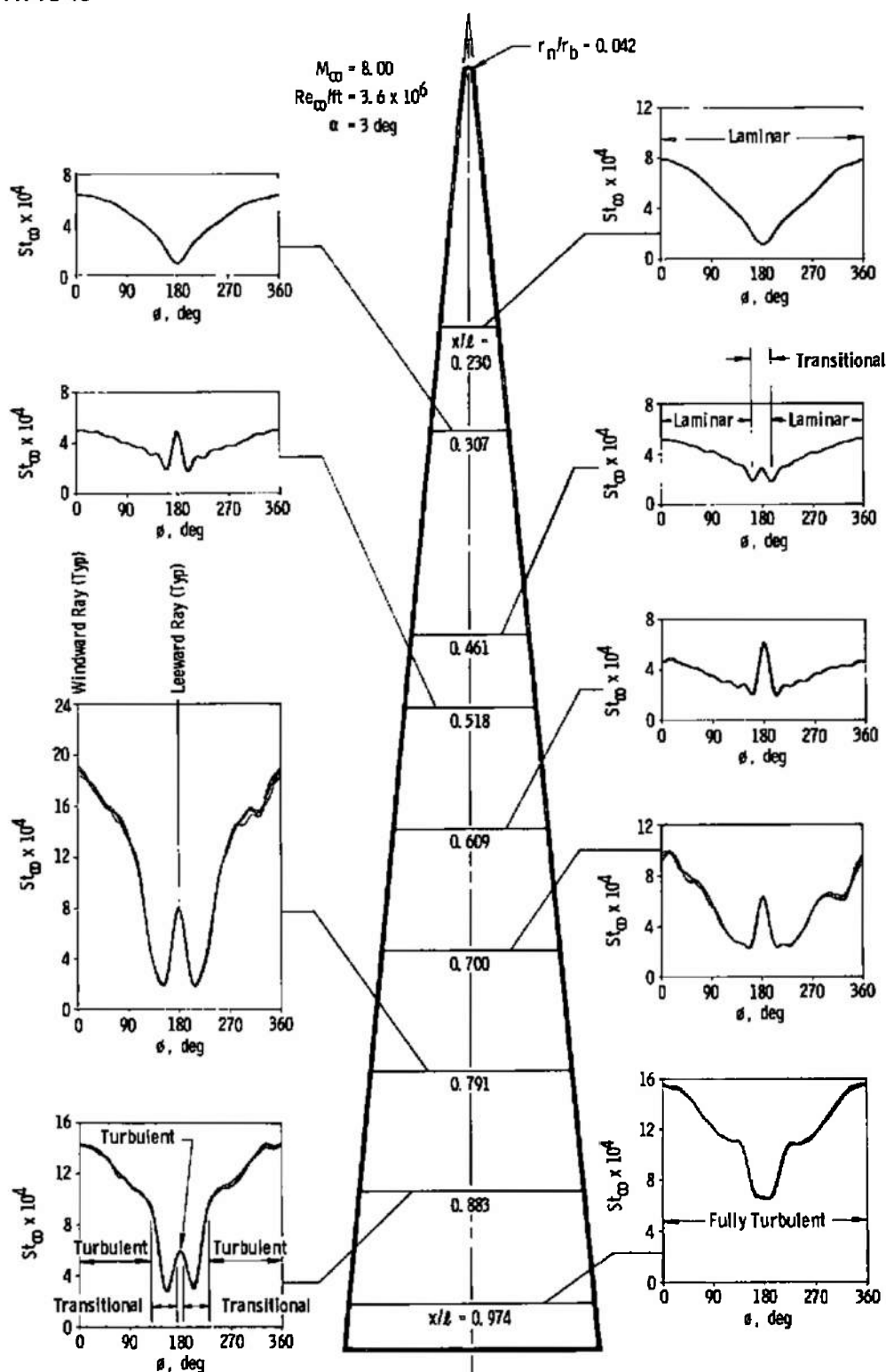


Figure 28. Typical heat-transfer distributions with model spinning, $p = 402$ deg/sec.

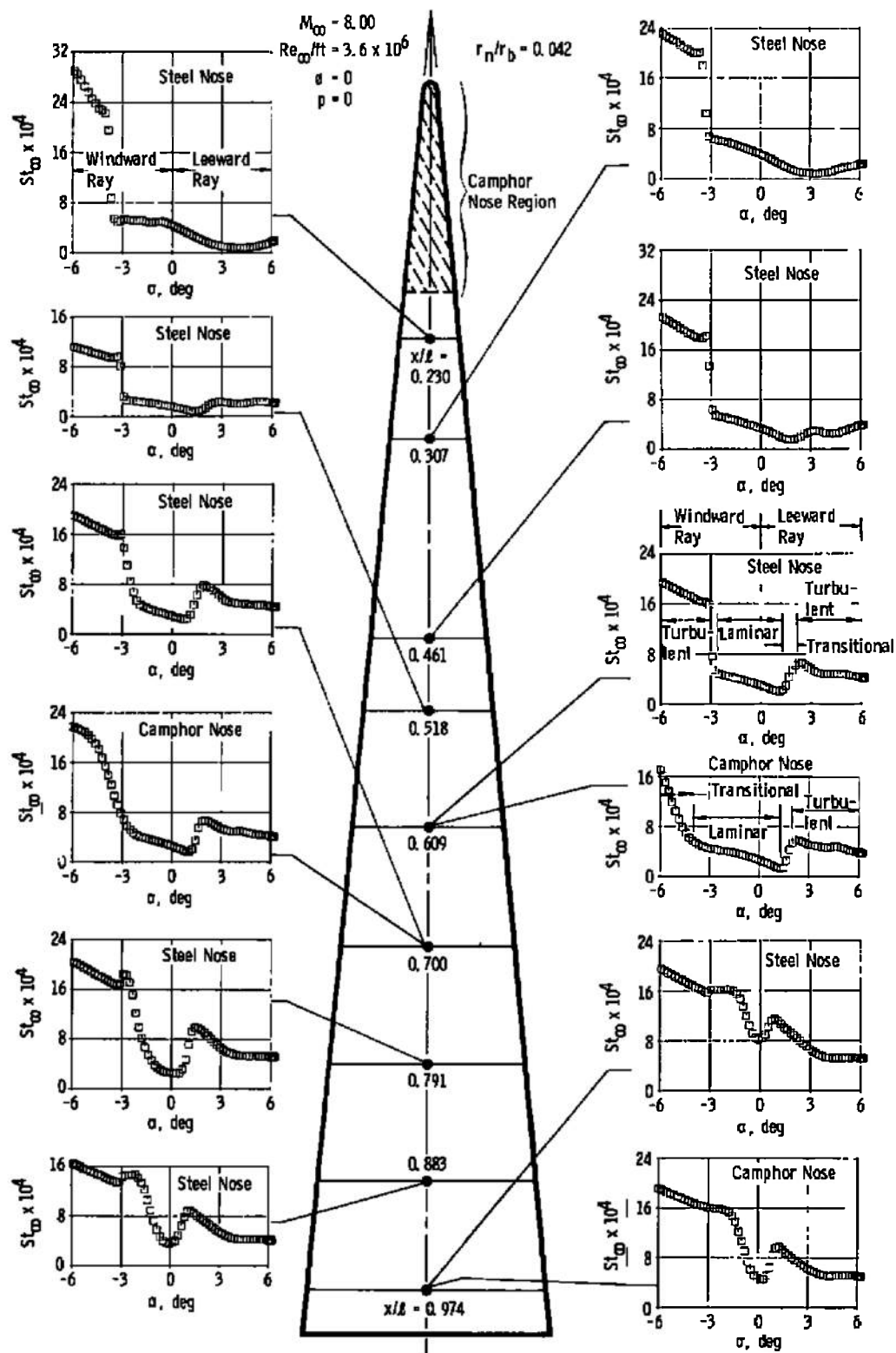


Figure 29. Typical heat transfer distributions with angle of attack with and without ablation.

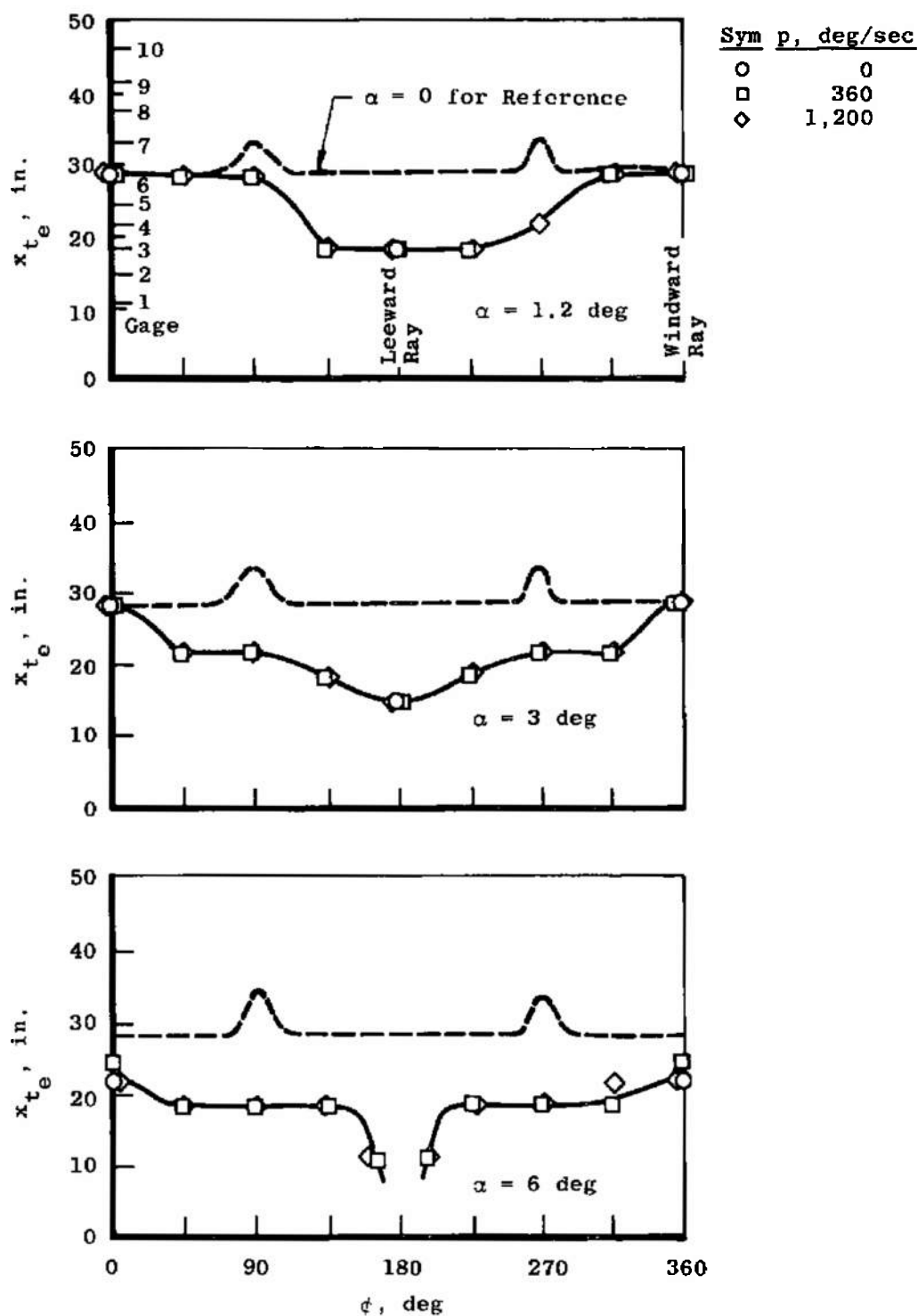


Figure 30. End of transition distribution, $r_n/r_b = 0.042$ spherical, $M_\infty = 5.06$, $Re_\infty/ft = 6 \times 10^6$.

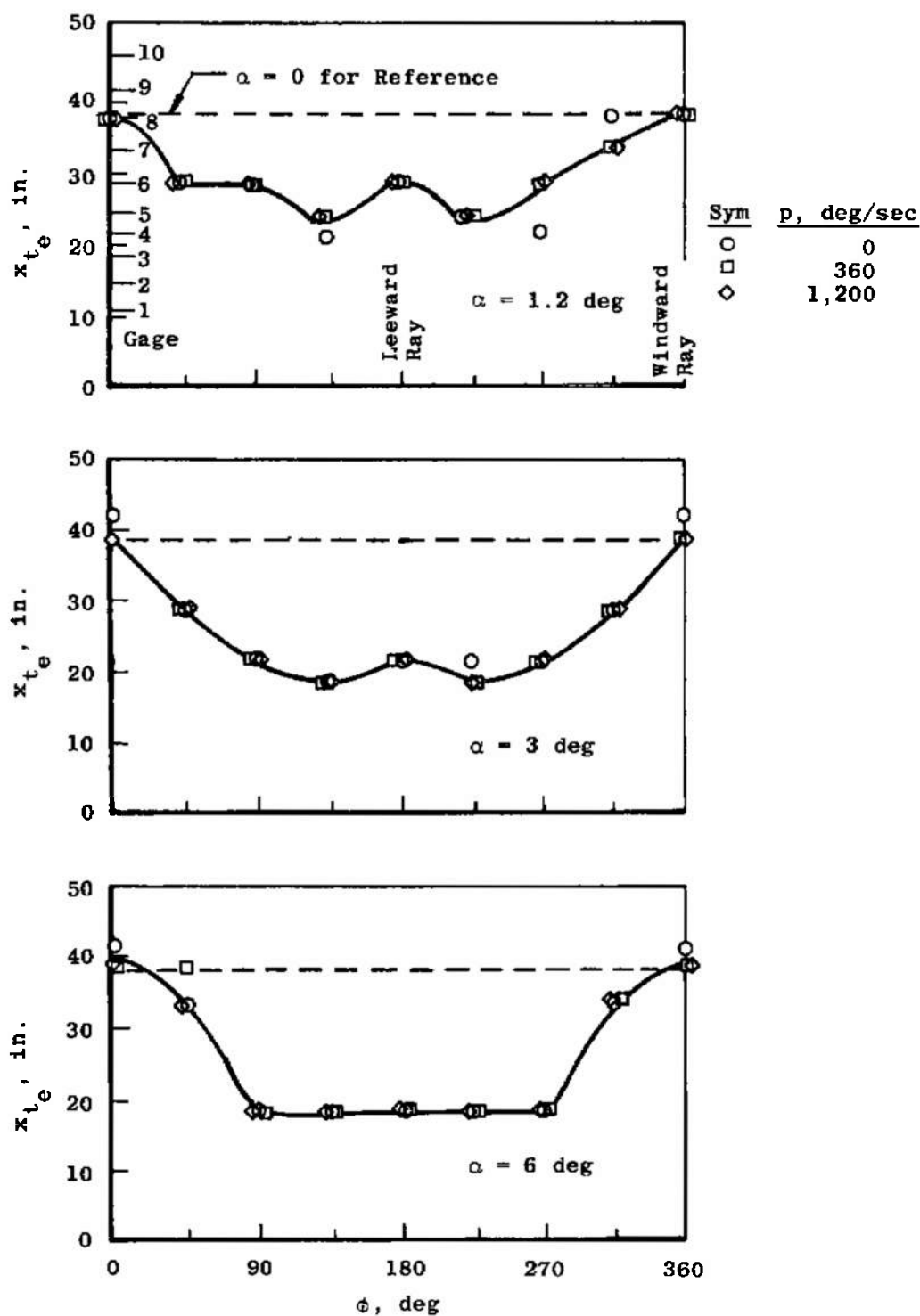


Figure 31. End of transition distribution, $r_n/r_b = 0.12$ spherical, $M_\infty = 5.06$, $Re_\infty/ft = 6 \times 10^6$.

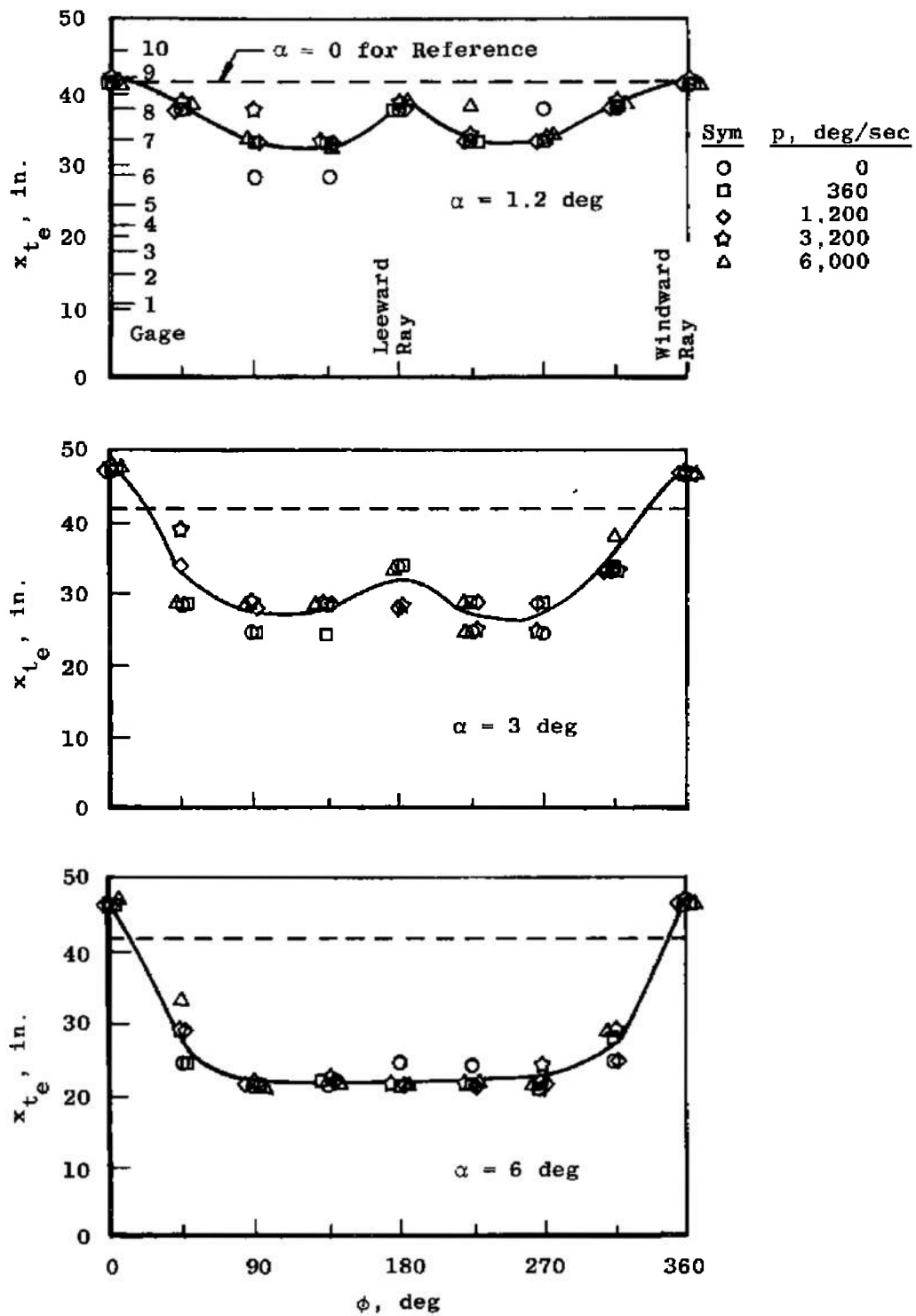
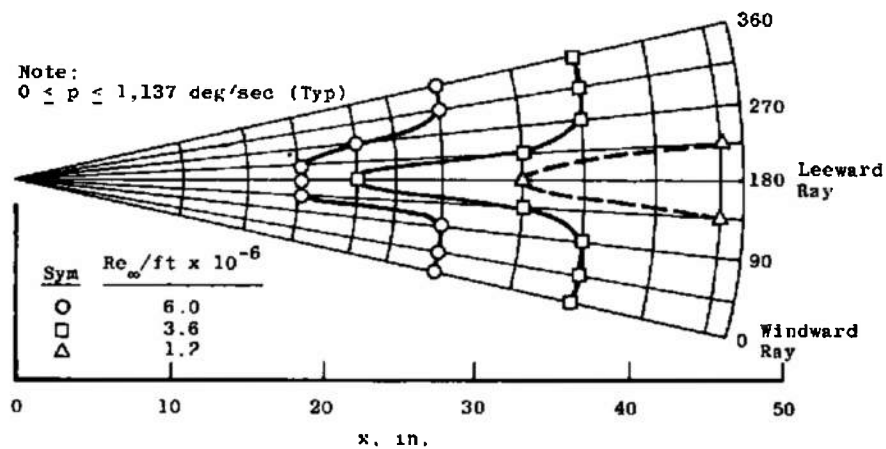
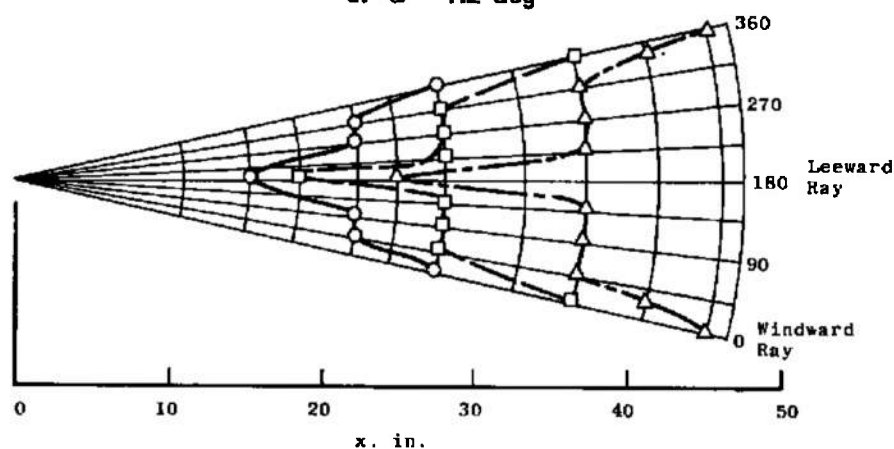


Figure 32. End of transition distribution, r_n/r_b spherical, $M_\infty = 5.06$, $Re_{x_{te}} = 6 \times 10^6$.

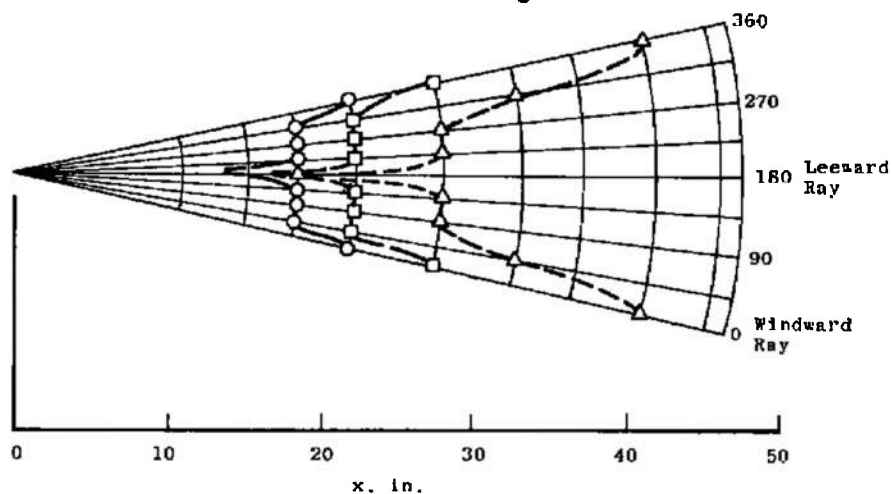
Note:
 $0 \leq p \leq 1,137 \text{ deg/sec (Typ)}$



a. $\alpha = 1.2 \text{ deg}$



b. $\alpha = 3 \text{ deg}$



c. $\alpha = 6 \text{ deg}$

Figure 33. End of transition mapping, $r_n/r_b = 0.042$
 spherical, $M_{\infty} \approx 5$.

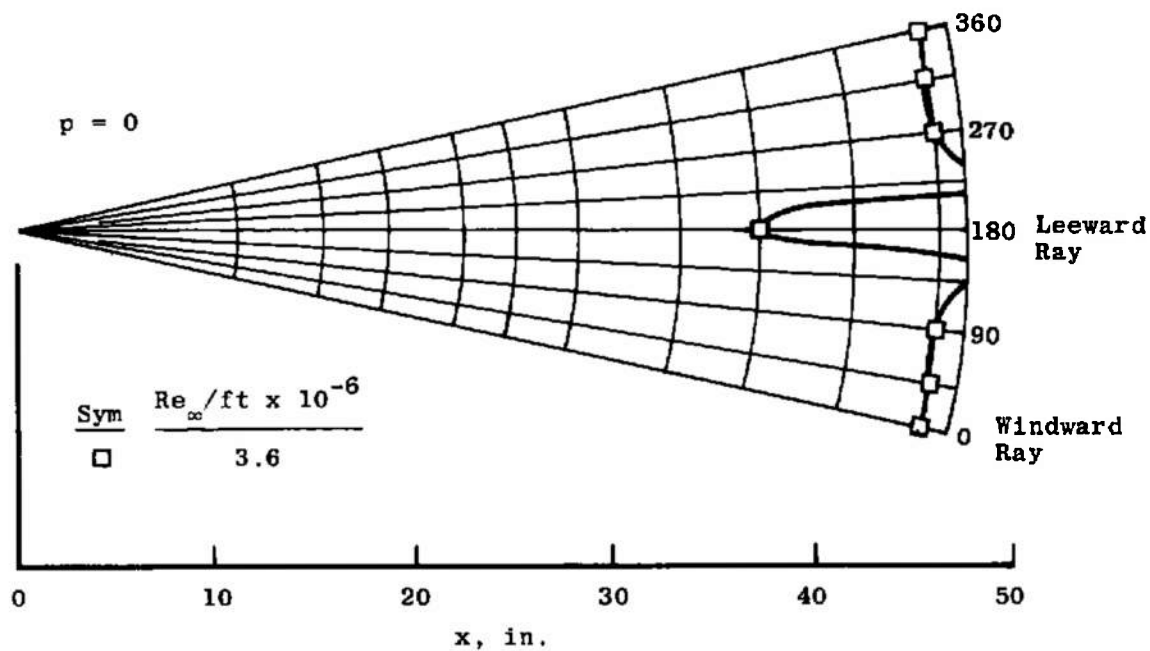
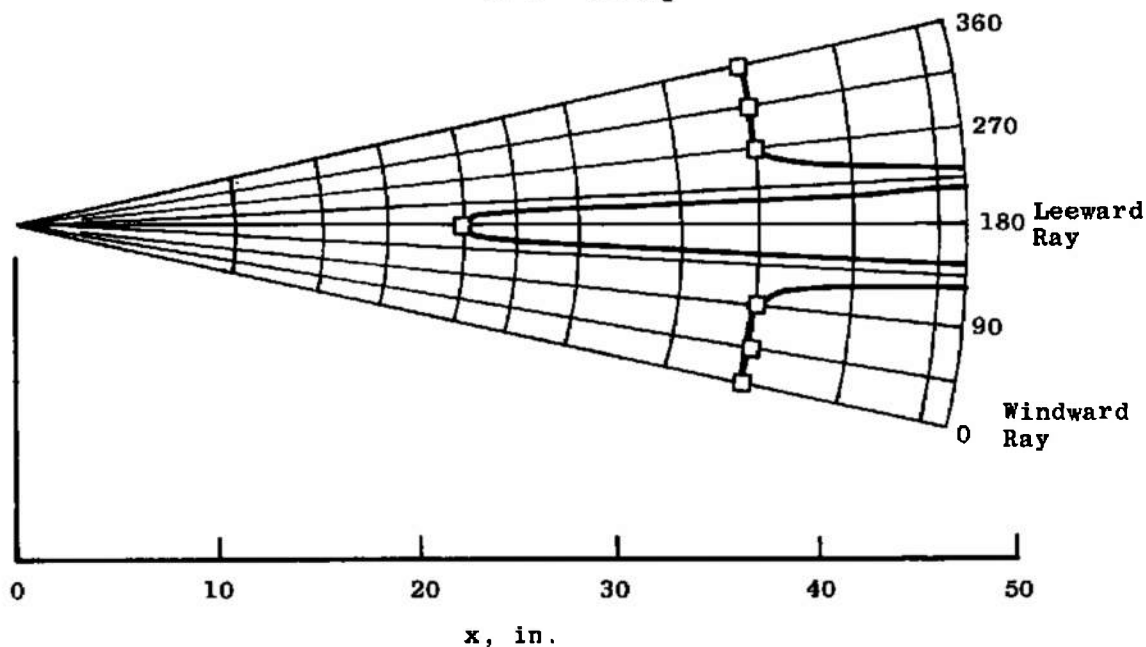
a. $\alpha = 1.2$ degb. $\alpha = 3$ deg

Figure 34. End of transition mapping, $r_n/r_b = 0.042$
spherical, $M_{\infty} \approx 8$.

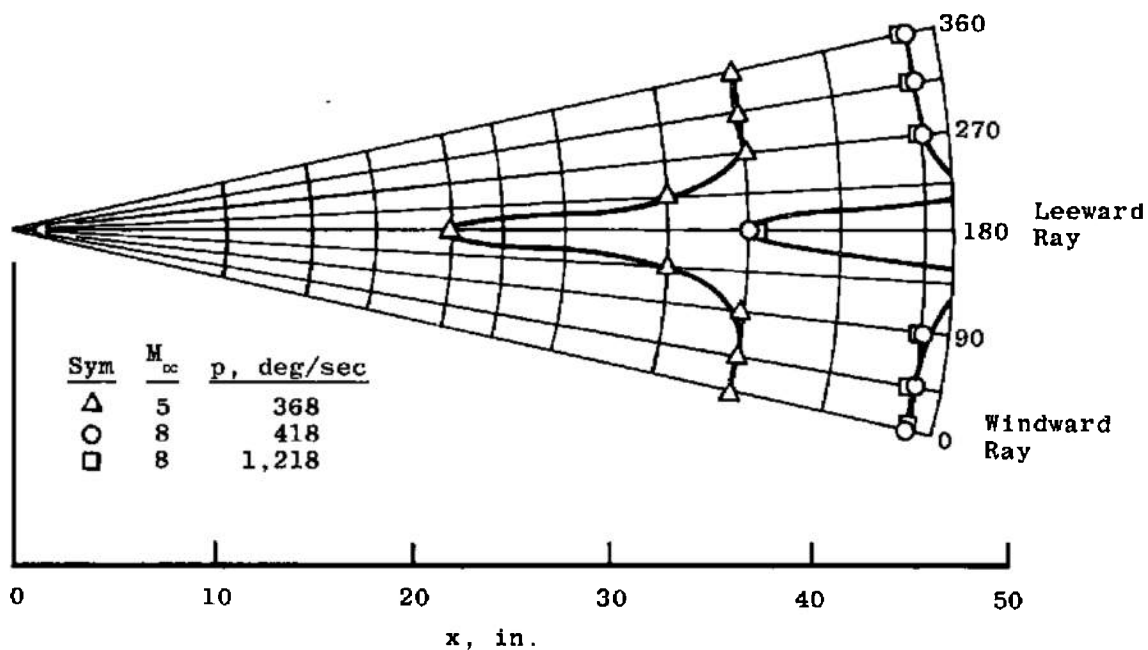
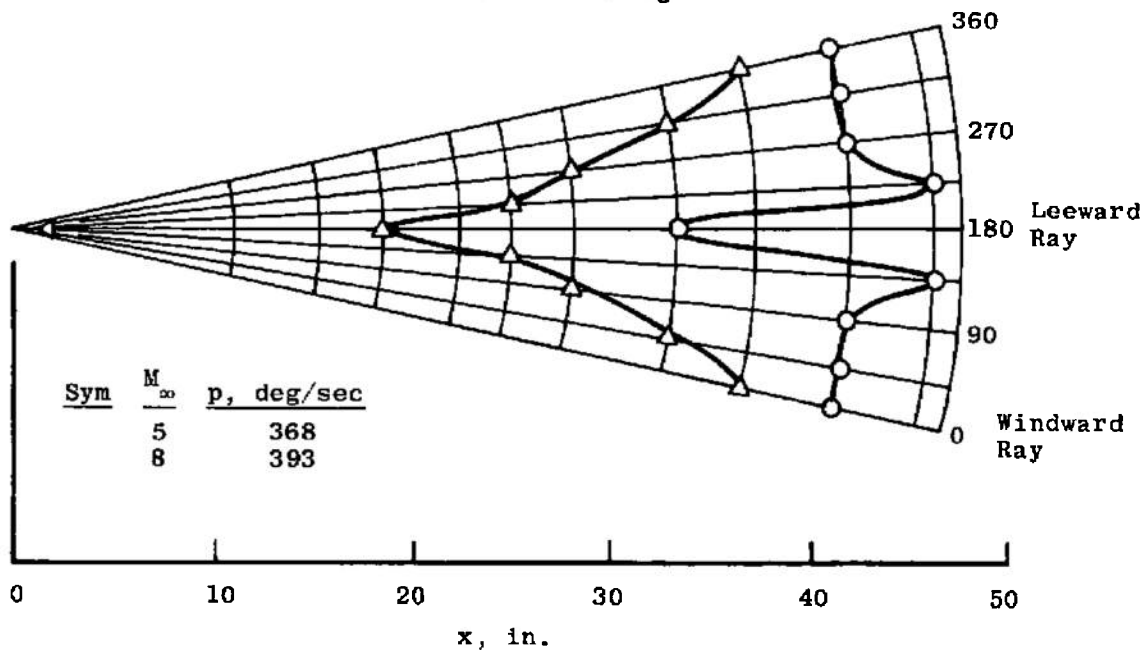
a. $\alpha = 1.2$ degb. $\alpha = 3$ deg

Figure 35. End of transition mapping, $r_n/r_b = 0.042$ Biconic,
 $Re_\infty/ft = 3.6 \times 10^6$, $M_\infty \approx 5$ and 8.

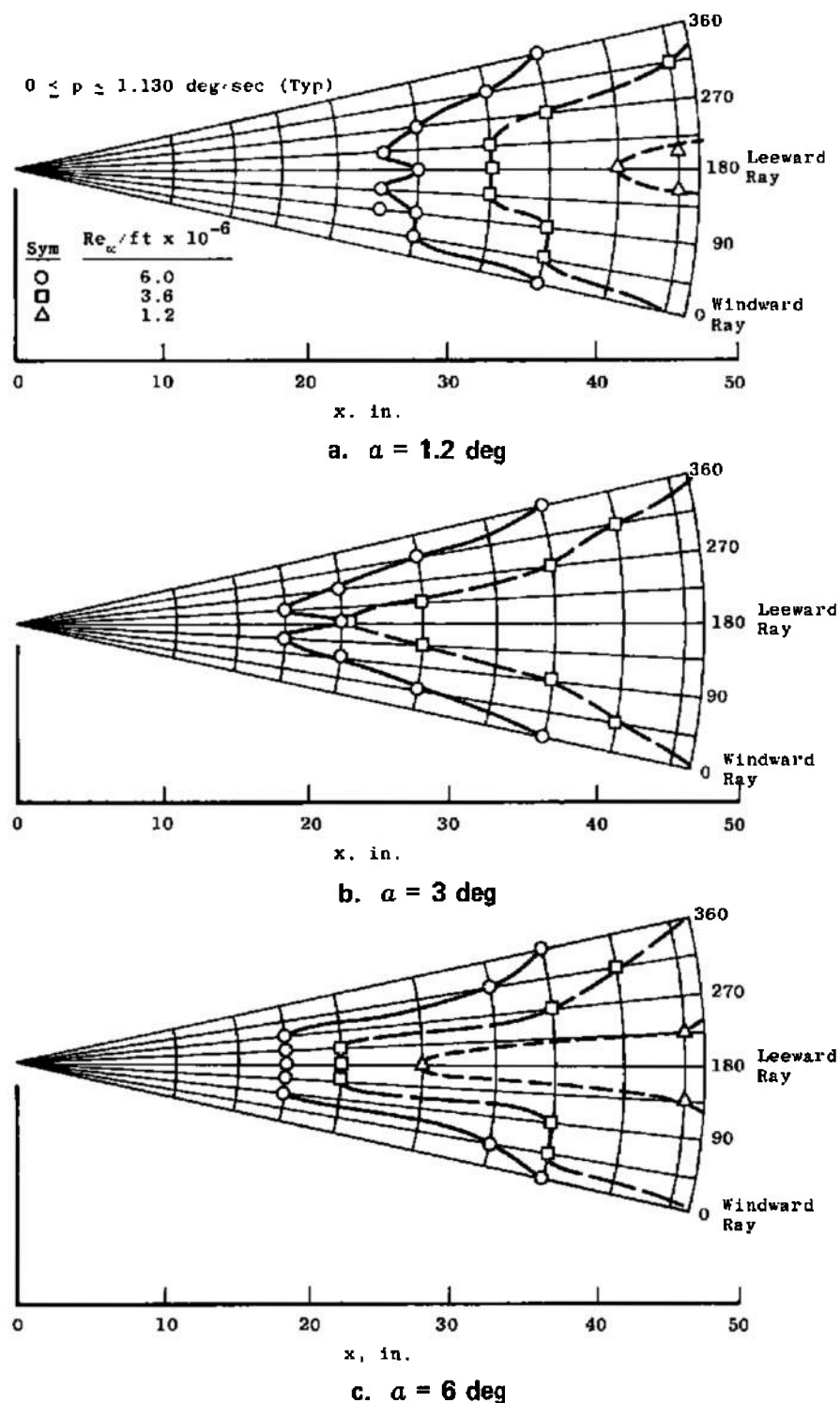


Figure 36. End of transition mapping, $r_n/r_b = 0.12$ spherical, $M_{\infty} \approx 5$.

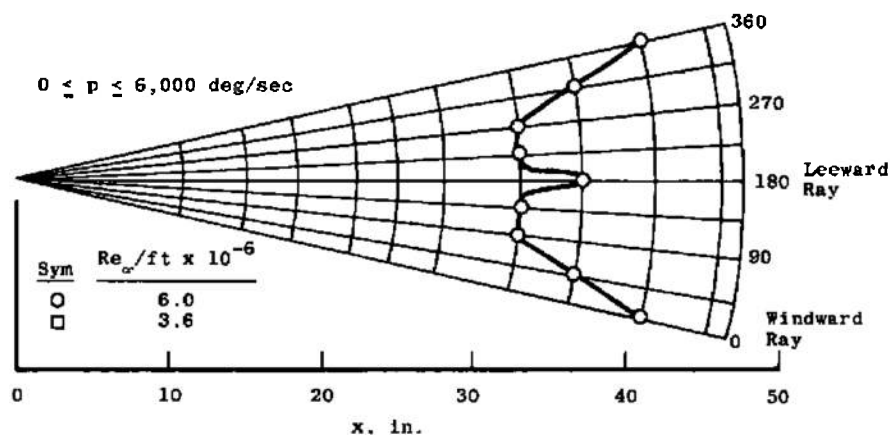
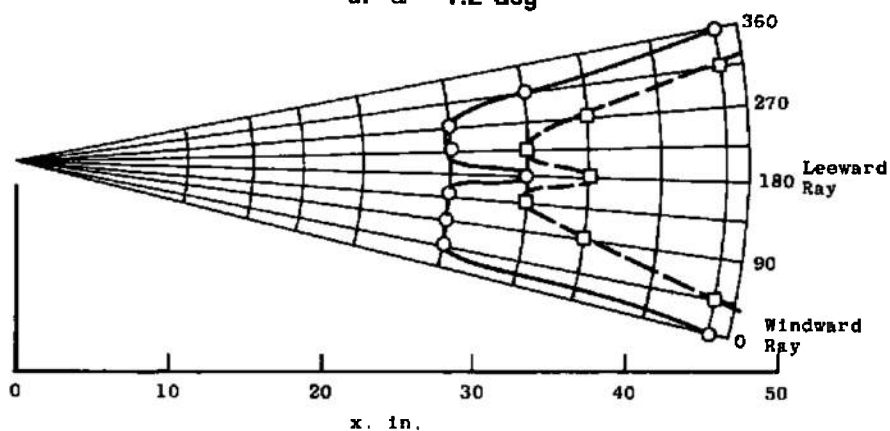
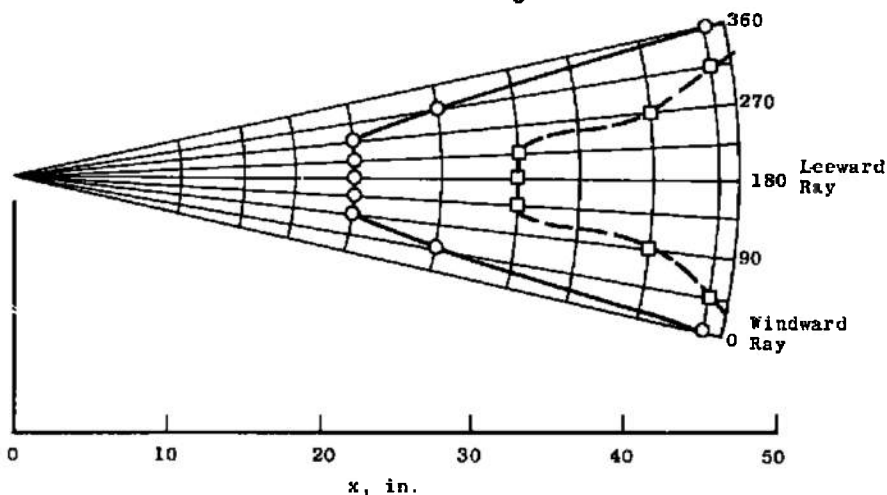
a. $\alpha = 1.2$ degb. $\alpha = 3$ degc. $\alpha = 6$ deg

Figure 37. End of transition mapping, $r_n/r_b = 0.20$, spherical, $M_{\infty} \approx 5$.

$M_\infty = 7.95$
 $Re_\infty/ft = 1.2 \times 10^6$
 $\alpha = 6 \text{ deg}$
 $r_n/r_b = 0.013$
 $p = 330 \text{ deg/sec}$

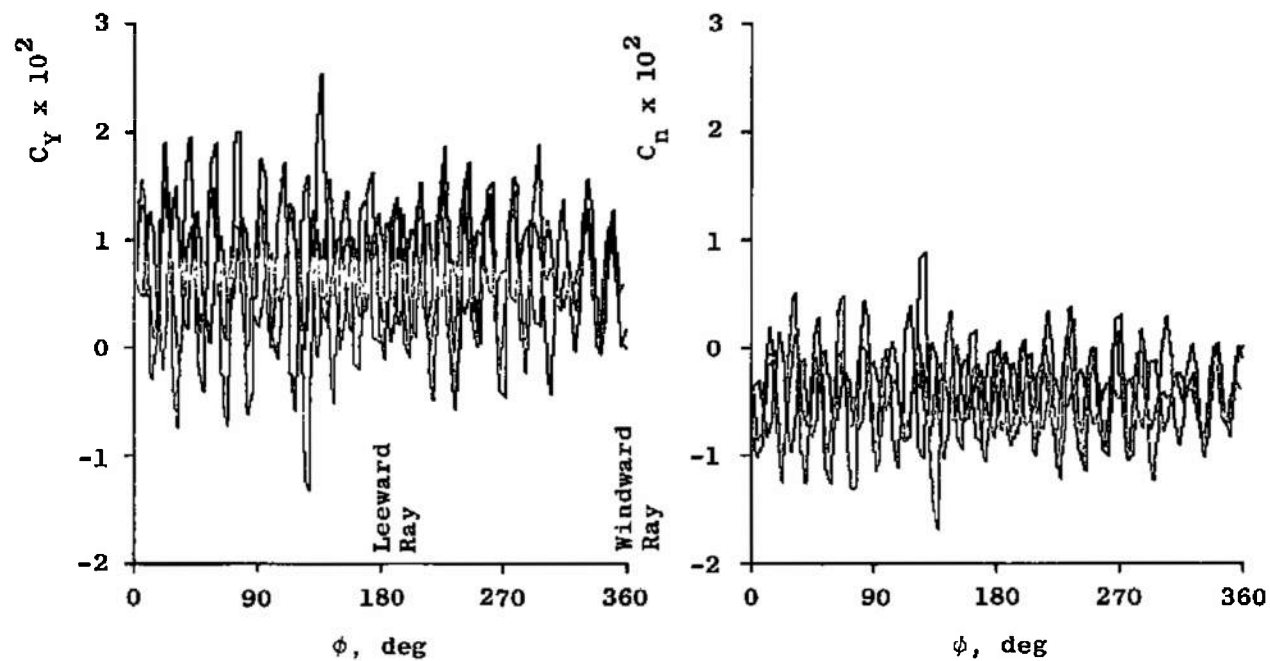
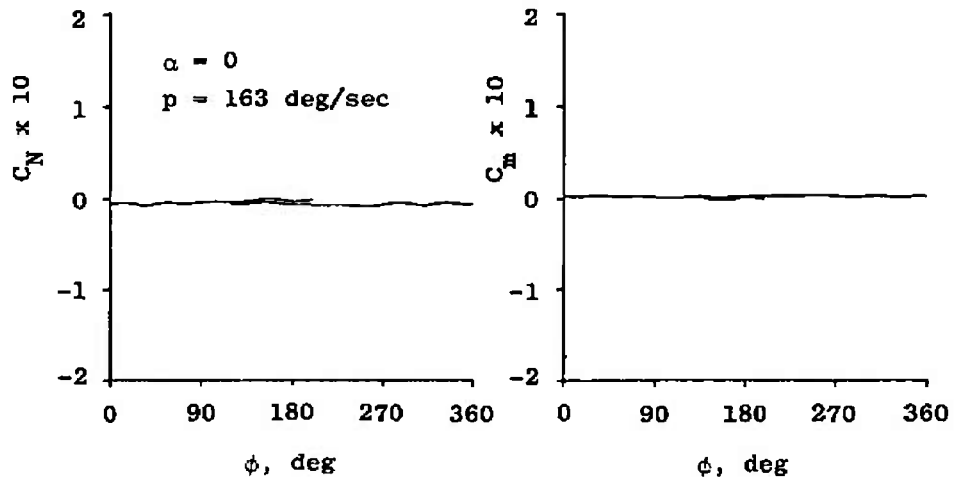


Figure 38. Unfiltered aerodynamic coefficients without tare correction.

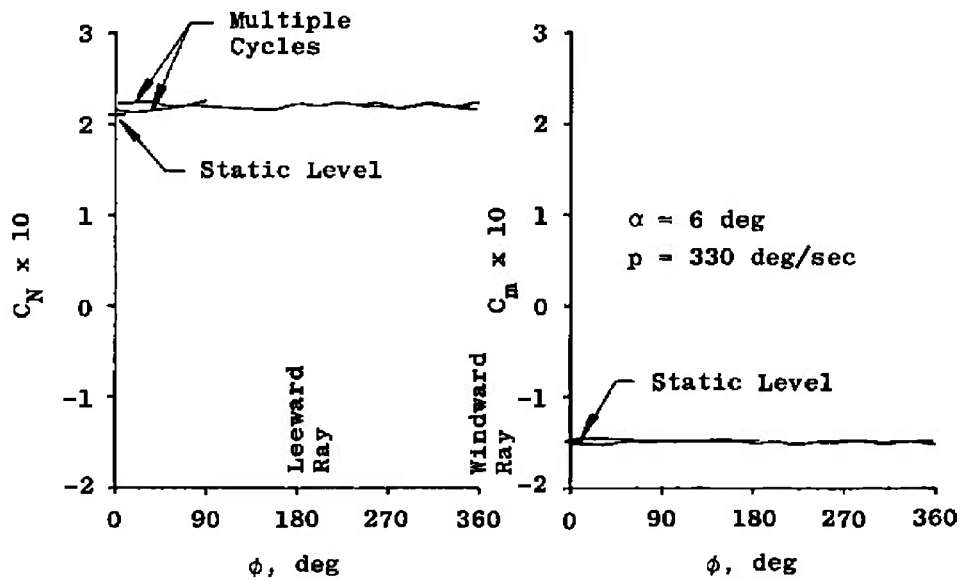
$$M_{\infty} = 7.95$$

$$Re_{\infty}/ft = 1.2 \times 10^6$$

$$r_n/r_b = 0.013$$



Tank Tare



Reduced Aerodynamic Data

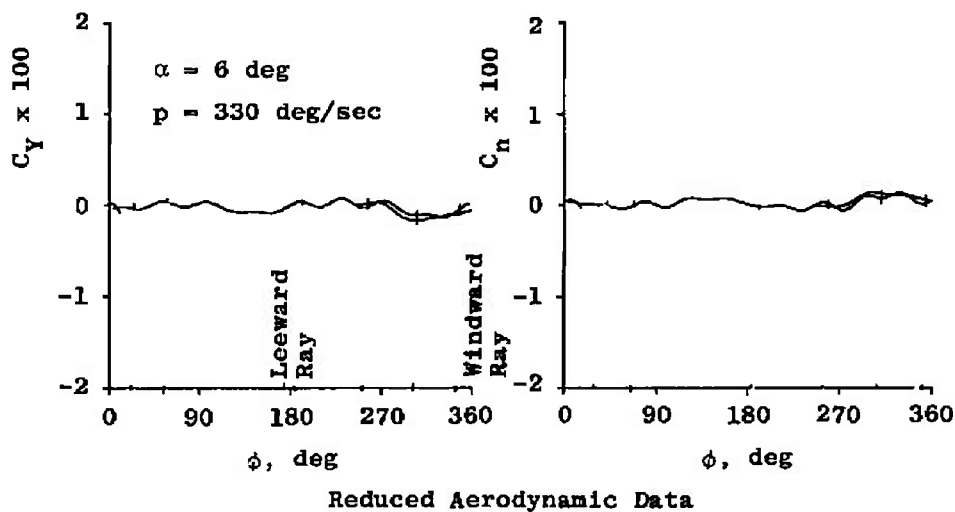
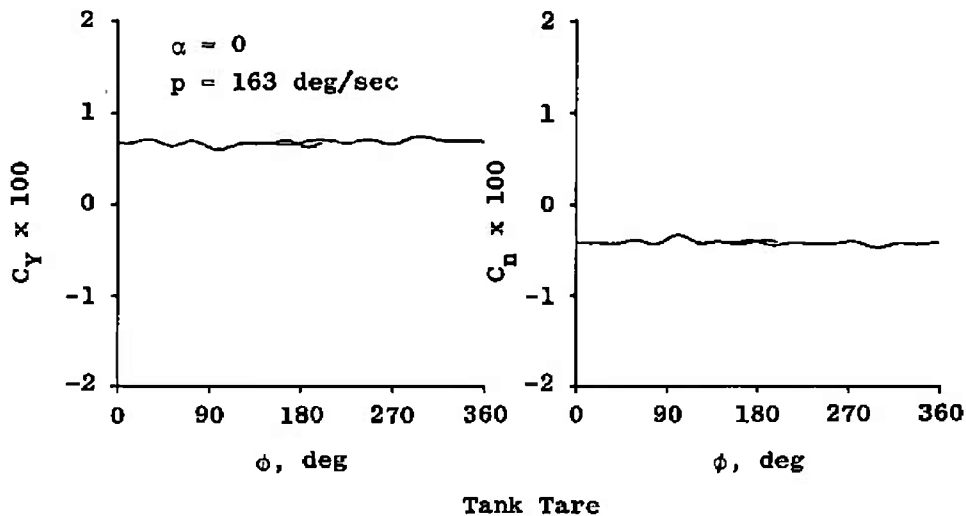
a. C_N and C_m

Figure 39. Representative dynamic aerodynamic coefficient data.

$$M_{\infty} = 7.95$$

$$Re_{\infty} = 1.2 \times 10^6$$

$$r_n/r_b = 0.013$$



b. C_Y and C_N
Figure 39. Concluded.

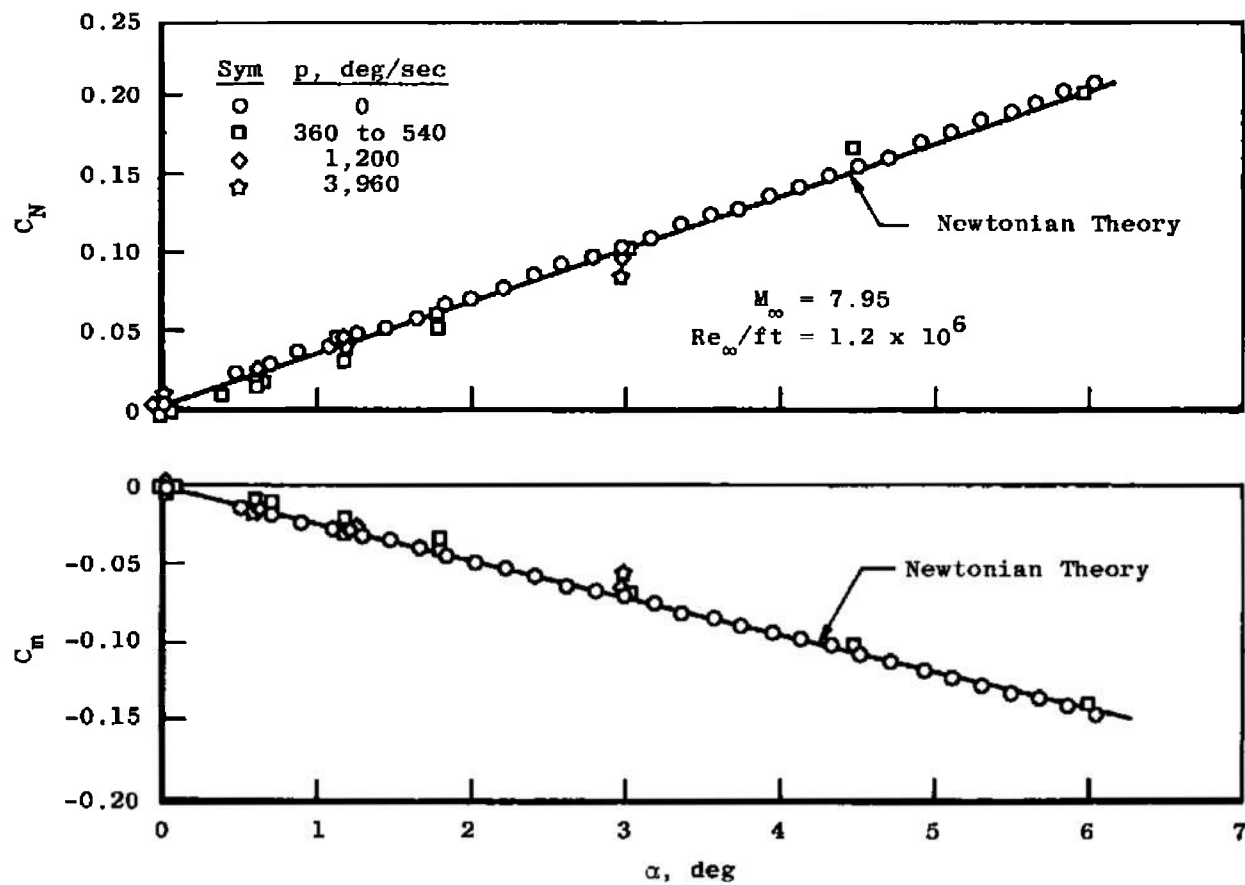


Figure 40. Aerodynamic coefficients for sharp cone at angle of attack.

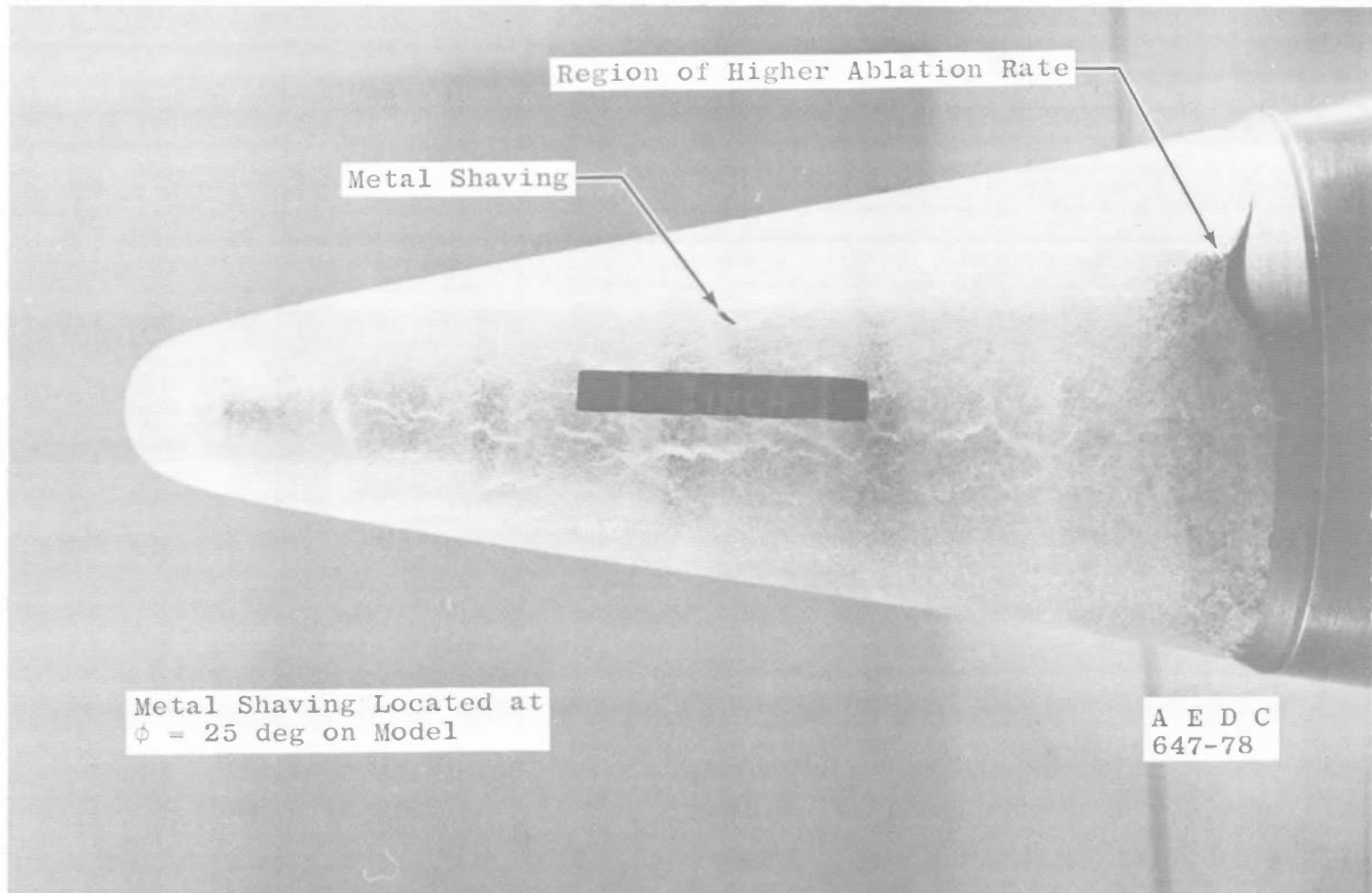


Figure 41. Posttest photograph of ablated camphor nose tip, $r_n/r_b = 0.042$.

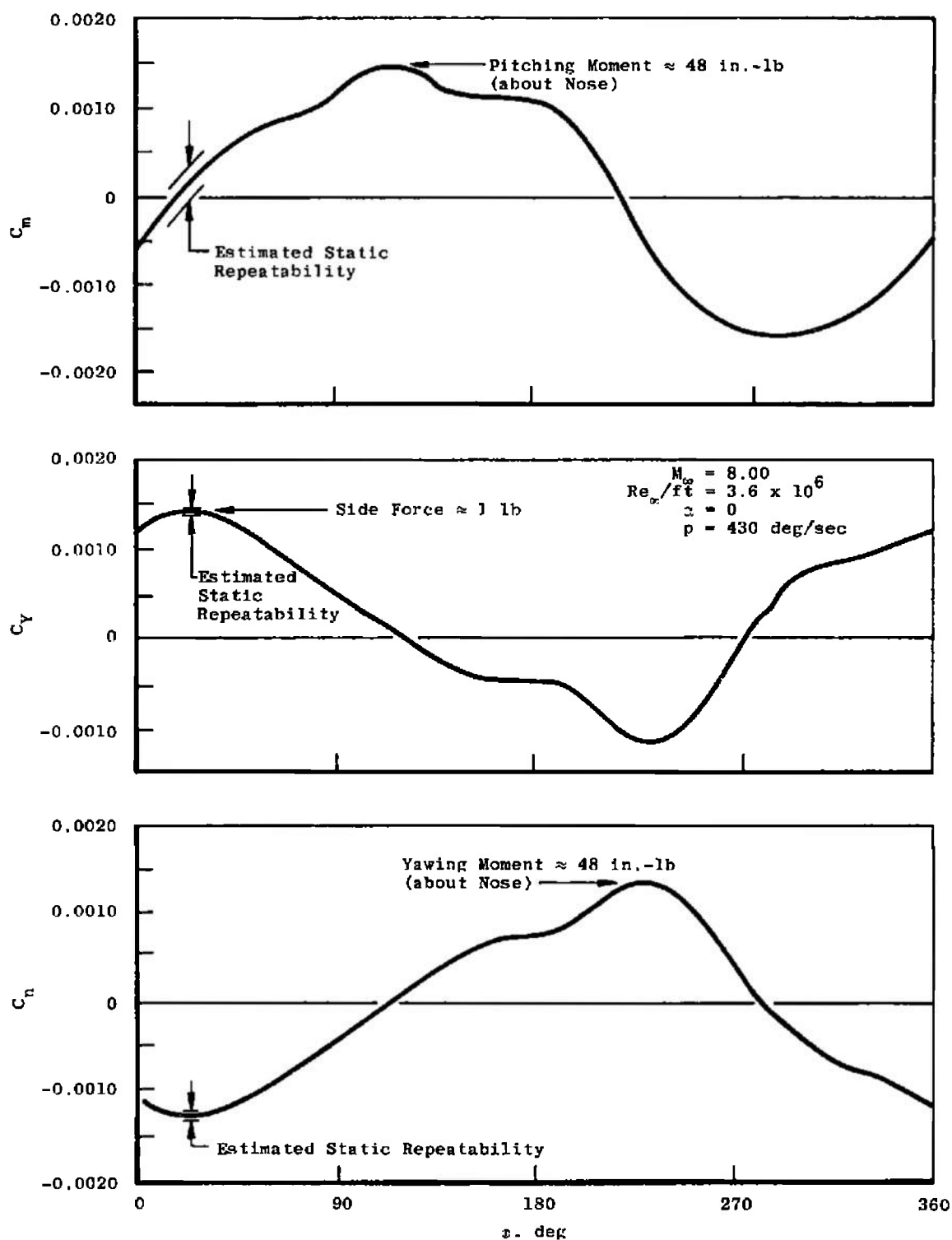
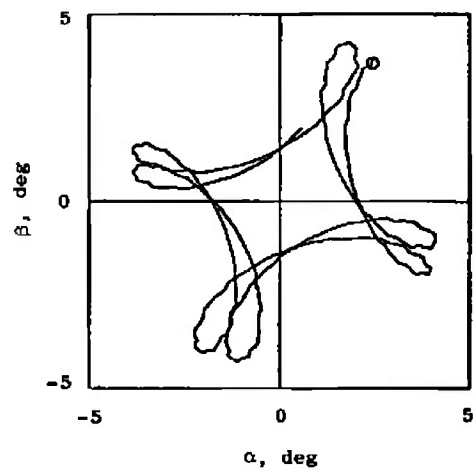
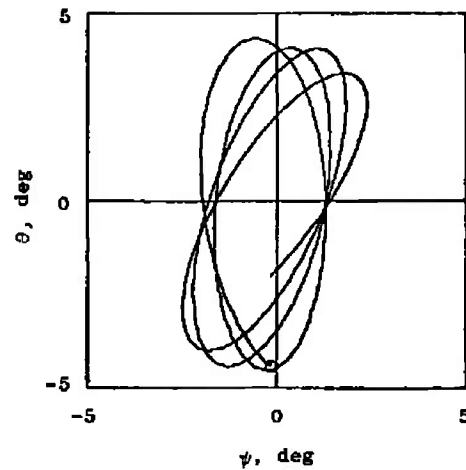


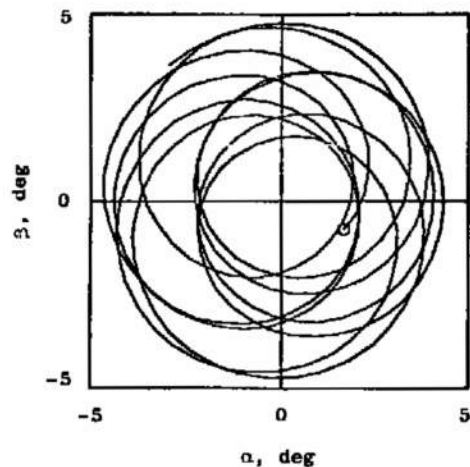
Figure 42. Aerodynamic coefficients on spinning model with camphor nose tip with imbedded metal shaving.



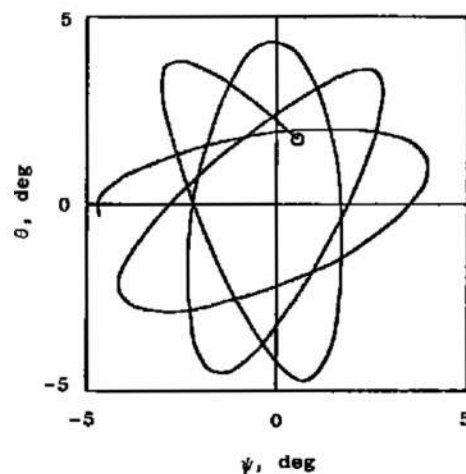
$M_\infty = 7.91$
 $Re_\infty/ft = 0.6 \times 10^6$
 Sharp Cone
 No Trips



a. $p = 103 \text{ deg/sec}$

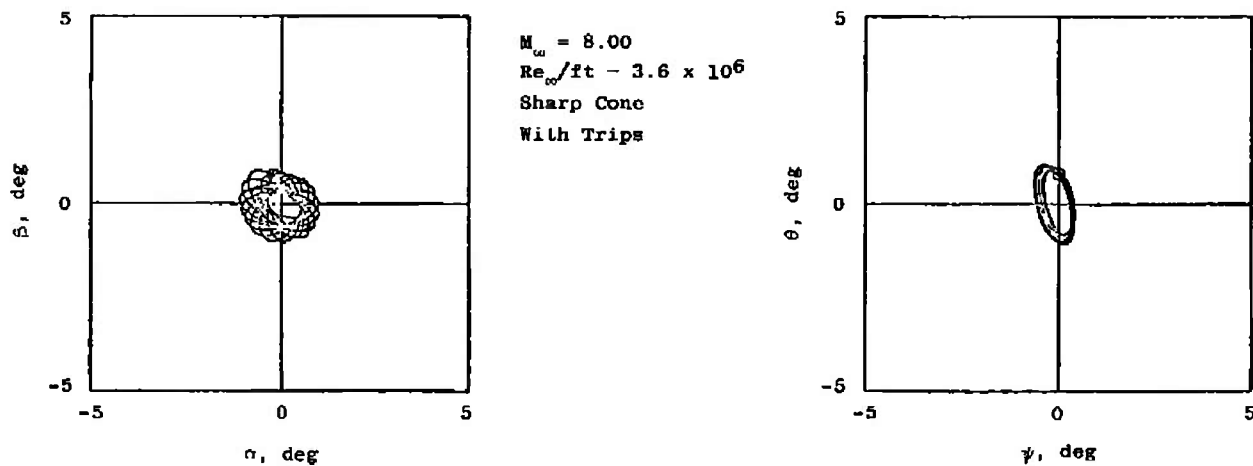


$M_\infty = 7.91$
 $Re_\infty/ft = 0.6 \times 10^6$
 Sharp Cone
 No Trips

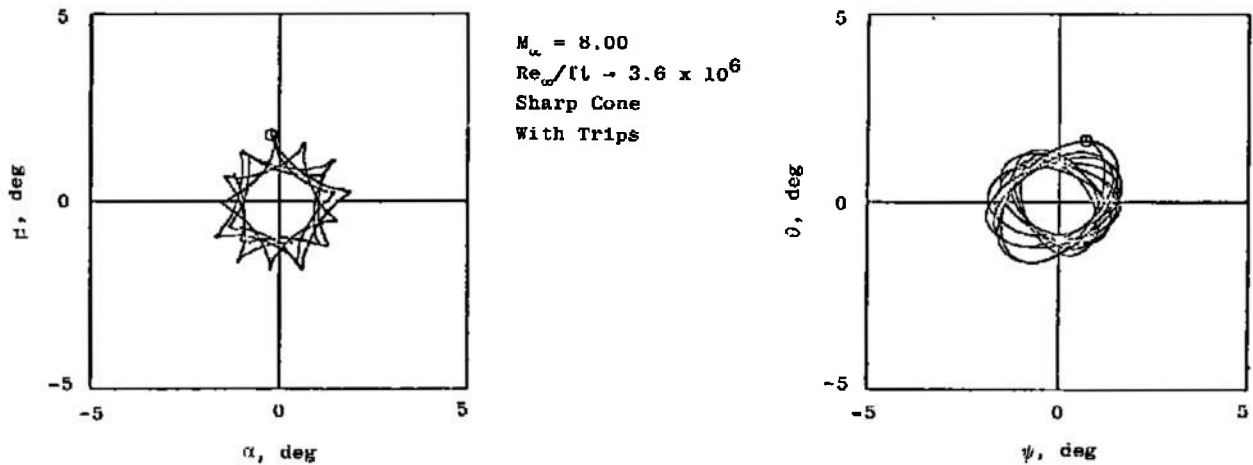


b. $p = -355 \text{ deg/sec}$

Figure 43. 3-DOF model motion - laminar boundary layer.



a. $p = 33$ deg/sec



b. $p = 351$ deg/sec

Figure 44. 3-DOF model motion - turbulent boundary layer.

Table 1. Test Summary

[illegible]

* Grit Description:

Type Trips

- A No. 30 grit on a 20-deg segment.
B No. 30 grit on two, 20-deg segments.
C No. 20 grit on a 20-deg segment.
3-Ball Three spherical balls of 0.078-in.
Diameter on 20-deg segment.

Table 1. Continued

Nose Configuration	Frustum Configuration	M_∞	$Re_\infty/ft \times 10^{-6}$	Type Trips	Data Type		
					Static	Spin	3-DOF
0.315-in. R. Nose, B ↓	Aluminum ↓	5	1.8	None ↓	—	X	—
		5	3.6		X	X	—
		5	6.0		X	X	—
		8	0.6		—	—	X
		↓	1.2	T/S Grooves ↓	X	X	X
		↓	2.4		—	—	X
		↓	3.6		X	X	—
		5	1.8		X	—	—
		5	3.6	Rect. Grooves 3-Ball ↓	—	X	—
		8	1.2		—	X	—
		8	3.6		—	X	—
		5	3.6		—	X	—
		8	3.6	Grit A Grit A Grit C Grit C ↓	—	—	X
		↓	0.6		—	—	X
		↓	1.2		—	—	X
		↓	2.4		—	—	X
		↓	3.6		—	—	X
		↓	2.4	None ↓	—	—	X
		↓	3.6		—	—	X
		↓	2.4		—	—	X
		↓	3.6		—	—	X
	Huskey Pup	↓	0.6	None ↓	—	—	X
	Huskey Pup	↓	2.4		—	—	X
	Huskey Pup	↓	3.6		—	—	X
	Antenna Window No. 1 (Note 1)	↓	1.2		—	X	X
		↓	3.6		—	X	X
	Antenna Window No. 2	↓	1.2	↓	—	—	X
		↓	1.2		—	—	X
	Ablated C. P.	↓	1.2		—	—	X
	Camphor	↓	3.6		—	X	—
	ASYM Aluminum No. 2	↓	0.6	↓	—	X	—
		↓	0.6		—	X	—
	Flat Smooth, E ↓	5	3.6		—	X	—
		5	6.0		—	X	—
		8	1.2		—	X	—
		8	3.6		—	X	—

Table 1. Continued

Nose Configuration	Frustum Configuration	M_∞	$Re_\infty ft \times 10^{-6}$	Type Trips	Data Type		
					Static	Spin	3-DOF
Flat Smooth, F ↓	Aluminum	5	1.8	None ↓	—	X	—
		5	3.6		X	X	—
		5	6.0		X	X	—
		8	1.2		—	X	—
		8	3.6		X	X	—
Flat Rough, F ↓	Aluminum	5	6.0	{ T/S } Grooves ↓ Rect. Grooves	—	X	—
		8	1.2		—	X	—
		8	3.6		—	X	—
		5	3.6		—	X	—
		5	3.6		—	X	—
Flat Notch, G ↓	Aluminum	8	0.6	None ↓	—	—	X
		↓	1.2		—	—	X
		↓	2.4		—	—	X
		↓	3.6		—	—	X
Flat Notch, H ↓	Aluminum	5	6.0	{ T/S } Grooves ↓ Rect. Grooves	—	X	—
		8	0.6		—	—	X
		↓	1.2		—	X	X
		↓	2.4		—	X	X
		↓	3.6		—	X	X
Biconic, I ↓	Aluminum	↓	↓		—	X	—
		5	6.0		—	X	—
		8	1.2		—	X	X
		8	2.4		—	X	X
		8	3.6		—	X	X
0.875-in. R., C ↓	Aluminum	5	↓	{ T/S } Grooves ↓ Rect. Grooves	—	X	—
		↓	↓		—	X	—
		↓	↓		—	X	—
		↓	↓		—	X	—
		↓	↓		—	X	—
Huskey Pup Huskey Pup Camphor	Huskey Pup Huskey Pup Camphor	↓	↓	None ↓	—	X	—
		↓	↓		X	X	—
		↓	↓		X	X	—
		↓	↓		X	X	—
		↓	↓		X	X	—

Table 1. Concluded

Nose Configuration	Frustum Configuration	M_∞	$Re_\infty/ft \times 10^{-6}$	Type Trips	Data Type		
					Static	Spin	3-DOF
1.500-in. R., D ↓	Aluminum ↓	5	1.8	None ↓	—	X	—
		5	3.6		X	X	—
		5	6.0		X	X	—
		8	0.6		—	X	—
		↓	1.2		X	X	—
0.315-in. R., Camphor	Camphor ↓	↓	3.6		X	—	—
		↓	↓		X	X	—
0.875-in. R., Camphor	Aluminum Camphor	↓	↓		—	X	—
		↓	↓		—	X	—
Active Trip (Fig. 17) (Note 2)	Aluminum ↓	↓	0.6		X	X	—
		↓	0.8		—	X	—
		↓	1.2		X	X	—
Gaseous Jet Nose Tip	↓	↓	0.6		X	X	—
		↓	0.8		X	X	—
		↓	1.2		X	X	—
		↓	3.6		X	X	—
Porous Tip (Note 3)	↓	↓	0.6		X	—	—
		↓	1.2		X	X	—

- Notes: 1. Various parts (fillers, etc.) were removed from antenna windows during these tests.
 2. All mass injection was run with various pressure regulators.
 3. Porosity of nose tips was varied.

NOMENCLATURE

a, b	Complex number constants, $a + jb$
C_m	Pitching-moment coefficient, pitching moment/ $q_\infty S \ell$
C_N	Normal-force coefficient, normal force/ $q_\infty S$
C_n	Yawing-moment coefficient, yawing moment/ $q_\infty S \ell$
C_Y	Side-force coefficient, side force/ $q_\infty S$
DLP	Data loop period, i.e., time required to read 1 loop of data (all multiverter channels), sec
F	General function
f	Frequency, Hz
$H(f)$	Transfer function, $H(f) = T[I(t)]/T[O(t)]$
h_o	Tunnel stilling chamber enthalpy, Btu/lbm
h_w	Specific enthalpy of gas at wall temperature, 540°F
$I(f)$	Input signal to gage in frequency domain, $I(f) = T[I(t)]$
$I(t)$	Input signal to gage in time domain
I_x, I_y, I_z	Moments of inertia for 3-DOF model
K_N	Adjustment constants for heat-transfer gages
ℓ	Model length, 47.353 in. for spin model and 31.423 in. for 3-DOF model
M	Magnitude of signal, $\sqrt{a^2 + b^2}$
M_f	Magnitude of transfer function
$M_{f=0}$	Magnitude of transfer function at $f = 0$
M_{INPUT}	Magnitude of transform of input signal
M_{OUTPUT}	Magnitude of transform of output signal

M_∞	Free-stream Mach number
$O(f)$	Output signal of gage in frequency domain, $O(f) = T[O(t)]$
$O(t)$	Output signal of gage in time domain
p	Spin of model, deg/sec
p_∞	Free-stream static pressure, psia
p_0	Tunnel stilling chamber pressure, psia
\dot{q}	Heat-transfer rate, Btu/ft ² -sec
q_∞	Free-stream dynamic pressure, psia
Re_∞/ft	Free-stream Reynolds number per ft
r_b	Base radius of model, in.
r_n	Nose radius, in.
S	Reference (base) area of model. 176.175 in. ² for spin model. 78.540 in. ² for 3-DOF model
ST_∞	Stanton number, $\dot{q}/\rho_\infty V_\infty (h_0 - h_w)$
T_∞	Free-stream static temperature, °R
T_0	Tunnel stilling chamber temperature, °R
$T[\]$	Fast Fourier Transform (FFT) of function in brackets
T_w	Wall temperature, °R
t	Time, sec
V_∞	Free-stream velocity, ft/sec
X_1-X_3, X_n	Function variable
X_{cpN}/ℓ	Center of pressure in pitch plane, $X_{cpN}/\ell = C_m/C_N$
X_{cpY}/ℓ	Center of pressure in yaw plane, $X_{cpY}/\ell = C_n/C_Y$

X_{mrp}	Moment reference center, about nose
x	Distance along model axis measured from virtual apex of nose, in.
x_{te}	End of boundary layer transition measured from virtual apex of sharp cone, in.
α	Model angle of attack (body fixed axes), deg
β	Angle of sideslip (body fixed axes), deg
ΔF	Error in function F
Δp_o	Error in p_o , psia
ΔX_1	Error in variable X_1
θ	Angle of pitch, (tunnel fixed axes), deg
ρ_∞	Free-stream density, lbm/ft ³
ϕ	Angle of roll, deg
ψ	Angle of yaw (tunnel fixed axes), deg
ω	Frequency of spin - p/360, Hz

SUBSCRIPTS

adjusted	Data adjusted for heat gage installation
unadjusted	Data as reduced from FFT or static program without any installation adjustments